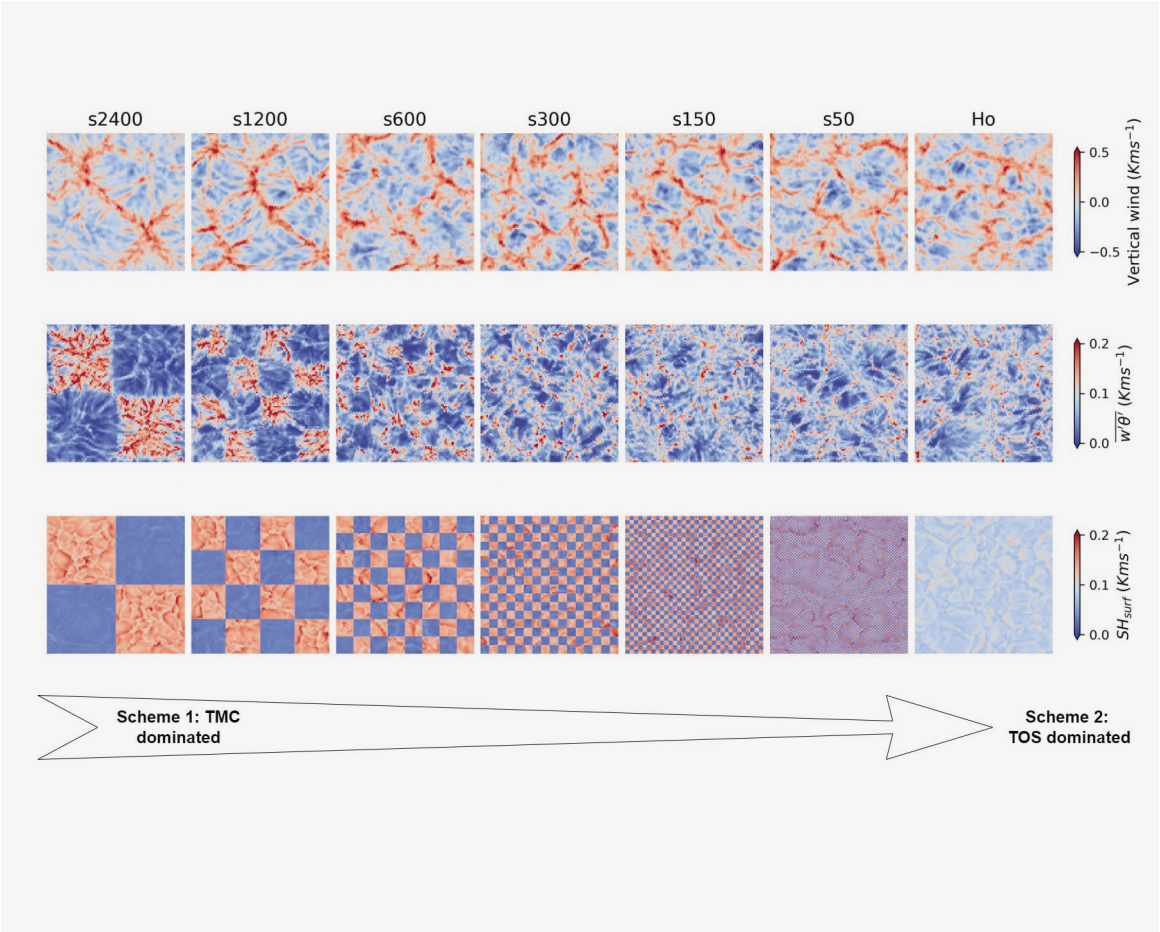

Modelling Secondary Circulation in Convective Boundary Layer Using Large Eddy Simulatione

Lijie Zhang

Energie & Umwelt / Energy & Environment
Band / Volume 652
ISBN 978-3-95806-799-8

Mitglied der Helmholtz-Gemeinschaft

JÜLICH
Forschungszentrum

Schriften des Forschungszentrums Jülich
Reihe Energie & Umwelt / Energy & Environment Band / Volume 652

Forschungszentrum Jülich GmbH
Institut für Bio- und Geowissenschaften (IBG)
Agrosphäre (IBG-3)

Modelling Secondary Circulation in Convective Boundary Layer Using Large Eddy Simulation

Lijie Zhang

Schriften des Forschungszentrums Jülich
Reihe Energie & Umwelt / Energy & Environment Band / Volume 652

ISSN 1866-1793 ISBN 978-3-95806-799-8

Bibliografische Information der Deutschen Nationalbibliothek.
Die Deutsche Nationalbibliothek verzeichnet diese Publikation in der
Deutschen Nationalbibliografie; detaillierte Bibliografische Daten
sind im Internet über http://dnb.d-nb.de abrufbar.

Herausgeber und Vertrieb:	Forschungszentrum Jülich GmbH Zentralbibliothek, Verlag 52425 Jülich Tel.: +49 2461 61-5368 Fax: +49 2461 61-6103 zb-publikation@fz-juelich.de www.fz-juelich.de/zb
Umschlaggestaltung:	Grafische Medien, Forschungszentrum Jülich GmbH
Druck:	Grafische Medien, Forschungszentrum Jülich GmbH
Copyright:	Forschungszentrum Jülich 2024

Schriften des Forschungszentrums Jülich
Reihe Energie & Umwelt / Energy & Environment, Band / Volume 652

D 5 (Diss. Bonn, Univ., 2024)

ISSN 1866-1793
ISBN 978-3-95806-799-8

Vollständig frei verfügbar über das Publikationsportal des Forschungszentrums Jülich (JuSER)
unter www.fz-juelich.de/zb/openaccess.

List of Symbols and Abbreviations

r_{ah}	Aerodynamic resistance of heat
r_{am}	Aerodynamic resistance of momentum
ρ	Air density
p	Air pressure
ABL	Atmospheric boundary layer
zi	Boundary layer height/boundary layer depth
CBL	Convective boundary layer
w_*	Convective velocity scale
γ_θ	Counter-gradient term
ESMs	Earth System Models
EC	Eddy covariance
K_h	Eddy diffusivity
K_m	Eddy viscosity
FI	Flux Imbalance
$\langle I \rangle$	Flux Imbalance in the calculation
FLIMK	Flux Imbalance and K-theory scheme
De18	Flux imbalance prediction model proposed by De Roo *et al.,* (2018)
H08	Flux imbalance prediction model proposed by Huang *et al.,* (2008)
W22	Flux imbalance prediction model proposed by Winner *et al.,* (2022)
Z19	Flux imbalance prediction model proposed by Zhou *et al.,* (2019)
u_*	Friction velocity
U	Horizontal wind speed
ICON	Icosahedral Nonhydrostatic
ψ_h	Integral format of the universal function Φ_h
ψ_m	Integral format of the universal function Φ_m
lw	Integral length scale of vertical velocity
L-A	Land-Atmosphere
LES	Large Eddy Simulation
MOST	Monin-Obukhov Similarity Theory
N-S equation	Naiver-Stokes equation
NWP	Numerical Weather Prediction

L	Obukhov length
PBL	Planetary boundary layer
θ	Potential temperature
d	Replacement height
z_{0h}	Roughness length for heat
z_{0m}	Roughness length for momentum
SCM	Single column mode
C_p	Specific heat capacity of air
θ_*	Temperature scale
TMC	Thermally-induced secondary circulations
T	Time average interval
$\overline{w'\theta'}$	Turbulent heat flux
TOS	Turbulent organized structures
Pr_t	Turbulent Prandtl number
Φ_h	Universal function of heat
Φ_m	Universal function of momentum
κ	von Kármán constant
τ	Wind shear
V_a	Wind speed in the atmosphere
u,v,w	Wind speed in the x, y and z directions is expressed in Cartesian coordinates.

Contents

List of Figures

List of Tables

Abstract

Mesoscale secondary circulations, which frequently arise over heterogeneous land surfaces, profoundly influence atmospheric structure and characteristics. Its structure is primarily shaped by the combined effects of wind shear and buoyancy. The turbulence generated by the secondary circulation can considerably influence the fluxes, including estimations employed in the Monin–Obukhov similarity theory and measurements in eddy covariance systems. An ever-increasing body of evidence points to secondary circulations as the primary source of the reported underestimation of heat flux (i.e., flux imbalance, *FI*) by 10% to 30% across various sites.

A series of large eddy simulations (LES) were conducted in this PhD work to investigate the formation of secondary circulations under different conditions and to quantify its impact on flux estimations. These included one-dimensional strip-like soil moisture distribution with ambient wind speeds ranging from 0.5 ms^{-1} to 16 ms^{-1} in various wind directions (Chapter 3), two-dimensional checkerboard soil moisture distribution with heterogeneous scales varying from 50 m to 2,400 m (Chapter 4). A secondary circulation strength metric is proposed and found to have a positive correlation with the Bowen ratio and heterogeneity parameter, and a negative correlation with wind speeds when the wind direction is perpendicular to the direction of heterogeneity. It was observed that as the strength of the secondary circulation increased, the turbulent heat flux decreased, maintaining the same soil moisture conditions. Two distinct secondary circulation schemes are identified based on the heterogeneity scale: thermally-induced secondary circulations (TMCs) and turbulent organized structures (TOS).

The results of the LES were used to evaluate four selected *FI* prediction models. These models demonstrated an ability to capture the *FI* accurately. A novel first-order nonlocal turbulence closure scheme has been proposed (Chapter 5), namely the flux imbalance and K-theory (FLIMK), which employs the *FI* prediction model to account for the nonlocal processes and the conventional K-theory for the local processes. The FLIMK scheme has been demonstrated to reduce the flux imbalance from 15% to 6% in LES and from 16% to 6.7% in numerical weather prediction (NWP) models.

Chapter 1

1. Introduction

1.1. Background

Earth system models (ESMs) are becoming an indispensable source of information about the current state of our planet and replicating past conditions as well as predicting future changes (Pitman, 2003; Bauer, Thorpe and Brunet, 2015; Chow *et al.*, 2019; Blyth *et al.*, 2021). The atmospheric model component of ESMs simulates the transport of momentum, heat, moisture, and other scalar quantities by atmospheric turbulence of varying scales. The buoyancy and mechanical turbulence generate large eddies, which are subsequently broken down into smaller eddies through an energy cascade process (Wyngaard, 2010). These processes span a wide range of spatial and temporal scales (Katul *et al.*, 2007). Since resolving eddy motion at all scales is not feasible, the unresolvable parts must be parameterized in ESMs (Avissar *et al.*, 1989). In summary, the accuracy of ESMs is highly dependent on the parameterization of the physical process.

The atmospheric boundary layer (ABL), approximately the bottom 10% of the troposphere (Figure 1.1 a and b), is highly responsive to and influenced by surface conditions on a timescale of an hour or less (Stull, 1988). ABL displays daily variability (Collaud Coen *et al.*, 2014), with its depth (i.e. the boundary layer height, z_i) ranges from several kilometers in the afternoon to as low as a few tens of meters at night, as shown in Figure 1.1c. After sunrise, the land surface is continuously heated by incoming solar radiation, which in turn warms the air above it. This process creates thermals and enhances turbulent mixing (Pleim, 2007; Sun *et al.*, 2012). As a result, the boundary layer height increases after sunrise and reaches maximum in the afternoon. This phenomenon is known as the convective boundary layer (CBL) or unstable boundary layer (Cioni and Hohenegger, 2017). After sunset, the land surface cools more rapidly than the air above, forming a stable boundary layer (SBL) characterized by a downward heat flux that inhibits vertical mixing (Joffre *et al.*, 2001; Lothon *et al.*, 2014). This PhD work focuses on the CBL; hence, any reference to the boundary layer in the following content, unless explicitly stated otherwise, pertains to the CBL. To demonstrate the characteristics of CBL, the schematics of the mean vertical profile of potential temperature (θ) and turbulent heat flux ($\overline{w'\theta'}$) are presented in Figure 1.2. The CBL can be broadly divided into three layers, from the

bottom to the top: the surface layer, the mixed layer, and the entrainment zone. Above the CBL is the free troposphere.

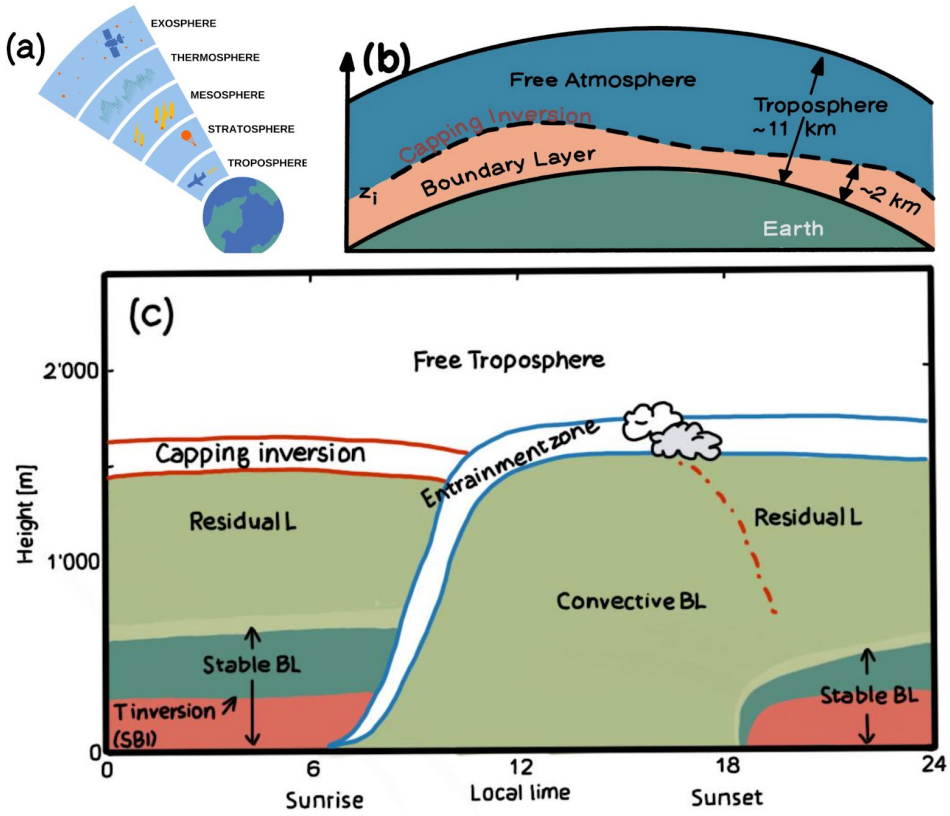

Figure 1.1: The Earth's atmosphere (a), the atmospheric boundary layer, ABL (b, modified from https://byjus.com/physics/atmosphere/) and daily dynamics of the ABL (c, adapted from Stull, 1988).

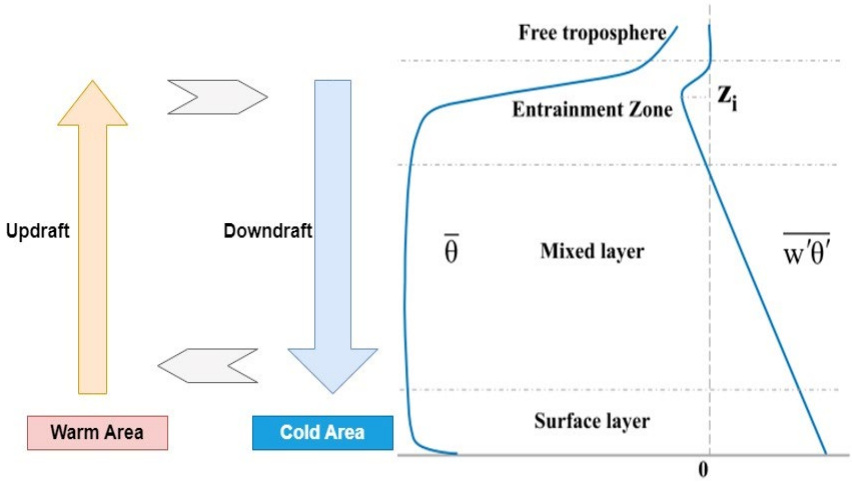

Figure 1.2: Sketch of the secondary circulation (left), and vertical profile of potential temperature and turbulent heat flux (right) within the convective boundary layer (adapted from Zhou et al (2018)).

The lowest portion of CBL is the surface layer, which is distinguished by nearly constant turbulent fluxes and referred to as the constant flux layer (Stull, 1988). Turbulent transport within the surface layer is generally considered more effective than molecular diffusion, except in a roughness sublayer near the surface, which is only a few centimeters thick (Boekee *et al.*, 2024). Most field measurements were collected within the surface layer, which is important for parameterizing the land-atmosphere (L-A) interactions. The surface layer process displays self-similarity and can be elucidated using the Monin-Obukhov similarity theory (MOST) that the turbulent fluxes and mean gradients can be related through similarity functions with only a few key parameters (Monin and Obukhov, 1954; Foken, 2006). Those parameters are the friction velocity ($u_* = [(\overline{u'w'})^2 + (\overline{v'w'})^2]^{1/4}$, u, v and w are the wind speed in x, y and z direction in the Cartesian coordinates, respectively), the buoyancy parameters ($\frac{g}{\theta}$, where g is the gravitational acceleration and θ is the potential temperature), the measurement height (z) and the turbulent heat flux at the land surface ($\overline{w'\theta'}$), more details about MOST are presented in chapter 2.

$$\frac{\partial \bar{u}}{\partial z} = \frac{u_*}{\kappa z}\phi_m\left(\frac{z}{L}\right); \frac{\partial \bar{\theta}}{\partial z} = \frac{\theta_*}{\kappa z}\phi_h\left(\frac{z}{L}\right). \quad (1.1)$$

$L = \frac{-{u_*}^3\theta_v}{\kappa g(\overline{w'\theta'})_s}$ is the Obukhov length, κ is the von Kármán constant with a typical value of 0.4. ϕ_m and ϕ_h are the universal functions for momentum and heat, respectively, which is

determined empirically from the experimental data (Stull, 1988). To illustrate, the 1968 Kansas Atmospheric Surface-Layer Experiment, one of the pioneering works in micrometeorology (Kaimal and Wyngaard 1990), furnished invaluable data for determining the universal functions in the current forms of the MOST. The hypothesis of MOST posits that in a stationary, horizontally homogeneous surface layer, turbulence is driven by shear and buoyancy forces with negligible Coriolis effects. This hypothesis has been validated over horizontal homogeneous surfaces (Högström, 1988; Foken, 2006).

However, in real-world scenarios, the Earth's surface is rarely homogeneous. In contrast, the landscape is generally heterogeneous, encompassing urban areas, water bodies, forests, agricultural fields, complex terrains, and diverse soil moisture conditions. Each landscape exhibits distinct physical characteristics (Su, 2002; Gerken *et al.*, 2019). The validity of the MOST is called into question by surface heterogeneity, which results from violating its fundamental assumptions regarding steady conditions over a homogeneous surface. For example, significant mesoscale fluxes were observed to be tied to terrain heterogeneity (Avissar and Chen, 1993). A series of experiments were conducted to investigate the impact of heterogeneous land surfaces on atmospheric structure and statistics and to continuously develop MOST under various conditions (Businger *et al*., 1971; Högström, 1988; Mahrt, 2000). These include CASES-99 (Sun *et al*., 2012), FESSTVal (Hohenegger *et al*., 2023), and LITFASS-2003 (Mauder *et al*., 2006), among others.

Above the surface layer, the potential temperature is nearly constant with height until reaching the entrainment zone. With regard to turbulent fluxes, a linear decrease is observed with height, reaching a minimum of approximately -0.2 times the surface heat flux at the top of the CBL. This characteristic is also frequently employed to determine the CBL height, which is defined as the height where the sensible heat flux profile has its minimum. In general, the heterogeneity of the surface (e.g., variations in topography, vegetation, soil moisture, among others) gives rise to the heterogeneous temperature of the land surface, leading to an updraft in warm areas, which results in a lower (higher) density at the bottom (top) of the boundary layer. Conversely, the area with lower temperature exhibits downdrafts, which exert an opposing effect. These differences in air density give rise to pressure gradients, which in turn give rise to compensatory air movements, thus forming secondary circulations, as shown in Figure 1.2. The secondary circulation is analogous to the sea-land breeze and is also referred to as the '*inland breeze*' (Raasch and Harbusch, 2001; Eder, Serafimovich and Foken, 2013; Kenny *et al.*, 2017). Large-scale eddies generated by secondary circulation can penetrate more deeply into the entrainment

zone than smaller eddies (Avissar and Schmidt, 1998). This process draws warmer air from the upper free troposphere into the boundary layer by entrainment process, resulting in a relatively larger entrainment flux when secondary circulation is present. As a result, the height of the boundary layer increases. Additionally, the vertical profile of boundary layer characteristics is influenced by secondary circulation; a larger liquid water content was observed over a more heterogeneous land surface than a homogeneous surface in a large eddy simulation (LES) study (Han *et al.,* 2019), further affecting the development of the shallow cumulus cloud.

The formation of the secondary circulation depends on the combined effect of buoyancy and shear. Under conditions of strong mean shear and low surface heat fluxes, convective updrafts are often arranged into horizontal rolls (Steinfeld *et al.*, 2007). These quasi-two-dimensional structures are usually aligned 10-20 degrees to the left of the geostrophic wind direction in the northern hemisphere (Salesky, Chamecki and Bou-Zeid, 2017). Conversely, weak mean shear and high surface heat fluxes lead to the formation of open convective cells (Poll, Shrestha and Simmer, 2017). Secondary circulation affects the structure of the atmosphere and contributes to nonlocal processes (Mahrt, 2000; Raasch and Harbusch, 2001), which leads to the underestimation of heat flux measurements by 10 to 30% across various sites and land cover types globally (Stoy *et al*., 2023; Franssen *et al*., 2010; Wilson *et al*., 2002). In this work, this underestimation is termed consistently Flux Imbalance, *FI*. For instance, Eder *et al*., (2014) provided experimental evidence over cropland in Germany, showing that secondary circulations are inherently not captured by single-tower eddy covariance (EC) measurement systems. Margairaz *et al*., (2020) employed spatial EC measurements to directly determine the dispersive fluxes, finding that the contribution of the dispersive fluxes to the total heat flux ranges from 5-10% near the surface and could reach up to 40% at a height of 100 meters in a desert in Utah, USA. Additionally, the accuracy of flux measurements largely depends on the relative location of the measurement site to the structure of the secondary circulation. In other words, overestimations may also occur if the site is consistently located in an updraft area, as has been reported in Prabha *et al*., (2007).

Meanwhile, the technique of Large Eddy Simulation (LES) has gained increasing popularity for studying large Reynolds number turbulent flows, such as those observed in the atmosphere (Moeng, 1984). LES is employed to resolve large-scale, energy-containing eddies while parameterizing small-scale processes with a typical grid size of 10-100 m (Sullivan and Patton, 2011). LES is frequently used to construct and evaluate parameterizations in coarse resolution models, such as the numerical weather prediction models (NWP). LES-generated high spatial-

temporal data have been used to study the formation of secondary circulations and their impact on atmospheric structures and properties (Zhou, Zhu and Xue, 2017; Gustafson *et al.*, 2020; Waterman *et al.*, 2024). For example, Patton et al. (2005) examined the impact of heterogeneity scales on atmospheric structure. Their findings indicated that the strength and extent of the organized motion depend on the heterogeneity scale relative to the boundary layer height (z_i), with the optimal value being between 4 to 9 times. Avissar and Schmidt (1998) demonstrated that an ambient wind of 2.5 ms^{-1} is sufficient to reduce the impact of land surface heterogeneity on the atmospheric structure, and an ambient wind of 5 ms^{-1} eliminates all impacts from the surface heterogeniety. Nevertheless, in a separate study, Raasch and Harbusch (2001) demonstrated that the circulation structure persists even at ambient winds of 7.5 ms^{-1}. The discrepancy suggests the necessity for further inquiry into the significance of ambient wind directions relative to the heterogeneity pattern (Huang and Margulis, 2013).

In addition, several attempts have been made to quantify the impact of secondary circulation on flux estimation and associated errors with both measurements (Eder, De Roo, *et al.*, 2015) and LES (Huang, Lee and Patton, 2008; De Roo and Mauder, 2018a; De Roo *et al.*, 2018; Zhou, Li and Li, 2019; Wanner, Calaf and Mauder, 2022), leading to the proposal of several semi-empirical models for predicting flux imbalance (*FI*). Huang *et al.*, (2008) employed both top-down and bottom-up tracers in LES to quantify the influence of entrainment and bottom-up diffusion processes on *FI*. They proposed that *FI* can be described as a function of atmospheric stability ($-\frac{z_i}{L} = \frac{\frac{g}{\theta_v}\overline{(w'\theta')}_s}{u_*^3/(\kappa\, z_i)}$) and a ratio of measurement height to boundary layer height (z/z_i). Formulas of a similar nature were proposed and evaluated in De Roo *et al.*, (2018), Mauder *et al.*, (2021) and Wanner *et al.*, (2022). The findings of Panin and Bernhofer (2008), based on data from a tall flux tower in Cabauw, the Netherlands, indicate that *FI* increases with the increase of landscape heterogeneity. They propose that incorporating the effective roughness length in the calculation of the heat flux could enhance the closure of the energy balance. Zhou *et al.*, (2019) demonstrated that the *FI* is influenced by a number of factors, including the mean horizontal wind (U), the averaging time period (T), atmospheric stability, and the integral length of vertical velocity (l_w, an indicator of the autocorrelation of the vertical wind). The concept of cospectral between the vertical wind and potential temperature was employed to support this conclusion.

1.2. Flux Imbalance

In the discussion of the *FI* near the land surface, we commence with basic energy conservation considerations,

$$R_{net} = H + LE + G + \varepsilon, \tag{1.2}$$

where $R_{net} = S\downarrow + S\uparrow + L\downarrow + L\uparrow$ is the total amount of radiation energy available at the surface, $S\downarrow$ and $S\uparrow$ are the incoming and outgoing shortwave radiation, respectively. $L\downarrow$ is the incoming longwave radiation from the thermal radiation emitted by the atmosphere, and $L\uparrow$ is the outgoing longwave radiation from the land surface emission. On the right-hand side of equation 1.2 are the sensible heat flux (*H)*, the latent heat flux (*LE)*, the ground heat flux (G), and the residual (ε).

In the field, the sensible and latent heat fluxes are typically measured using Eddy Covariance (EC) measurement systems, which operate at a point scale with a footprint extending up to hundreds of meters (Kljun, Rotach and Schmid, 2002). In models, the turbulent transport is generally parameterized through the MOST, e.g. in ESMs (Lawrence *et al.*, 2019). However, both EC and the MOST rely on the same fundamental assumptions of steady-state conditions over flat homogeneous surfaces, negligible horizontal advection, and no additional source or sink (Foken, 2006). The measured sensible and latent heat flux is often reported to be underestimated by 10% to 30 % (Wilson *et al.*, 2002; Barr *et al.*, 2006; Franssen *et al.*, 2010; Stoy *et al.*, 2013). In a recent review, Mauder *et al*., (2020) summarized four main hypotheses for the underlying causes of the *FI*: instrument error, data processing error, additional energy source, and sub-mesoscale transport. Nevertheless, even after a meticulous quality control process of the measurement data over relatively flat and homogeneous land surfaces, the *FI* persists, indicating that sub-mesoscale transport (i.e. secondary circulations) is the primary cause of the *FI* (Mauder *et al*., 2007; Eder *et al*., 2014).

Efforts have been made to identify the factors related to the *FI*. For example, the *FI* decreased as the time average period (T) increased and the measurement height (z) decreased. According to Schalkwijk's investigation, which utilized a long-term LES over a homogenous land surface in Cabauw, the Netherlands, the *FI* is only a few percent for a 3600-s average period at 16 m, but increases to over 20% for a 900-s average period at 100 m. Franssen *et al*., (2010) investigated 26 EC stations from the European FLUXNET sites and found that the *FI* decreased with an increase in horizontal wind speed (U) and friction velocity (u_*). Similar outcomes were observed by Stoy *et al.*, (2013), who examined 173 EC sites from the FLUXNET database

(Baldocchi *et al.*, 2001). More details of those factors that influence the flux imbalance are listed in Table 1.1.

Table 1.1: Factors that influence the flux imbalance. The larger the factor, the larger the flux imbalance. Any exception is marked ⋆, including the time average period, the horizontal mean wind velocity, and the friction velocity.

Factors	Reference	
	Measurement-based	Simulation-based
Average period (T) ⋆	(Mauder et al. 2007)	(Kanda *et al.*, 2004; Steinfeld *et al.*, 2007; Schalkwijk, Jonker and Siebesma, 2016)
Height (z)	(Lu.Zhang et al. 2024)	(Huang, Lee and Patton, 2008; De Roo and Mauder, 2018a; De Roo *et al.*, 2018; Zhou, Li and Li, 2019; Liu *et al.*, 2024)
Horizontal mean wind velocity (U) ⋆	(Franssen *et al.*, 2010)	(Zhou, Li and Li, 2019)
Friction Velocity ⋆	(Wilson *et al.*, 2002; Franssen *et al.*, 2010; Stoy *et al.*, 2013; Eder, Schmidt, *et al.*, 2015)	(Huang, Lee and Patton, 2008; Zhou, Li and Li, 2019)
Atmospheric stability	(Franssen *et al.*, 2010; Stoy *et al.*, 2013)	(Huang, Lee and Patton, 2008; De Roo and Mauder, 2018a; De Roo *et al.*, 2018; Zhou, Li and Li, 2019; Liu *et al.*, 2024)
Phase difference	(Gao, Liu, *et al.*, 2017)	-
Integral length scale of vertical velocity (lw)	-	(Zhou, Li and Li, 2019)
Asymmetric structure	(Lan *et al.*, 2023)	(Liu *et al.*, 2024)

1.3. Research Questions and Objectives

An increasing body of evidence indicates that secondary circulation is the primary cause of *FI* (Eder, De Roo, *et al.*, 2015; De Roo and Mauder, 2018a). Various factors related to *FI* have been investigated, and several *FI* prediction models have been proposed (Huang, Lee and Patton, 2008; De Roo *et al.*, 2018; Zhou, Li and Li, 2019; Wanner, Calaf and Mauder, 2022;

Zhou, Sühring and Li, 2023). However, the role of ambient winds in the formation of secondary circulation requires further investigation. Moreover, models for predicting *FI* were proposed to quantify the impact of the secondary circulation on flux estimation. Nevertheless, the assessment of these *FI* prediction models in the context of more intricate two-dimensional heterogeneous land surfaces remains uncertain. While the *FI* prediction model has been applied in EC measurements, its potential application in ESMs parameterization also needs further investigation. This dissertation seeks to address the following key research questions:

- How do ambient winds affect the formation of the secondary circulation? What strength indicators can describe secondary circulations? How does the strength of secondary circulations relate to the energy content in the surface layer?
- How does the heterogeneity scale affect the formation of secondary circulation? How does the *FI* prediction model work on a two-dimensional heterogeneous land surface? What role does the measurement height play in flux imbalance?
- How can the flux imbalance prediction model be utilized to enhance the representation of heat flux in the surface layer within ESMs?

Answering these questions defines the scope of this PhD dissertation. Chapter 2 provides an overview of the ABL dynamics, encompassing the fundamental governing equations, Reynolds decomposition and averaging, and the Monin-Obukhov similarity theory. Chapter 3 uses LES to investigate soil moisture heterogeneity-induced secondary circulations under different ambient wind conditions. A continuous soil moisture distribution in a one-dimensional stripe-like pattern is used to mimic a '*flat river corridor'*. Various ambient wind speeds, ranging from 0 to 16 ms^{-1}, are incorporated from different directions. A secondary circulation strength metric based on phase-wind decomposition following Patton *et al.,* (2005) is proposed, and the impact of secondary circulation on different energy content in the surface layer is analyzed. The second study (Chapter 4) extends the land surface heterogeneity into a two-dimensional checkerboard pattern of soil moisture distribution, with scales ranging from 50 m to 2,400 m. Different secondary circulation schemes are identified. The output of the LES is employed in the evaluation of four *FI* prediction models. Furthermore, the influence of the measurement height on the *FI* is examined through quadrant analysis. In light of the findings presented in Chapter 4, the third study (Chapter 5) proposes a novel approach, Flux Imbalance and K-theory (FLIMK), which integrates *FI* prediction models to account for the local process in conjunction with the conventional gradient diffusion method (also referred to as K-theory) to account for

the nonlocal process. The FLIMK scheme has been evaluated in both idealized LES with prescribed heat flux and real-case forced NWP scenarios, demonstrating a notable enhancement in the flux estimation. Chapter 6 presents a comprehensive summary and conclusions of the research conducted in this PhD work. It includes an evaluation of the contributions and limitations of the research, as well as insights into potential avenues for future research.

1.4. List of Publications

The chapters are derived from papers that have been published in peer-reviewed journals, are currently under review, or are ready for submission.

Chapter 3: Zhang, Lijie, Stefan Poll, and Stefan Kollet. 2023. “Large-eddy Simulation of Soil Moisture Heterogeneity-induced Secondary Circulation with Ambient Winds.” *Quarterly Journal of the Royal Meteorological Society* 149(751):404–20. doi: 10.1002/qj.4413.

Chapter 4: Zhang, Lijie, Stefan Poll, and Stefan Kollet. 2024. “Assessing the Performance of Flux Imbalance Prediction Models Using Large Eddy Simulations Over Heterogeneous Land Surfaces.” *Boundary-Layer Meteorology.* 190, 43 (2024). doi:10.1007/s10546-024-00880-y

Chapter 5: Zhang, Lijie, Stefan Poll, Jan Weinkaemmerer, Stefan Kollet. “An Alternative Way to Parameterizing the Nonlocal Scale Sensible Heat Flux Using the Flux Imbalance and K-theory Approach” (To be submitted)

Chapter 2

2. Atmospheric Boundary Layer Dynamics

The various scales of atmospheric phenomena are linked by fundamental physical and mathematical laws (Stull, 1988; Chow *et al.*, 2019; Bou-Zeid *et al.*, 2020). This section introduces the fundamental governing equations within Cartesian coordinates, encompassing the conservation equations for mass, momentum, and heat. Subsequently, the Reynolds averaging and decomposition method is presented as the basis for the eddy covariance (EC) approach. Additionally, the Monin-Obukhov similarity theory is introduced.

2.1. Governing Equations

The conservation of mass (i.e. continuity equation), momentum (i.e. Navier-Stokes equation, N-S equation), and heat (i.e. first law of thermodynamics) are described by the following equations in three-dimensional Cartesian coordinates.

$$\frac{\partial \rho}{\partial t} + \frac{\partial (\rho u_j)}{\partial x_j} = 0, \tag{2.1}$$

$$\frac{\partial u_i}{\partial t} + u_j \frac{\partial u_i}{\partial x_j} = -\delta_{i3} g - 2\epsilon_{ijk}\Omega_j u_k - \frac{1}{\rho}\frac{\partial P}{\partial x_i} + \frac{1}{\rho}\frac{\partial \tau_{ij}}{\partial x_j}, \tag{2.2}$$

$$\frac{\partial \theta}{\partial t} + u_j \frac{\partial \theta}{\partial x_j} = \upsilon_\theta \frac{\partial^2 \theta}{\partial x_j^2} - \frac{1}{\rho C_p}\left(\frac{\partial Q_j^*}{\partial x_j}\right) - \frac{L_p E}{\rho C_p}, \tag{2.3}$$

where ρ ($kg\ m^{-3}$) is the air density, t (s) is the time, u_j (ms^{-1})is the wind component in the j^{th} direction, p (Pa, or $kg\ m^{-1}s^{-2}$) is the air pressure, g ($m\ s^{-2}$) is the gravitational acceleration, τ ($kg\ m^{-1}s^{-2}$) is the viscous stress, θ (K) is the potential temperature, Q_j^* ($W\ m^2$) is the net radiation in the j^{th} direction, L_p ($J\ kg^{-1}$) is the latent heat associated with the phase change of E (i.e. mass of water vapour per unit volume per time, $kg\ m^{-3}s^{-1}$), and C_p ($J\ kg^{-1}K^{-1}$) is the heat capacity. Note the Einstein notation is used here, where δ_{i3} is the Kronecker Delta, $\delta_{mn} = \begin{cases} +1, & m = n \\ 0, & m \neq n \end{cases}$, and ϵ_{ijk} is the alternating unit tensor that $\epsilon_{ijk} = \begin{cases} +1, & ijk = 123, 231, or\ 312 \\ -1, & ijk = 213, 213, or\ 123 \\ 0, & for\ any\ two\ or\ more\ indices\ alike \end{cases}$.

The continuity equation (Eq. 2.1) serves to elucidate the fundamental concept of the conservation of mass, namely that the rate of change of mass within a control volume ($\frac{\partial \rho}{\partial t}$) is

equal to the net flux of mass across its boundaries ($-\frac{\partial(\rho u_j)}{\partial x_j}$). The N-S equation (Eq. 2.2) is Newton's second law of the fluids that describe the relationship between the motion of an object and the forces acting on it. Terms on the left-hand side of Eq. 2.2 are the storage of momentum ($\frac{\partial u_i}{\partial t}$), and the advection terms ($u_j \frac{\partial u_i}{\partial x_j}$), respectively. The right-hand side of Eq. 2.2 are the normalized forces to the weight, including the gravity ($-\delta_{i3} g$), the Coriolis effects ($2\epsilon_{ijk}\Omega_j u_k$), the pressure-gradient force ($\frac{1}{\rho}\frac{\partial P}{\partial x_i}$) and the viscous stress ($\frac{1}{\rho}\frac{\partial \tau_{ij}}{\partial x_j}$). The first law of thermodynamics (Eq. 2.3) describes the conservation of heat (i.e. enthalpy). The left-hand side of Eq. 2.3 are the storage of heat ($\frac{\partial \theta}{\partial t}$) and the advection term ($u_j \frac{\partial \theta}{\partial x_j}$), and the right-hand side of Eq. 2.3 are the are the molecular diffusion term ($\upsilon_\theta \frac{\partial^2 \theta}{\partial x_j^2}$), and the advection of sensible heat flux ($\frac{1}{\rho C_p}\left(\frac{\partial Q_j^*}{\partial x_j}\right)$) and latent heat flux ($\frac{L_p E}{\rho C_p}$), respectively.

2.2. Reynolds Decomposition and Averaging

Reynolds decomposition is a statistical technique that separates the mean value and the fluctuations from the original time series and/or spatial data. In the following equations, the vertical wind w and the scalar of interest c (e.g.u, v, θ) are selected as an example to illustrate the decomposition,

$$w(x,t) = \overline{w(x)} + w'(x,t), \tag{2.4 a}$$

$$c(x,t) = \overline{c(x)} + c'(x,t), \tag{2.4 b}$$

$$w(x,t) = \langle w \rangle(t) + \delta w(x,t), \tag{2.4 c}$$

$$c(x,t) = \langle c \rangle(t) + \delta c(x,t). \tag{2.4 d}$$

The overbar represents the temporal mean, the angle brackets represent the spatial mean. The prime symbol represents temporal fluctuation, whereas the delta symbol (δ) represents spatial fluctuation. The turbulent flux in temporal, spatial, and composite format is described as,

$$\overline{wc} = \overline{(\bar{c} + c')(\bar{w} + w')} = \overline{wc} + \overline{w'c'}, \tag{2.5 a}$$

$$\langle wc \rangle = \langle w \rangle \langle c \rangle + \langle \delta w \delta c \rangle, \tag{2.5 b}$$

$$\langle \overline{wc} \rangle = \langle \bar{w}\,\bar{c} + \overline{w'c'} \rangle = \langle \bar{w}\,\bar{c} \rangle + \langle \overline{w'c'} \rangle = \langle \bar{w} \rangle \langle \bar{c} \rangle + \langle \delta\bar{w}\delta\bar{c} \rangle + \langle \overline{w'c'} \rangle, \quad (2.5\ \mathrm{c})$$

respectively. The mean value of the fluctuation is equal to zero, which leaves only two terms on the right-hand side of Eq. 2.5a and 2.5b. These terms are the products of the temporal (or spatial) averaged w and c, and the covariance term (i.e. turbulent flux). In Eq. 2.5 c, the terms on the right-hand side are defined as the total vertical advection flux, dispersive flux, and turbulent flux, respectively.

2.3. Monin-Obukhov Similarity Theory

In the context of observations conducted in the 1930s, dimensional analysis showed that the ratio of the friction velocity (u_*) to the normalized mean velocity gradient ($z\frac{\partial u}{\partial z}$, with z representing the measurement height) is constant under neutral conditions ($\frac{z}{L} = -\frac{\left(\frac{g}{\theta}\right)(\overline{w'\theta'})_s}{\frac{u_*^3}{\kappa z}} \sim 0$, or $(\overline{w'\theta'})_s \sim 0$), designated as the von Kármán constant (κ), gives,

$$\kappa = \frac{u_*}{z\frac{\partial u}{\partial z}} \; or \; \frac{\kappa z}{u_*}\frac{\partial u}{\partial z} = 1. \quad (2.6)$$

To represent such a relationship in all atmospheric conditions, including buoyancy, a universal function of the atmospheric stability parameter ($\Phi_m(\frac{z}{L})$) has been incorporated, leading to the Monin-Obukhov similarity theory (MOST) as

$$\frac{\kappa z}{u_*}\frac{\partial u}{\partial z} = \Phi_m(\tfrac{z}{L}), \quad (2.7)$$

where the stability parameter ($\frac{z}{L} = -\frac{(g/\theta)(\overline{w'\theta'})_s}{u_*^3/(\kappa z)}$) represents the ratio of the buoyancy production to the mechanical production. Eq. 2.7 can also be expressed as

$$u_*^2 = \frac{\kappa z\, u_*}{\Phi_m(\frac{z}{L})}\frac{\partial u}{\partial z}, \quad (2.8)$$

where the momentum flux (u_*^2), or turbulent shear stress ($\rho\, u_*^2$), is proportional to the wind speed gradient ($\frac{\partial u}{\partial z}$), and the term $\frac{\kappa z\, u_*}{\Phi_m(\frac{z}{L})}$, which is also called the eddy viscosity (K_m).

A similar relationship applies to the profile of the potential temperature, gives

$$\frac{kz}{\theta_*}\frac{\partial \theta}{\partial z} = \Phi_h\left(\frac{z}{L}\right), \quad (2.9)$$

$$u_*\theta_* = \frac{kzu_*}{\Phi_h\left(\frac{z}{L}\right)}\frac{\partial \theta}{\partial z}, \quad (2.10)$$

where $\Phi_h(\frac{z}{L})$ is the university function of heat, and $\theta_* = \frac{(\overline{w'\theta'})_s}{u_*}$ is the temperature scaling parameter, $\frac{\kappa z\, u_*}{\Phi_h(\frac{z}{L})}$ is the eddy diffusivity (K_h). The methodology used to determine heat fluxes based on eddy diffusivity is also known as the gradient diffusion approach, or K-theory. It should be noted that the values of K_m and K_h are not necessarily identical, given that temperature is an active scalar influencing the flow field with feedback on heat fluxes themselves (Li, 2019). The ratio of $\frac{K_m}{K_h}$ is defined as the turbulent Prandtl number (Pr_t), and has been demonstrated that Pr_t increase with the incrase of the stability parameter (Högström and Bergström, 1996; Foken, 2006; Li, 2019).

In ESMs, the universal equation of $\Phi_m(\frac{z}{L})$ (also applies for $\Phi_h(\frac{z}{L})$) is expressed in the integral forms,

$$\psi_m\left(\frac{z}{L}\right) = \int_{z_{om/L}}^{z/L} \frac{[1-\Phi_m(x)]}{x}\, dx, \tag{2.11}$$

further gives,

$$|u_2| - |u_1| = \frac{u_*}{k}\left[\ln\left(\frac{z_2-d}{z_1-d}\right) - \psi_m\left(\frac{z_2-d}{L}\right) + \psi_m\left(\frac{z_1-d}{L}\right)\right]. \tag{2.12}$$

here u_2 (ms^{-1}) is the horizontal wind speed at height z_2 (m), and u_1 (ms^{-1}) is the horizontal wind speed at height z_1 (m), d (m) is the displacement height. By introducing the roughness length for momentum (z_{0m}) where wind speed decreases to zero, the wind speed in the atmosphere (V_a) is expressed as

$$V_a = \frac{u_*}{k}\left[\ln\left(\frac{z_{atm,m}-d}{z_{0m}}\right) - \psi_m\left(\frac{z_{atm,m}-d}{L}\right) + \psi_m\left(\frac{z_{0m}}{L}\right)\right], \tag{2.13}$$

by defining the aerodynamic resistance as

$$r_{am} = \frac{V_a}{u_*^2} = \frac{1}{\kappa^2 V_a}\left[\ln\left(\frac{z_{atm,m}-d}{z_{0m}}\right) - \psi_m\left(\frac{z_{atm,m}-d}{L}\right) + \psi_m\left(\frac{z_{0m}}{L}\right)\right]^2 \tag{2.14}$$

one can parameterize the momentum flux in the form of Ohm's law,

$$\tau = -\rho\, \frac{u_{atm}-u_s}{r_{am}}. \tag{2.15}$$

A similar formula applies to the heat flux,

$$H = -\rho\, C_p\, \frac{(\theta_{atm}-\theta_s)}{r_{ah}}, \tag{2.16}$$

with

$$r_{ah} = \frac{1}{\kappa^2 V_a}\left[\ln\left(\frac{z_{atm,m}-d}{z_{0m}}\right) - \psi_m\left(\frac{z_{atm,m}-d}{L}\right) + \psi_m\left(\frac{z_{0m}}{L}\right)\right]\left[\ln\left(\frac{z_{atm,h}-d}{z_{0h}}\right) - \psi_h\left(\frac{z_{atm,h}-d}{L}\right) + \psi_h\left(\frac{z_{0h}}{L}\right)\right]. \quad (2.17)$$

Chapter 3

3. Large-eddy Simulation of Soil Moisture Heterogeneity-induced Secondary Circulation with Ambient Winds

3.1. Publishing Information and Individual Contributions

This chapter has been published in *Quarterly Journal of the Royal Meteorological Society* (Zhang, Poll and Kollet, 2023). Co-authors are Dr. Stefan Poll and Prof. Dr. Stefan Kollet. Lijie Zhang is the first author of this study and is responsible for the methodology development, LES simulations, data curation, formal analysis, visualization and the original draft. Stefan Poll contributes to the software implementation, data curation, and formal analysis. Stefan Kollet is responsible for the conceptualization, the acquisition of funding, and the administration of the project. He also assists in interpreting and discussing the results and reviewing and editing the process.

3.2. Summary

Soil moisture heterogeneity in conjunction with ambient winds influences the convective boundary layer (CBL) by affecting the distribution of incoming solar radiation and forming secondary circulations. This study performed coupled large-eddy simulation (ICON-LEM) with a land surface model (TERRA-ML) over a flat river corridor mimicked by soil moisture heterogeneity to investigate the impact of ambient winds on secondary circulations. The coupled model employed double-periodic boundary conditions with a spatial extend and resolution of 4.8 km and 50 m, respectively. All simulations used the same idealized initial atmospheric conditions with constant incident radiation of 700 Wm^{-2} and various ambient winds with different speeds (0 to 16 ms^{-1}) and directions (e.g., cross-river, parallel-river, and mixed).

Based on phase-wind decomposition as outlined by Patton *et al.,* (2005), the atmospheric states are decomposed into ensemble-averaged, mesoscale, and turbulence, respectively. The results show that the secondary circulation structure persists under the parallel-river wind conditions independently of the wind speed but is destroyed when the cross-river wind is stronger than the phase wind speed, which is 2 ms^{-1} in this study. The soil moisture and wind speed determine the influence on the surface energy distribution independent of the wind direction.

However, secondary circulations increase the total vertical advection flux and dispersive flux while decreasing the turbulent flux.

A metric for secondary circulation strength was proposed based on the results of a dimensional analysis. The proposed metric indicates that the normalized maximum value of mesoscale vertical wind variance in the vertical profile may be employed as an indicator of secondary circulation strength. The secondary circulation strength positively scales with the Bowen ratio, stability parameter, and thermal heterogeneity parameter under cross-river wind and mixed wind conditions. The proposed similarity analysis and scaling approach provide a new quantitative perspective on the impact of the ambient wind under heterogeneous soil moisture conditions on secondary circulations.

Chapter 4

4. Assessing the Performance of Flux Imbalance Prediction Models Using Large Eddy Simulations over Heterogeneous Land Surface

4.1. Introduction

The eddy-covariance (EC) technique serves as a tool to determine the exchange of energy, water, and trace gases at the Land-Atmosphere (L-A) interface, improving our understanding of the dynamics and the feedback (Baldocchi, 2003, 2020; Pastorello *et al.*, 2020). To date, data from over 900 EC stations worldwide are available through the FLUXNET2015 Dataset (Pastorello *et al.*, 2020), covering a diverse range of climates and land covers (https://fluxnet.org/sites/site-summary/, latest access on 30th May 2024). With the establishment of networks like AmeriFlux (Novick *et al.*, 2018; Chu *et al.*, 2023), EuroFlux (Aubinet *et al.*, 1999; Franssen *et al.*, 2010), and AsiaFlux (Yamamoto *et al.*, 2005), numerous additional stations currently being installed, providing a benchmark for the development, validation, and prediction of earth system models (ESMs) (Baldocchi *et al.*, 2001; Rebmann *et al.*, 2018; Pastorello *et al.*, 2020).

A significant challenge in EC measurement arises due to the discrepancy between the measured sensible (H) and latent (LE) heat fluxes and the available energy (net radiation Rn minus the ground heat flux G), leading to the surface energy balance (SEB) closure problem (i.e. $H + LE < R_n - G$) (Foken, 2008; Foken *et al.*, 2010; Mauder, Foken and Cuxart, 2020). The reason for this inconsistency is still debated. However, it is generally agreed upon that the inherent assumptions of the EC method, such as Taylor's frozen turbulence hypothesis (Mauder *et al.*, 2013), statistical stationarity (Franssen *et al.*, 2010), and horizontal homogeneity (Eder, De Roo, *et al.*, 2015), are often not fulfilled, especially over complex terrains (Mauder, Foken and Cuxart, 2020). A degree of underestimation of sensible heat flux between 10% and 30% has been consistently reported across sites (Twine *et al.*, 2000; Wilson *et al.*, 2002; Barr *et al.*, 2006; Franssen *et al.*, 2010; Stoy *et al.*, 2013). The possible sources of error remain a topic of discussion in the community, including but not limited to measurement errors, missed additional terms related to energy conversion and storage, inadequate sampling over a finite mean period, and phase lag existing between vertical wind and water vapour, among others. For more details, interested readers are referred to the review papers (Foken, 2008; Mauder, Foken and Cuxart, 2020; Sun *et al.*, 2021).

Many studies aimed to identify the key factors impacting the flux imbalance (*FI*, a ratio of nonlocal scale flux to the total reference flux) through the analysis of EC data, considering direct measurement states and prognostic variables, including wind speed ($U = (u^2 + v^2)^{\frac{1}{2}}$, where u and v are the longitudinal and lateral velocity components along the cartesian coordinates x and y, respectively), time average interval (T), friction velocity ($u_* = \left(\overline{u'w'}^2 + \overline{v'w'}^2\right)^{\frac{1}{4}}$, convective velocity scale ($w_* = \left[\frac{g\, z_i}{\overline{\theta_v}}(\overline{w'\theta'})_s\right]^{\frac{1}{3}}$, g is the gravitational acceleration, θ_v is the potential temperature and z_i is the boundary layer height), stability parameters (z/L or z_i/L, *L is* the Obukhov length) and others (Zhou, Li and Li, 2019). A diminished *FI* is frequently observed with higher wind speeds or friction velocities, particularly during unstable weather conditions (Franssen *et al.*, 2010). Furthermore, an increase in the averaging time also results in a decrease in the *FI*, as the averaging operator acts as a high-pass filter. However, the averaging time is limited by the requirement of Taylor's frozen turbulence hypothesis for the stationarity, typically in 15, 30, or 60 minutes (Mauder *et al.*, 2013). Conversely, *FI* is often reported to increase with an increase in the measurement height and the atmospheric instability (Twine *et al.*, 2000; Wilson *et al.*, 2002; Finnigan *et al.*, 2003; Franssen *et al.*, 2010; Stoy *et al.*, 2013; Zhou and Li, 2019). It was also reported that there was a phase difference between the vertical wind velocity and scalar states. With a greater phase difference, there is a greater *FI* (Gao *et al.*, 2016; Gao, Russell, *et al.*, 2017).

Extensive research efforts have been devoted to large eddy simulation (LES) to explore the land-atmosphere interactions (Shen and Leclerc, 1994; Gopalakrishnan and Avissar, 2000; Albertson, Kustas and Scanlon, 2001; Maronga and Raasch, 2013; Patton *et al.*, 2016) and the *FI* (Kanda *et al.*, 2004; Inagaki *et al.*, 2006; Steinfeld *et al.*, 2007; Huang, Lee and Patton, 2008; De Roo *et al.*, 2018; Zhou, Li and Li, 2019; Margairaz, Pardyjak and Calaf, 2020a, 2020b; Wanner, Calaf and Mauder, 2022; Zhou, Sühring and Li, 2023). Several semi-empirical *FI* prediction models have been proposed based on LES. For instance, Huang *et al.,* (2008), hereafter H08, proposed a *FI* prediction model as a function of stability parameters (u_*/w_*), and the ratio of measurement height to the boundary layer height (z/z_i) over a homogeneous land surface. The H08 model is based on a simple shape function and can capture the *FI* in their simulation within the range of 0.3 z_i to 0.5 z_i. An evaluation study by Eder et al. (2014) based on observations in the Bavarian Alps and the Pre-Alps indicates that the H08 may not be able to accurately account for energy balance in complex terrain. Nevertheless, further testing

of its validity is still required. In our study, we conducted an evaluation of the H08 based on the LES output, demonstrating the significance of measurement height in *FI* estimates.

With the advancement in computational power, De Roo *et al.,* (2018) build on the work of H08 by using nesting techniques to increase the vertical resolution to 2 m (Hellsten *et al.*, 2021) and fitting the *FI* prediction model based on the data within the atmospheric surface layer (ASL), which is roughly 0.1 z_i (Stull, 1988), hereafter De18. Additionally, De18 has been successfully applied to EC data from three sites, including a beech forest site in Denmark and two pre-alpine grass sites in Germany, demonstrating a promising outcome for reducing the *FI* and closing the surface energy balance (Mauder *et al.*, 2021). Wanner *et al.,* (2022) extended the model, hereafter W22, to account for land surface heterogeneity by incorporating the thermal heterogeneity parameter (Margairaz, Pardyjak and Calaf, 2020b). The W22 model was fitted to the LES data, accounting for varying heterogeneity scales. This process resulted in the creation of semi-empirical *FI* prediction equations, each with its own set of parameters corresponding to the different heterogeneity scales.

Based on the cospectral analysis of the vertical wind velocity and potential temperature, (Zhou, Li and Li, 2019) proposed a conceptual model to explain the *FI* with a semi-empirical formation of four variables, including the stability parameter (-z_i/L, note that $-z_i/L = -\kappa\frac{w_*^3}{u_*^3}$ under unstable conditions, with κ being the von Kármán constant of 0.40), wind speed (U), time average interval (T) and integral length scale of vertical velocity ($l_w = \int_0^\infty R(r)dr$, with $R(r)$ as a autocorrelation function), providing a potential approach to diagnose the *FI*. A further study by (Zhou, Sühring and Li, 2023) compared the performance of H08, De18, and Z19 using LES data over a 1-D stripe heterogeneity pattern with prescribed sensible and latent heat fluxes. Zhou *et al.,* (2023) suggest that the *FI* prediction model performs poorly at the single-pixel scale. However, integrating the footprint model enhances its performance. Among the three models (H08, De18, Z19), Z19 demonstrates superior performance compared to H08 and De18 with their data. In addition, Z19 can be applied under all atmospheric stability conditions, whereas the other two models are only valid under unstable conditions.

Recent studies have shown that the *FI* is positively related to atmospheric instabilities, associated with the imbalance between the ejecting and sweeping contributions to the heat flux. For instance, based on the EC measurement from dryland (Hanford Site, Washington, USA), (Gao *et al.*, 2020) show that with the increase of atmospheric instability, the flux contribution from sweeps ($w' < 0, \theta' < 0$) decreases, while the flux contribution from ejections ($w' >$

$0, \theta' > 0$) remains constant (Fig. 8 in their work). In a separate study, based on observations from a 225 m meteorological tower in an urban environment (Tianjin, China), (Zhang *et al.*, 2023) reported that with the increase of atmospheric instability, the flux contribution from ejections increases slightly, and the flux contribution of sweeps remains constant (Fig. 3 in their study). Despite slight inconsistencies in each component, the trend remains the same: the difference in flux contribution between the sweeps and ejections increases as the instability increases. This asymmetric transport phenomenon provides insight into the underestimation of turbulent heat fluxes (Li, Katul and Liu, 2018; Liu, Gao and Katul, 2021). Further analysis of the asymmetric transport over the LES data can shed light on the mechanics of the *FI* within the ASL (Liu *et al.*, 2024).

There is increasing scientific interest in understanding the mechanics of *FI* and utilizing this knowledge to improve EC measurements. However, few studies have focused on the validity of flux imbalance prediction models. For example, Zhou *et al.*, (2023) compared three *FI* prediction models over a 1-D stripe heterogeneity surface with prescribed sensible and latent heat flux. Further evaluation of available *FI* prediction models over more complex terrain (i.e., 2-D heterogeneity) at different heterogeneity scales is needed to interrogate the robustness of these models. In order to achieve this objective, this study conducts a series of large eddy simulations coupled with a land surface model (LES-LSM) over a checkerboard pattern of soil moisture heterogeneity. This study aims to evaluate four selected *FI* prediction models and investigate the role measurement height played in the *FI* through the quadrant analysis. This chapter is organized as follows: Section 4.2 presents the *FI* prediction models and the model and simulation setup. Section 4.3 presents the results and a brief discussion. Section 4.4 presents the summary and conclusion.

4.2. Methods

4.2.1. Flux Imbalance

4.2.1.1. Flux Imbalance Estimation

To illustrate *FI*, we take the vertical wind speed (w) and potential temperature (θ), respectively, as examples, presenting them in both temporal and spatial domains using the Reynolds decomposition (Finnigan and Shaw, 2008), as

$$w(x,t) = \overline{w(x)} + w'(x,t), \tag{4.1 a}$$

$$\theta(x,t) = \overline{\theta(x)} + \theta'(x,t), \tag{4.1 b}$$

$$w(x,t) = \langle w \rangle(t) + \delta w(x,t), \tag{4.2 a}$$

$$\theta(x,t) = \langle \theta \rangle(t) + \delta\theta(x,t). \tag{4.2 b}$$

The temporal mean is indicated by an overline, and the spatial horizontal mean is indicated by the angle bracket. A prime symbol denotes the temporal fluctuation, and the symbol δ represents the spatial fluctuation. The total vertical heat flux at a given height (De Roo and Mauder, 2018b) is described as

$$\langle \overline{w\theta} \rangle = \langle \overline{w} \rangle \langle \overline{\theta} \rangle + \langle \delta\overline{w}\delta\overline{\theta} \rangle + \langle \overline{w'\theta'} \rangle. \tag{4.3}$$

On the right-hand side of Eq. 4.3, the terms correspond to the mean vertical advection flux, the dispersive flux, and the eddy-covariance flux (i.e., turbulent heat flux), respectively. An important observation is that the vertical wind $\overline{w}$ does not exhibit a zero value at the point scale when a heterogeneous land surface experiences continuous heating under free convection conditions (Prabha, Karipot and Binford, 2007).

The dispersive flux has been consistently recognized as an important factor in achieving the closure of the surface energy balance (Kanda *et al.*, 2004; Mauder, Foken and Cuxart, 2020). Research has shown that dispersive fluxes account for about 5% - 10% of the total sensible heat flux in the lower atmosphere, and this contribution increases with height, potentially reaching over 40% at heights above 100 m over an arid landscape (Margairaz, Pardyjak and Calaf, 2020a).

The *FI* is often defined as the nonlocal scale flux (i.e., difference between the total reference heat flux and the turbulent heat flux) to the total reference heat flux (Kanda *et al.*, 2004; Inagaki *et al.*, 2006; Huang, Lee and Patton, 2008; De Roo *et al.*, 2018; Zhou, Li and Li, 2019; Wanner *et al.*, 2022, 2024; Zhou, Sühring and Li, 2023). In the literature, different selections of total reference heat flux have been proposed, including either the total heat flux within the atmosphere ($\langle \overline{w\theta} \rangle$, first row in Table 4.1), or surface heat flux ($\langle \overline{H_{surf}} \rangle$, second row in Table 4.1, often employed in studies with prescribed surface heat flux). In order to be consistent with the majority of previous research, we have followed the methodology outlined in the first row of Table 3.1 for the data processing. It can be reasonably assumed that the two definitions will have a negligible effect on the results, given that the sensible heat flux within the lower atmosphere is nearly constant (Baldocchi *et al.*, 2001).

Furthermore, a novel definition of *FI* has been put forth by Morrison *et al.,* (2022), which is the ratio of the total reference heat flux in the atmosphere to the turbulent heat flux. In the event of a perfect balance, the value is 1. Conversely, any underestimation yields a value greater than 1. The definition is also listed as the third row in Table 4.1 for reference.

Table 4.1: Different definitions of *FI* in the literature

Equations	Reference
$\langle \mathrm{I} \rangle = \frac{\langle \overline{\mathrm{w}\theta} \rangle - \langle \overline{\mathrm{w}'\theta'} \rangle}{\langle \overline{\mathrm{w}\theta} \rangle}$	(Kanda *et al.*, 2004; Inagaki *et al.*, 2006; Steinfeld *et al.*, 2007; Huang, Lee and Patton, 2008; Schalkwijk, Jonker and Siebesma, 2016; Y. Zhou *et al.*, 2018)
$\langle \mathrm{I} \rangle = \frac{\langle \overline{\mathrm{H}_{\mathrm{surf}}} \rangle - \langle \overline{\mathrm{w}'\ \theta'} \rangle}{\langle \overline{\mathrm{H}_{\mathrm{surf}}} \rangle}$	(De Roo *et al.*, 2018; Zhou, Li and Li, 2019; Wanner, Calaf and Mauder, 2022)
$\langle I \rangle = \frac{\langle \overline{\mathrm{w}'\theta'} \rangle + \langle \delta\overline{w}\delta\overline{\theta} \rangle + \langle \overline{w} \rangle \langle \overline{\theta} - \overline{\theta}_{ref} \rangle}{\langle \overline{\mathrm{w}'\theta'} \rangle}$	(Morrison *et al.*, 2022; Morrison, Calaf and Pardyjak, 2023)

4.2.1.2. Flux Imbalance Prediction Models

Numerous research efforts have been dedicated to determining the *FI* with statistical models considering turbulence characteristics, as mentioned in the introduction. To gain a better understanding of the value and usefulness of these models, we selected four *FI* prediction models for a comprehensive evaluation. The models are H08, De18, Z19, and W22, with the semi-empirical formulas shown in Table 4.2. Notably, this study excluded the approach suggested by (Panin and Bernhofer, 2008) for using the effective roughness length, because a uniform roughness length of 0.1 m was applied across all simulations in our study.

Table 4.2: *FI* prediction models in the literature

Notation	*FI* Prediction Model	Application Range	Reference
H08	$\langle I \rangle = \left[\exp\left(4.2 - 16\,\frac{u_*}{w_*}\right) + 2.1\right]\left[1.1 - 8.0\left(\frac{z}{z_i} - 0.38\right)^2\right]^{0.5}$	0.3 z_i ~ 0.5 z_i	(Huang, Lee and Patton, 2008)
De18	$\langle I \rangle = \left[0197\exp\left(-17.0\,\frac{u_*}{w_*}\right) + 0.156\right]\left[0.21 + 10.69\,\frac{z}{z_i}\right]$	< 0.1 z_i	(De Roo *et al.*, 2018)
Z19	$\langle I \rangle = 1 - \left[-1.46\,\frac{z}{z_i} + 1.0\right]\left[-0.05\,\frac{z_i}{L}\,\frac{l_w}{U\,T} + 0.95\right]$	0.03 z_i ~ 0.1 z_i	(Zhou, Li and Li, 2019)
W22	$\langle I \rangle = \left[a\exp\left(b\,\frac{u_*}{w_*}\right) + c\right]\left[20.05\,\frac{z}{z_i} + 0.157\right]\left[H_{par}\right]$	< 0.1 z_i	(Wanner, Calaf and Mauder, 2022)

In Table 4.2, $u_* = \left(\overline{u'w'}^2 + \overline{v'w'}^2\right)^{\frac{1}{4}}$ is the friction velocity, $w_* = \left[\frac{g\, z_i}{\overline{\theta_v}}(\overline{w'\theta'})_s\right]^{\frac{1}{3}}$ is the convective velocity scale, z is the measurement height, z_i is the boundary layer height defined as the height where the sensible heat flux profile has its minimum, $L = \frac{-u_*^3 \theta_v}{k\, g\, \overline{w'\theta'}}$ is the Obukhov length, U is the mean horizontal wind speed, $l_w = \int_0^\infty R(r)dr$ is the integral length scale of vertical velocity, and R(r) is the autocorrelation function (Zhou, Li and Li, 2019), $H_{par} = \frac{g\, l_h}{U^2}\frac{\Delta T}{\overline{T}}$ is the thermal heterogeneity parameter (Margairaz, Pardyjak and Calaf, 2020b). Details of the scaling parameters are described in the Appendix 1.

It is important to note that the parameters *a*, *b*, and *c* in W22 are scale-dependent and were explicitly designed for heterogeneity scales of 200 m, 400 m, and 800 m in the original study. Therefore, they are labeled W22-200m, W22-400m, and W22-800m. To align closely with the heterogeneity scale in our simulation setting, we compared the simulations with heterogeneity scales of 2400 m (s2400), 1200 m (s1200), and 600 m (s600) to W22-800m. However, this comparison may lead to uncertainties in the model's performance. The same approach applies to the remaining scenarios in which we compare the simulations with a heterogeneity scale of 300 m (s300) to W22-400m and a heterogeneity scale of 150 m (s150) and 50 m (s50) to W22-200m.

4.2.2. Data and Processing

4.2.2.1. Model Description

In this study, a dataset was generated using an LES model, ICON-LEM, coupled with a land surface model, TERRA-ML, at various scales of land surface heterogeneity. The ICON (Icosahedral Nonhydrostatic) framework is a collaboration between the German Weather Service (DWD), the Max Planck Institute for Meteorology (MPI-M), German Climate Computing Centre (DKRZ), Karlsruhe Institute of Technology (KIT) and the Centre for Climate Systems Modelling (C2SM). ICON was originally developed for research and operational purposes in numerical weather prediction and climate modelling (Zängl *et al.*, 2015). The ICON framework enables the implementation of a LES mode (ICON-LEM) (Dipankar *et al.*, 2015a). ICON-LEM uses the 3D Smagorinsky turbulence scheme to account for the SGS contribution. The performance of ICON-LEM has been extensively evaluated over a large spatial domain in Germany, as reported in the study of (Heinze *et al.*, 2017). Furthermore, ICON-LEM has been used in various scientific investigations, including studies

on mesoscale secondary circulations (Han *et al.*, 2019), high-CAPE (convective available potential energy) (Rybka *et al.*, 2021), Atmospheric Boundary Layer (ABL) tuning parametrization (Poll, Shrestha and Simmer, 2022), cloud properties and precipitation (Verma and Burkhardt, 2022), and many others. For a comprehensive explanation of the parameterizations of ICON-LEM, interested readers are referred to Dipankar et al. (2015).

The ICON framework comprises the land surface model TERRA-ML that enables two-way coupling between the land surface and the atmosphere (Grasselt *et al.*, 2008; Schulz and Vogel, 2020). TERRA-ML estimates the sensible and latent heat flux at the land surface using the following equations and provides soil temperature and soil moisture as lower boundary layer conditions.

$$H = \rho C_p C_h |U| \left(\theta\, \pi_{sfc} - T_{sfc}\right), \tag{4.4}$$

$$LE = \rho L_v \frac{q_v - q_{sav}}{r_a + r_s}, \tag{4.5}$$

where H ($W\ m^{-2}$) is the sensible heat flux at the land surface, ρ is the air density ($kg\ m^{-3}$), C_p and C_h are the heat capacity ($J\ kg^{-1}K^{-1}$) and the bulk transfer coefficient (-), respectively, θ is the air potential temperature (K), and T_{sfc} is the ground surface temperature (K), with π as the scaled pressure at the ground surface (-). r_a denotes the aerodynamic resistance, and $r_s = r_{s,min}\left(\frac{\theta_1 - \theta_{adp}}{\theta_{fc} - \theta_{adp}}\right)^{-1}$ is the soil resistance, with $r_{s,min}$=50 ms^{-1}, while θ_{adp} (K) and θ_{fc} (K) are the air dryness point and field capacity (Schulz and Vogel, 2020).

4.2.2.2. Simulation setup

In this study, the spatial resolution of the simulation was set to 50 m in both the x and y directions, covering an area of 4.8 km × 4.8 km with a double periodic boundary setting. This spatial configuration is considered suitable for capturing the mesoscale secondary circulation while ensuring computational efficiency (Han *et al.*, 2019; Zhang, Poll and Kollet, 2023). The vertical grid consists of 420 levels with a resolution of 10 m, extending to a height of 4.2 km. A sponge layer with Rayleigh damping of the vertical velocity component was incorporated into the model at an altitude of 3,700 m and above, with a depth of 500 m (the upper 8.3%) to nudge the atmosphere at the upper atmospheric boundary layer. The initial height of the boundary layer was set to 1,000 m, with a constant potential temperature of 290 K below. Above 1,000 m, the potential temperature was set to increase at a lapse rate of 0.006 $K\ m^{-1}$.

Each simulation was conducted for a duration of 8 hours, with a temporal step of 0.5 seconds for both ICON-LEM and TERRA-ML that coupled in every time step. A fixed incoming radiation of 700 $W\ m^{-2}$ at the top of the atmosphere and a flat terrain ensure the tractability of the problem, as incorporating the diurnal variations in radiation (Y. Zhou *et al.*, 2018) or accounting for complex terrain (Rihani, Chow and R. Maxwell, 2015) would introduce additional complexity into to the system. It should be noted that the Coriolis effect and the background wind have not been incorporated into the simulation.

The use of a two-dimensional checkerboard pattern has been widely used in various studies, including the application of prescribed heat fluxes (Lee, Zhang and Klein, 2019), temperature (Margairaz, Pardyjak and Calaf, 2020b; Wanner, Calaf and Mauder, 2022) and soil moisture (Huang and Margulis, 2009). This work used a classical checkerboard pattern of soil moisture (Figure 4.1) with the same horizontal grid size as the atmosphere (i.e., 50 m). Patch sizes varied from 50 m to 2,400 m, allowing for different scales of spatial heterogeneity. The soil moisture distribution included two values: 0.55 cm^3cm^{-3} for the wet region and 0.25 cm^3cm^{-3} for the dry region, with a domain-averaged value of 0.40 cm^3cm^{-3}. Although TERRA-ML comprises eight soil layers reaching a maximum depth of 15 m, the variation in the soil moisture profile was not considered due to the simulation's limited time of 8 hours. Note, while ICON uses unstructured grids instead of the traditional longitude-latitude grid (i.e., structured orthogonal grids), a checkerboard distribution of soil moisture can still be achieved through a remapping process (Wan *et al.*, 2013). The model output the instantaneous variables at a 15 minutes interval. In addition, a time step of 0.5 seconds is saved for the wind components and potential temperatures of the lowest ten layers during the last hour.

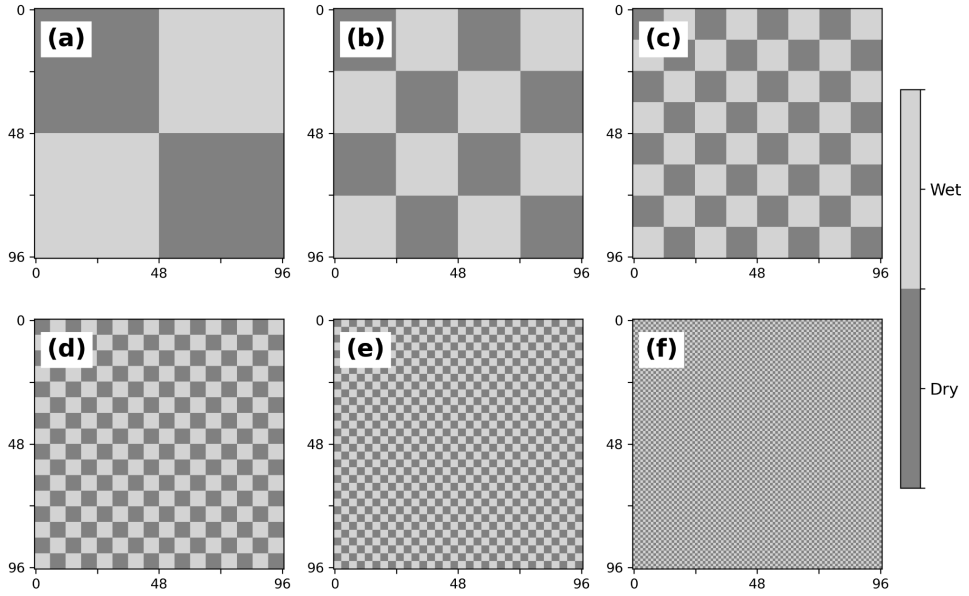

Figure 4.1: Initial distribution of soil moisture. (a) heterogeneity scale = 2,400 m, (b) heterogeneity scale = 1,200 m, (c) heterogeneity scale = 600 m, (d) heterogeneity scale = 300 m, (e) heterogeneity scale = 150 m, (f) heterogeneity scale = 50 m. The simulations are named s2400, s1200, s600, s300, s150 and s50, respectively. The dark colour has a value of 0.25 $cm^3 cm^{-3}$ and the light colour has a value of 0.55 $cm^3 cm^{-3}$ The spatial average is 0.40 $cm^3 cm^{-3}$. Additionally, an equivalent homogeneous simulation (Ho) is performed, see Appendix 2.

4.2.2.3. Quadrant analysis

The quadrant analysis method decomposes two turbulent fluctuations (e.g. w' and θ') into four quadrants, thereby determining the contribution and time fraction of turbulent heat flux from each quadrant. This approach has also been employed to investigate the dissimilarity between heat and momentum transport (Schmutz and Vogt, 2019; Gao *et al.*, 2020).

This study follows (Li and Bou-Zeid, 2011) definition of quadrant decomposition, which includes the ejections ($w' > 0,\ \theta' > 0$), the sweeps ($w' < 0,\ \theta' < 0$), the inward interaction ($w' > 0,\ \theta' < 0$), and the outward interaction ($w' < 0,\ \theta' > 0$). The average fluxes within each quadrant can be expressed in Eq. 4.6, as

$$\overline{w'\theta'}_k = \frac{1}{N}\sum_{t=1}^{N} w'\theta'\, I_k\,(t), \tag{4.6}$$

where $I_k(t)$ is an indicator variable with a weight of one if the sample is in the corresponding quadrant, otherwise it has a weight of zero. The flux contribution $S(i)$ and time fraction $T(i)$ can then be calculated using the following equations (Schmutz and Vogt, 2019),

$$S(i) = \frac{\overline{w'\theta'}_k}{\overline{w'\theta'}}, \tag{4.7}$$

$$T(i) = \frac{\sum_{n=1}^{N} I_k(t)}{N}. \tag{4.8}$$

4.3. Results and Discussions

4.3.1. Horizontal Cross-Section and Vertical Profiles

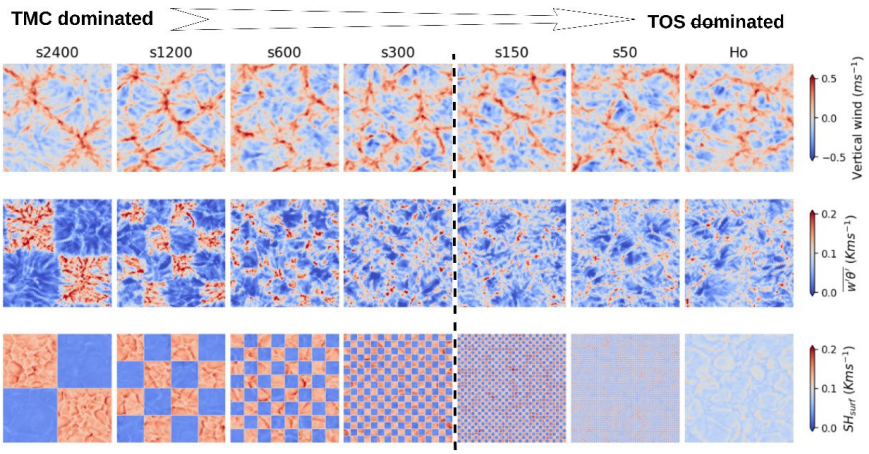

Figure 4.2: Cross section of temporal-averaged vertical wind at 50 m (half level), turbulent heat flux ($\overline{\boldsymbol{w'\theta'}}$) at 45 m (full level) and surface sensible heat flux ($\boldsymbol{SH_{surf}}$) at the land surface for the last hour of the simulation. At a large heterogeneity scale (on the left side), the atmospheric structure is dominated by the thermally-induced mesoscale circulation (TMC). At a small heterogeneity scale (on the right side), the atmospheric structure is dominated by the turbulent organized structure (TOS). The black dashed line represents the homogeneous equivalent line.

Figure 4.2 displays a clear cellular structure for the vertical wind velocity, characterized by narrow and intense updrafts and weak downdrafts. The air temperature over dry soil is higher than over wet soil with uniform incoming radiation. The air parcels over dry soil move upward due to buoyancy, which reduces and increases air pressure at the land surface and top of the ABL, respectively. Conversely, the air parcels over wet soil sinks, increasing air pressure at the land surface, leading to secondary circulations due to the horizontal pressure gradients. This phenomenon is commonly known as thermally-induced mesoscale circulation (TMC) and has been extensively documented in the literature (Wanner, Calaf and Mauder, 2022). A systematic discussion can be found in (Salesky, Chamecki and Bou-Zeid, 2017). Simulations s2400 and

s1200 show a prevalence of updrafts in the dry region. However, as the scale of heterogeneity decreases to 600 m and 300 m (i.e., s600 and s300), the connection between the updraft pattern and the dry region pattern becomes less pronounced, as also shown in Figure 4.11 in Appendix 3, that a point-to-point Pearson correlation coefficient between the turbulent heat flux at 45 m and the land surface heat flux decreased from 0.76 for s2400 to 0.27 for s300. Simulations s150 and s50 show a quasi-homogeneous random structure, similar to the homogeneous simulation, which has been previously reported as a slow-moving turbulent organized structure (TOS) (Kanda *et al.*, 2004). According to the classification by (Bou-Zeid *et al.*, 2020), land patches of s150 and s50 could be considered statistically homogeneous if they exhibit locally variable surface characteristics at a small scale, yet remain relatively uniform at the regional scale. The turbulent energy spectrum in Figure 4.10 of Appendix 3 also indicates that the difference between s150, s50, and the equivalent homogeneous case is negligible.

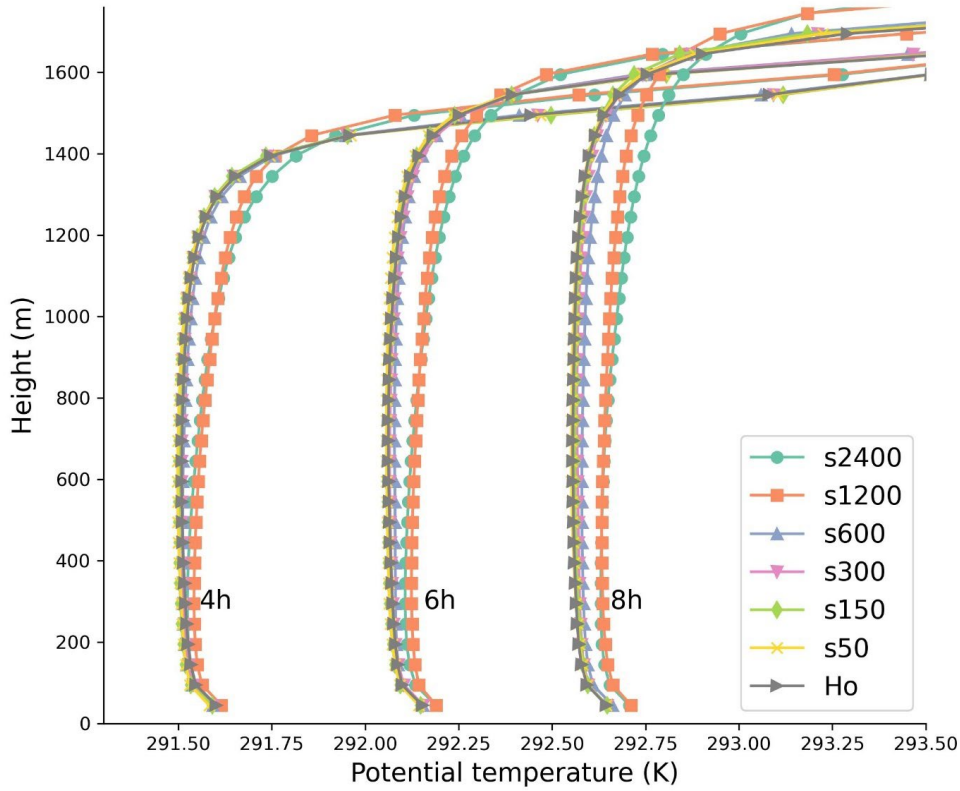

Figure 4.3: Vertical profile of the horizontal mean potential temperature at 4h, 6h and 8h.

In Figure 4.3, the potential temperature above the ASL remains constant until the boundary layer height is reached, as indicated by an almost vertical line. The potential temperature for simulations with larger heterogeneity scales (e.g. s2400, s1200) are slightly higher than those with smaller heterogeneity scales (e.g. s150, s50), which is consistent with the findings of previous studies (Raasch and Harbusch, 2001; Huang and Margulis, 2009; Han *et al.*, 2019; Zhou, Li and Li, 2019). Enhanced entrainment effects in simulations with larger heterogeneity scales may explain this behaviour, as shown in Figure 4.4.

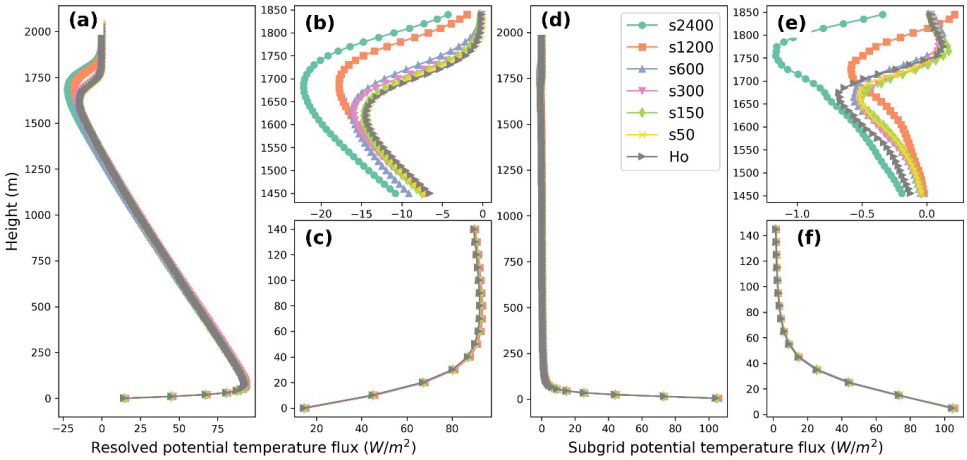

Figure 4.4: Profile of the resolved and subgrid scale potential temperature flux (i.e. turbulent heat flux) for the last hour of the simulation. Panels (a) and (d) show the resolved and subgrid scale potential temperature flux within the convective boundary layer. Panels (b) and (c) are magnifications of (a) showing details in the entrainment layer and ASL. The same applies to panels (e) and (f) to (d).

In Figure 4.4, the vertical profile of the potential temperature flux is depicted, showing a typical shape (Tennekes, 1973), where the resolved potential temperature flux decreases as height increases, reaching its maximum negative value at the entrainment layer. For simulation s2400, the maximum negative value observed was -23 $W\ m^{-2}$, which decreased to -17 $W\ m^{-2}$ for simulation s1200, and further decreased to -13 $W\ m^{-2}$ for the remaining cases up to a heterogeneity scale of 50 m. The significant influence of the subgrid-scale (SGS) contribution on the potential temperature flux near the surface layer is evident in Figure 4.4 f, which gradually decreases with increasing height. The lowest levels of the LES output are often excluded from the analysis because the flux is usually purely parameterized (De Roo and Mauder, 2018b; Zhou, Li and Li, 2019). However, surface-level data has been included in this

study to provide readers with a complete perspective on the role of SGS in atmospheric heat flux characteristics.

4.3.2. Impact of Heterogeneity Scale on the Atmospheric Structure

Table 4.3 shows the bulk statistics of the different simulations. Simulations with larger heterogeneity scales (s2400 and s1200) show a slightly higher boundary layer height (z_i, defined as the height where the sensible heat flux has its minimum), reaching 1,695 m compared to the simulations with smaller heterogeneity scales (e.g., 1,635 m for s300). Previous studies have consistently shown that the horizontal mean of the boundary layer height is relatively unaffected by the heterogeneity scales. For example, (Lee, Zhang and Klein, 2019) investigated a range of checkerboard patch sizes from 1.2 km to 14.4 km, which exceeded a typical boundary layer height, while Wanner *et al*., (2022) investigated patch sizes of 200 m, 400 m, and 800 m, which were smaller than a typical summer clear-sky boundary layer height. Both studies show insignificant variations in boundary layer height among the simulations with different heterogeneity scales. In our study, we found that despite the heterogeneity scale ranging from 50 m to 2,400 m that crosses from microscale to mesoscale, the difference in the boundary layer height is only around 40 m, which is less than 5%.

Table 4.3: Bulk statistics of various simulations

Case	Heterogeneity Scale (m)	z_i (m)	u_* (m s^{-1})	w_* (m s^{-1})	t_* (s)	Bowen ratio (-)	$-\frac{z_i}{L}$ (-)	H_{par} (-)
s2400	2,400	1695	0.297	1.60	1056	0.747	74.6	135.3
s1200	1,200	1695	0.323	1.60	1057	0.739	57.1	55.2
s600	600	1665	0.326	1.58	1050	0.730	54.8	30.3
s300	300	1635	0.348	1.57	1040	0.726	44.5	13.4
s150	150	1675	0.342	1.58	1061	0.722	47.6	6.7
s50	50	1635	0.345	1.56	1045	0.720	45.4	2.1
Ho	-	1635	0.344	1.57	1041	0.722	46.8	-

The values of u_* and w_* were calculated at a height of 45 m. The results indicate that as the heterogeneity scale decreases, u_* increases while w_* decreases, resulting in a slight decrease of the atmospheric stability (-z_i/L). The Bowen ratio decreased with a decreasing heterogeneity scale, shifting from 0.747 to 0.720. However, z_i does not consistently decrease with the decrease in heterogeneity scale. Additionally, s300 exhibits the lowest z_i and -z_i/L values, which will be discussed below. On the other hand, the difference of large-eddy turnover time

scale $t_* = \frac{z_i}{w_*}$ among the simulations with different heterogeneity scales is negligible, with a value range between 1040 s to 1061 s, which is roughly 17 mins.

One possible explanation for the non-monotonic effects of the heterogeneity scale on the atmosphere's structure, supported by Figure 4.2, is that the atmosphere is significantly influenced by the TMC at sufficiently large heterogeneity scales. In contrast, at smaller heterogeneity scales, the formation of the TMC appears to be less pronounced, and the mesoscale circulation pattern is dominated by the TOS. Nevertheless, the various secondary circulation schemes do not appear to have an impact on the performance of the *FI* prediction model, see section 4.3.3 for details.

4.3.3. Flux Imbalance Prediction Model Evaluation

This section analyses the vertical sensible heat flux components, which comprise the turbulent heat flux, the mean vertical advection flux, and the dispersive flux at various measurement heights. Based on these components, we assess four *FI* prediction models selected from the literature, as listed in Table 4.2.

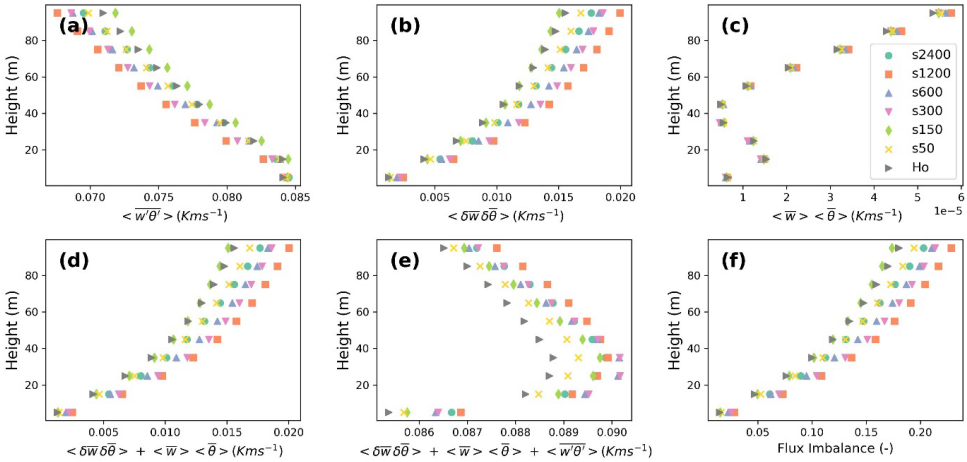

Figure 4.5: Flux components and *FI* for the last hour of simulation. The first row shows the turbulent heat flux including the SGS contribution, the dispersive flux and the mean vertical advection flux, respectively. The second row shows the sum of the vertical advective and dispersive heat flux, the total reference heat flux and *FI*. Noted that the *FI* is dimensionless. A reference temperature is included to calculate the mean vertical advection flux based on (Morrison *et al.*, 2022), which is set as the mean value of the previous hour.

Figure 4.5 shows the different components of the vertical heat flux and the *FI* within the ASL. The turbulent heat flux (including the SGS contribution) decreases with height, while the

dispersive flux increases with height. The results agree with Margairaz et al.'s (2020a) findings that the contribution of the dispersive component to the total heat flux increases from 10% to 40% as the height increases from near surface to above 100 m. The mean vertical advection flux calculation in this study includes a reference potential temperature (Morrison *et al.*, 2022). The mean vertical advection fluxes exhibit fluctuations in the lower levels, up to 45 m, before increasing with height. However, the mean vertical advection fluxes are several magnitudes smaller than the turbulent heat fluxes and the dispersive heat fluxes. This suggests that the mean vertical advection fluxes may be ignored in modelling efforts. For example, (Wanner *et al.*, 2024) also show that properly modelling the dispersive flux is the key to closing the energy balance.

The *FI* shows non-monotonicity across the heterogeneity scale and increases from s150 to s1200, reaching a maximum, then decreasing again at s2400. A similar result has been reported by (Zhou, Li and Li, 2019), who found that the *FI* decreases when the surface heterogeneity scale becomes larger than the boundary layer height. This may be due to the flows behaving like a homogeneous surface at scales below the heterogeneity scale, which minimizes the impact of the dispersive fluxes. Furthermore, case s50 exhibits a greater *FI* than s150. This is because case s50 has one grid cell size patch, so any adjustment of the surface fluxes from a transition is missing.

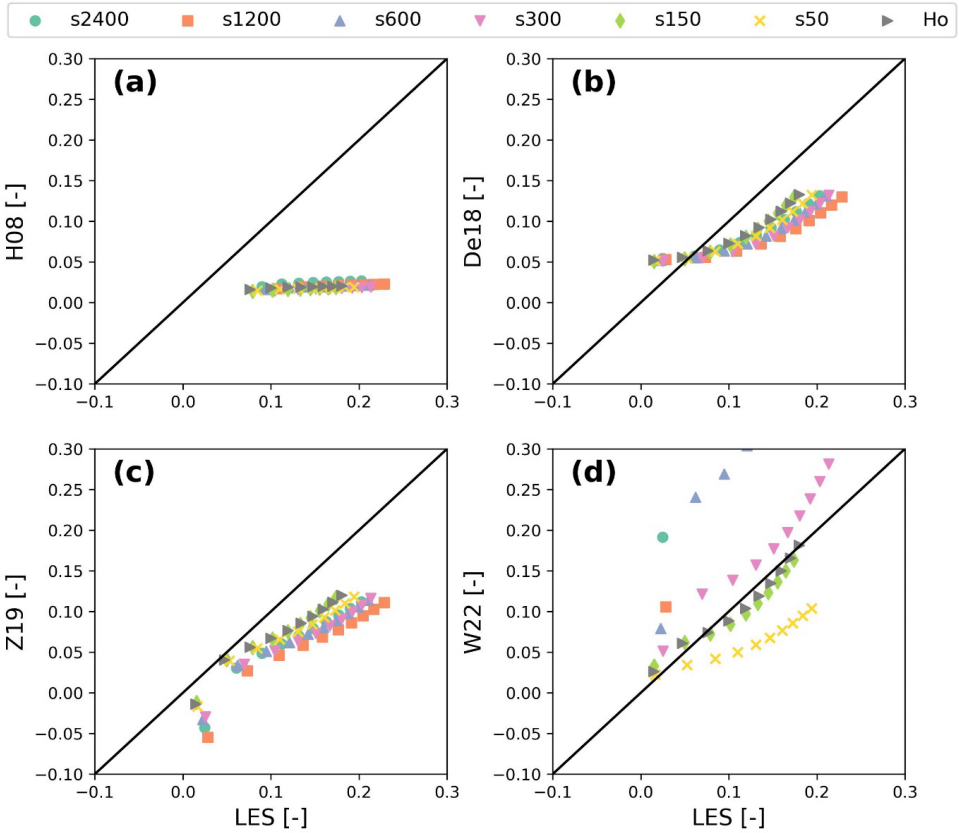

Figure 4.6: Performance of the *FI* prediction models for the bottom ten layers. (a) H08, (b) De 18, (c) Z19 (d) W22. The x-axis represents the *FI* calculated from LES data, and the y-axis displays *FI* estimated by the *FI* prediction models. Note that *FI* increases consistently with height.

Figure 4.6 shows the performance of the four *FI* prediction models considered. The performance of H08 is relatively worse compared to the other models. This is because H08 is fitted with data obtained between 0.3 z_i to 0.5 z_i, which extends beyond the atmospheric surface layer (ASL) and limits its direct applicability to the ASL *FI* estimates. Similar conclusions have been drawn by Eder *et al.*, (2014). Furthermore, if z/z_i is less than 0.01, (i.e., z = 17 m with z_i = 1700 m), the value within the square root in H08 formula becomes negative, resulting in a singularity. Therefore, the data below 15m is excluded in Figure 4.6a. Nevertheless, in our opinion, the concept of H08 is useful for quantifying *FI* based on atmospheric stability and relative measurement height in the mixing layer.

De18 produces results comparable to those obtained from the LES, even though it was originally developed from simulations over a homogeneous land surface. The results show a

slight overestimation of *FI* near the surface and an underestimation with increasing height. Z19, compared to De18, shows a similar performance in predicting the *FI*. In the first layer near the land surface (i.e. z = 5m), Z19 provides a negative imbalance, which is also reported by Zhou *et al.*, (2019) (Figure. C2 in their paper). This can be explained by the fact that Z19 was constructed with a data range of 0.03 z_i to 0.1 z_i, which is larger than 5 m.

W22 performs best when the heterogeneity scale is well matched, such as s300 and s150. However, W22 tends to significantly overestimate the *FI* for simulations with a larger heterogeneity scale, resulting in unreasonable values (not shown in the figure). Consequently, directly applying W22 in the climate model presents a challenge, particularly for grid sizes at the several-kilometre scale.

4.3.4. Quadrant Analysis

The turbulent flux is mainly attributed to the contributions from the ejections ($w' > 0, \theta' > 0$) and sweeps ($w' < 0, \theta' < 0$) (Högström and Bergström, 1996). Several studies indicate that the difference between the contributions from ejections and sweeps increases with atmospheric instability, leading to an increase in the *FI* (Gao *et al.*, 2020; Liu, Gao and Katul, 2021). To investigate the potential correlation between *FI* and height, a quadrant analysis was conducted at different measurement heights.

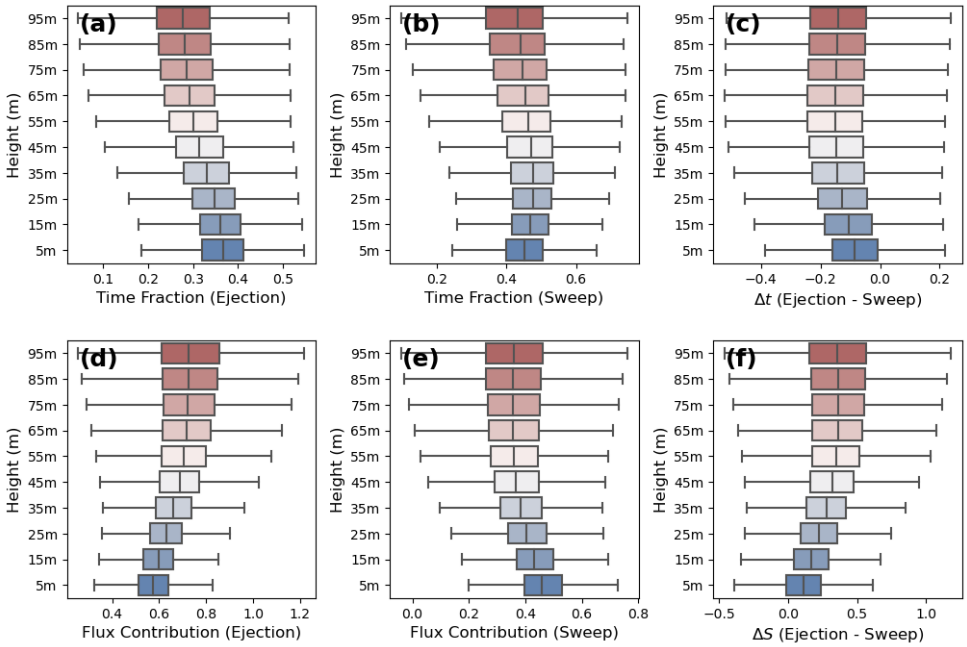

Figure 4.7: Time fraction and flux contribution of ejections and sweeps for case s1200. Similar patterns are observed in other cases (not shown).

As the height in the ASL increases from 5 m to 95 m, the time fraction of ejection (Figure 4.7a) decreases from a mean of 0.37 to 0.30. Meanwhile, the flux contribution of ejection (Figure 4.7d) increases from a mean of 0.58 to 0.70, along with a higher standard deviation. This suggests that the ejections originate from the land surface and increase in intensity while becoming narrower with increasing height. In contrast, the time fraction of sweeps (Figure 4.7b) fluctuates with increasing height, starting at 0.44 at 5 m, peaking at 0.50 at 35 m, and then decreasing to 0.43 at 95 m. The flux contribution of sweeps (Figure 4.7e) decreases with increasing height, indicating that the sweeps originate from the atmosphere and head towards the land surface. These findings are consistent with the work of (Li and Bou-Zeid, 2011) and (Gao *et al.*, 2020).

Another observation from Figure 4.7f is that the contribution difference between ejections and sweeps (ΔS) increases with height, correlating with the decrease in turbulent heat flux in Figure 4.5. Liu *et al.*, (2021) also reported comparable results based on the measurement from the EC tower, that the increased ΔS links to the reduced turbulent heat flux, which explains the increased *FI* with height.

4.4. Discussion

The De18, Z19, and W22 show promising results for predicting *FI*. However, the barriers to directly applying *FI* prediction models in correcting EC measurements must be discussed. When revisiting the *FI* prediction models, it becomes clear that the boundary layer height (z_i) is a critical parameter. However, z_i is not always available from measurements (Mauder *et al.*, 2021). The thermodynamic and aerodynamic properties of the atmosphere can be obtained through various methods, such as Ceilometer, Radiosonde, Doppler Sodar, and profiling radar, as discussed in (Seibert *et al.*, 2000). Moreover, these measurements are relatively expensive to install and maintain. Currently, only 28 stations are reported to have co-located atmospheric boundary layer measurements in the FLUXNET sites (Helbig *et al.*, 2021). In addition, data from these stations may not be continued, and their distribution is generally concentrated in North America and Europe.

The *FI* prediction models under consideration primarily target convective (i.e., unstable) boundary layer conditions. However, correcting EC data during neutral and stable conditions is important to achieve energy balance closure over extended periods. The relative *FI* remains significant during nocturnal periods, even if absolute values may be small (Franssen *et al.*, 2010). Here, the atmospheric stability parameters used in H08, De18, and W22 are inadequate because of the absence of a well-defined w_* under stable conditions (Zhou, Li and Li, 2019).

4.5. Summary and Conclusion

Accurately estimating turbulent heat flux is a persistent challenge in Earth science. Numerous researches suggest that large-scale eddies significantly contribute to the flux imbalance (*FI*). This study aims to investigate *FI* arising from mesoscale transport in convective boundary layer conditions, particularly assessing the performance of selected *FI* prediction models from the literature.

The dataset was generated using a large eddy simulation (ICON-LEM) coupled with a land surface model (TERRA-ML). A checkerboard pattern of wet-dry soil moisture was used to represent the two-dimensional heterogeneity of the land surface across a range of scales from 50 meters to 2.4 kilometers. The model was set up with a spatial coverage of 4.8×4.8 km^2 and a grid resolution of 50 meters. It assumed flat terrain and employed a double periodic boundary setting. Simulations were conducted over 8 hours with a time step of 0.5 seconds. The model was initialized with a constant incoming radiation of 700 $W\ m^{-2}$ at the top of the atmosphere.

Two distinct sub-mesoscale circulations were identified: thermally induced mesoscale circulation (TMC) and turbulent organized structure (TOS). TMC primarily affects atmospheric dynamics on larger heterogeneity scales, reflecting a clear updraft pattern that mirrors the configuration of the arid land surface. As the heterogeneity scale decreases, the relationship between updraft position and soil moisture pattern weakens, and TOS becomes the dominant structure in atmospheric dynamics. Additionally, the domain-averaged *FI* shows a non-linear correlation with the heterogeneity scales, which could be attributed to the presence of two distinct sub-mesoscale circulations. This finding is consistent with previous research suggesting an optimal heterogeneity scale for the formation of secondary circulations.

Four selected *FI* prediction models were evaluated, including H08 (Huang, Lee and Patton, 2008), De18 (De Roo *et al.*, 2018), Z19 (Zhou, Li and Li, 2019), and W22 (Wanner, Calaf and Mauder, 2022). H08 showed a tendency to underestimate the *FI*, which can be attributed to its initial valid vertical height range of 0.3 z_i to 0.5 z_i, while the data used in our analysis are within the above surface layer (ASL), approximately within 0.1 z_i. De18 and Z19 show a similar performance that can roughly capture the *FI*, with a slight underestimation as the measurement height increases. W22 agrees well with our LES data when the heterogeneity scale matches its simulation setting. The performance of the *FI* prediction model provides a potential in correcting EC measurements.

A further observation derived from quadrant analysis is the notable discrepancy between the flux contributions from ejections and sweeps along the height. This difference correlates with a decrease in the turbulent heat flux and an increase in the *FI*. These findings emphasize the importance of considering the EC measurement height and atmospheric model's vertical grid size when studying the vertical variations of turbulent fluxes.

4.6. Appendix

4.6.1. Appendix 1: Scaling Parameters

The scaling parameters used in this work are listed in Table 4.4.

Table 4.4 Scaling Parameters

Scaling parameters	Symbols	Equations
Obukhov length	L	$L = \frac{-u_*^3 \theta_v}{k\, g\, \overline{w'\theta'}}$

von Kármán constant	κ	0.40
Friction velocity	u_*	$u_* = \left\|\frac{\tau}{\rho}\right\|^{\frac{1}{2}} = \left(\overline{u'w'}^2 + \overline{v'w'}^2\right)^{\frac{1}{4}}$
Convective velocity scale	w_*	$w_* = \left[\frac{g\, z_i}{\overline{\theta_v}} (\overline{w'\theta'})_s\right]^{\frac{1}{3}}$
Characteristic temperature scale	θ_*	$\theta_* = \frac{\overline{w'\theta'}_s}{u_*}$
Large-eddy turnover time scale	t_*	$\frac{t_* = z_i}{w_*}$
Thermal heterogeneity parameter	H_{par}	$H_{par} = \frac{g\, l_h}{U^2} \frac{\Delta T}{\overline{T}}$, l_h is the heterogeneity scale
Integral length scale of vertical velocity	l_w	$l_w = \int_0^\infty R(r)dr$

4.6.2. Appendix 2: Equivalent Homogeneous Simulation

An equivalent homogeneous simulation was performed in this study but with a different domain-averaged soil moisture value. A sensitivity analysis of soil moisture to the domain-averaged sensible heat flux, as shown in Figure 4.8, indicates that a value of 0.325 $cm^3 cm^{-3}$ is comparable to the heterogeneous case. The land surface model used in this study (TERRA-ML) utilized a simple soil moisture loss function to calculate evapotranspiration (i.e., latent heat flux), as shown in Figure 4.9. In this model, evapotranspiration remains constant when soil moisture is low, increases constantly within the transitional zone, and becomes constant again when the soil is sufficiently wet.

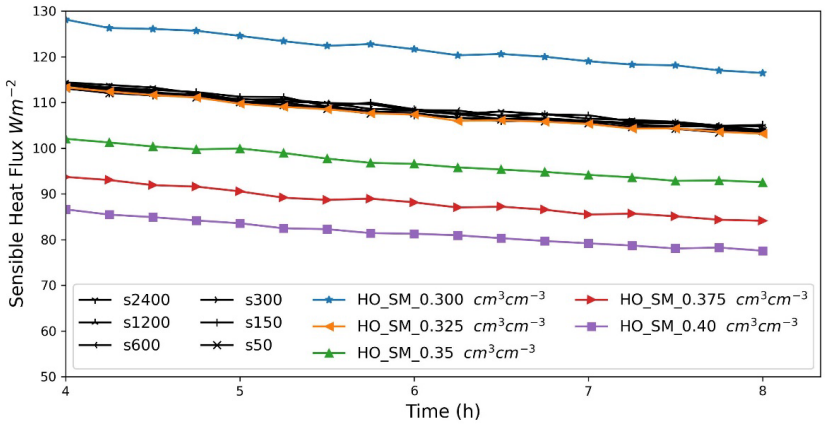

Figure 4.8: Time-series of sensible heat flux at the land surface for different simulations. Simulation with homogeneous soil moisture (HO_SM) of 0.325 $\boldsymbol{cm^3cm^{-3}}$ is suitable to represent as a comparable homogeneous case in this study.

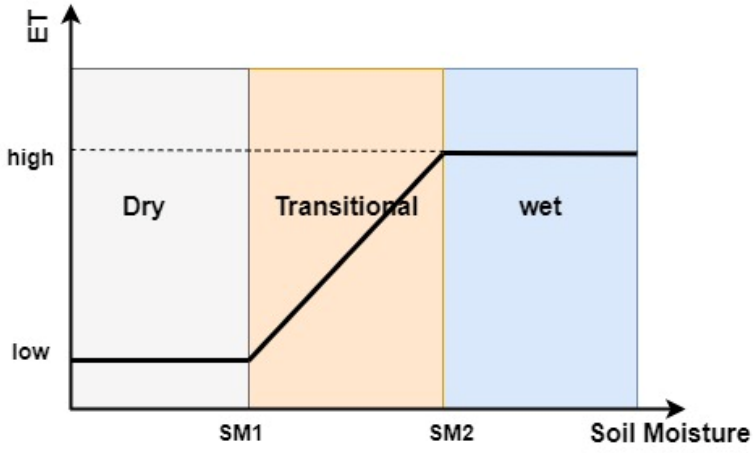

Figure 4.9: Sketch of the evapotranspiration calculated in TERRA-ML.

4.6.3. Appendix 3: Statistical Homogeneous

Figure 4.10 indicates that the differences in the kinetic energy spectrum between different simulations are largest at the lowest wavenumber. Specifically, simulations s2400 and s1200 show significant differences compared to other cases. In the case of s600, these differences begin to decrease. For the s300 simulation, differences are still observable, particularly at

wavenumbers 2 and 3. However, for simulations s150 and s50, the differences from the homogeneous case are negligible, indicating that a statistically homogeneous state is reached.

Furthermore, a point-to-point Pearson correlation coefficient is calculated between the land surface heat flux and the turbulent heat flux in the atmosphere at 45 m for the average of the last hour simulation. This is illustrated in Figure 4.11. The Pearson correlation coefficient demonstrates a decline in conjunction with a reduction in heterogeneity scale, exhibiting values of 0.74 for s2400, 0.62 for s1200, and 0.47 for s600. The coefficient for simulation s300 is 0.27, which is higher than those for simulations s150 and s50, where values are less than 0.1 and are similar to those observed in the homogeneous case.

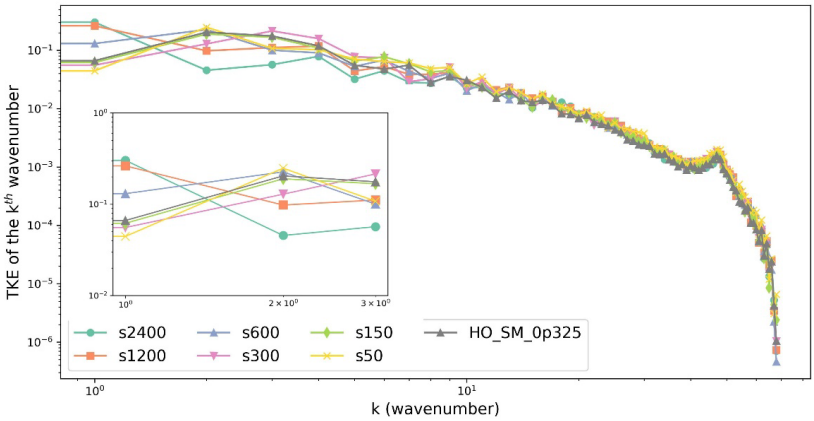

Figure 4.10: Kinetic energy spectrum for the last hour simulation at a height of 45 meters. The subfigure provides a zoomed-in view at the smallest wavenumber.

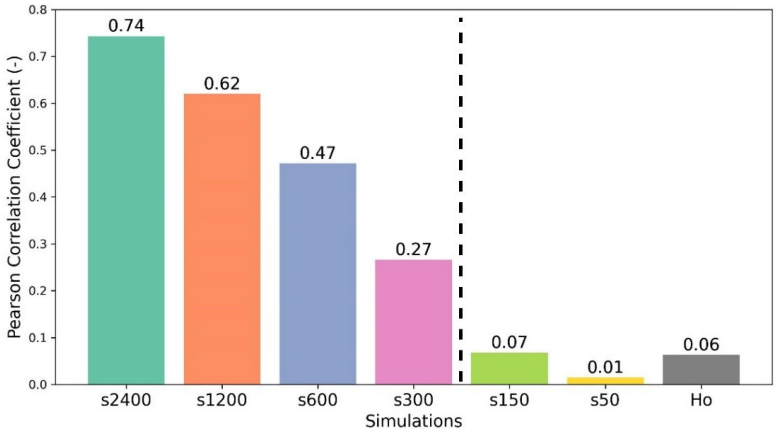

Figure 4.11: Point-to-point Pearson correlation coefficient between the land surface heat flux and the turbulent heat flux in the atmosphere at 45 m, averaged over the last hour of simulation.

Chapter 5

5. An Alternative Way to Parameterizing the Nonlocal Scale Sensible Heat Flux Using the Flux Imbalance and K-theory Approach

5.1. Introduction

The accurate representation of heat flux is important in Earth System Models (ESMs), yet presents a significant challenge (Bauer, Thorpe and Brunet, 2015). Heat flux involves various processes, including surface energy and water allocation (Mauder *et al.*, 2018; Lin, Li and Zhao, 2022), planetary boundary layer (PBL) development (Sullivan *et al.*, 1998), entrainment penetration (VanZanten, Duynkerke and Cuijpers, 1999), as well as cloud formation and deep convection (Stevens, 2007; Hohenegger *et al.*, 2009; Sedlar *et al.*, 2022). The interactions between the atmosphere and the land surfaces occur across a wide range of spatial scales, from hundreds of kilometers to millimeters, and across various temporal scales, from seconds and minutes to days, seasons, and years (Stull, 1988; Klein, 2008). Given the impracticality of resolving all scales directly in atmospheric models, the unresolved physical processes are often described using subgrid-scale (SGS) parameterizations (Ament and Simmer, 2006; Edwards *et al.*, 2020; Kuell and Bott, 2022). In numerical weather prediction (NWP) models, grid sizes are typically several kilometers and rely heavily on SGS parameterizations to account for unresolved processes, such as the heat flux (Niu *et al.*, 2011; Bauer, Thorpe and Brunet, 2015; Zängl *et al.*, 2015). Reducing grid sizes to sub-kilometer scales, and thus entering the gray zone (or terra incognita), poses significant challenges to these parameterizations, as turbulence is only partially resolved (Wyngaard, 2004).

In ESMs, the heat flux is often described in the gradient diffusion approach, also known as K-theory. This assumes that the flux is proportional to the gradient of the scalar of interest, as described in Eq. 5.1 for the sensible heat flux,

$$H = -\rho C_p K_h \frac{\partial \overline{\theta}}{\partial z}, \tag{5.1}$$

where H (Wm^{-2}) is the sensible heat flux, ρ ($kg\ m^{-3}$) is the air density, C_p ($J\ kg^{-1}K^{-1}$) is the specific heat capacity of air, K_h (m^2s^{-1}) is the eddy diffusivity, θ (K) is the potential temperature and z (m) is the measurement height.

The upward heat flux typically penetrates to around 80% of the PBL height (i.e. 0.8 z_i), while the potential temperature gradient becomes negative at approximately 40% of the PBL height

(i.e. 0.4 z_i), indicating a locally counter-gradient relationship associated with thermals and plumes (Pleim, 2007; B. Zhou *et al.*, 2018). Thus, the flux profile in the boundary layer becomes the result of a roughly linear superposition of bottom-up (local) and top-down (non-local) contributions (Wyngaard and Brost, 1984; Huang, Lee and Patton, 2008; Liu *et al.*, 2024). To represent the nonlocal transport contribution from top-down fluxes, it is often necessary to employ an additional counter-gradient term (γ_θ), as described in Eq 5.2 (Deardorff 1966; Deardorff 1972; Holtslag and Moeng 1991).

$$H = -\rho C_p K_h \left(\frac{\partial \bar{\theta}}{\partial z} - \gamma_\theta\right). \tag{5.2}$$

A variety of effects have been proposed to represent the counter-gradient term. For example, the counter-gradient term in the PBL scheme proposed by Holtslag and Moeng (1991) is related to the heat flux at the land surface ($\overline{w'\theta'}_s$) and is inversely proportional to both the boundary layer height (z_i) and the convective velocity scale ($w_* = (\frac{g}{\theta_v} zi\ (\overline{w'\theta'})_s)^{1/3}$, with $g = 9.81\ ms^{-2}$ as the gravitational acceleration).

An alternative method to account for the non-local mixing effect involves separating the updraft contribution from the surrounding environment using a conditional sampling approach. For instance, the mass flux model identifies updrafts as $w(x,y,z) > w_p(z)$, where p represents the top percentage of vertical wind speed, typically ranging from 1% to 10% (Siebesma, Soares and Teixeira, 2007; Li *et al.*, 2018; Tan *et al.*, 2018). The eddy diffusivity and mass flux (EDMF) schemes, given

$$H = \rho C_p \left[-K_h \frac{\partial \bar{\theta}}{\partial z} + M(\theta_u - \langle\theta\rangle)\right], \tag{5.3}$$

where θ_u represents the potential temperature in the updraft zones, and <θ> is the horizontal averaged value. The mass flux model offers a more physical perspective on separating the local and nonlocal part of the heat flux compared to the counter-gradient term aforementioned and has been implemented in several operational ESMs, such as the NASA GEOS (Suselj *et al.*, 2021), among others.

Describing heterogeneous land surfaces in ESMs remains challenging, particularly in terms of their impact on atmospheric structures and characteristics (Giorgi and Avissar, 1997; Bou-Zeid *et al.*, 2020). Secondary circulations have been consistently observed over heterogeneous land surfaces in both measurements (Eder, De Roo, *et al.*, 2015) and LES (Avissar and Schmidt, 1998; Raasch and Harbusch, 2001) and are influenced by the heterogeneity structure (Bou-

Zeid, Meneveau and Parlange, 2004; Bou-Zeid, Parlange and Meneveau, 2007; Han, Brdar and Kollet, 2019), scales (Patton, Sullivan and Moeng, 2005; van Heerwaarden, Mellado and De Lozar, 2014), gradients (Huang and Margulis, 2013), terrains (Rihani, Chow and R. M. Maxwell, 2015; Weinkaemmerer *et al.*, 2023) and background winds (Avissar and Schmidt, 1998; Kang and Lenschow, 2014; Eder, De Roo, *et al.*, 2015; Zhang, Poll and Kollet, 2023). Land surface models (LSMs) often use a tile-based approach to represent heterogeneity, where the flux in each tile is calculated independently, and the pixel-scale value is determined as the tile area weighted arithmetic mean, without accounting for the interaction between tiles (Avissar *et al.*, 1989; Lawrence *et al.*, 2019). Machulskaya and Mironov (2018) propose that the inter-tile (co-)variance of scalar quantities at the land surface should be considered for the lower boundary. The incorporation of this term into ESMs (e.g. E3SMv1 single column mode) results in an increase in the variance of potential temperature and humidity in the atmospheric surface layer, accompanied by a slight increase in cloud cover (Huang *et al.*, 2022). Similar outcomes were documented by Fowler et al. (2024) in the Community Earth System Model (CESM2). Nevertheless, the atmospheric response to land surface heterogeneity is less pronounced compared to a referenced LES case, primarily due to the absence of explicit representation of mesoscale secondary circulations (Fowler *et al.*, 2024).

Recent research shows that the nonlocal effects (e.g. secondary circulation) on the heat flux estimation can be quantified through the similarity functions, that is to say, the flux imbalance (*FI*, ratio of the nonlocal heat flux to the total reference heat flux) could be quantified through semi-empirical functions with scaling parameters (Huang, Lee and Patton, 2008; De Roo and Mauder, 2018a; Zhou, Li and Li, 2019; Wanner, Calaf and Mauder, 2022). These models exhibit a robust ability to perform under various conditions, both in the case of measurements (Mauder *et al.*, 2021) and numerical simulations (Zhou, Sühring and Li, 2023). This study aims to address the research question: can the representation of heat fluxes in ESMs be improved by incorporating *FI* prediction models to account for the nonlocal effects? To answer this question, this study aims to propose an alternative approach that represents nonlocal processes using *FI* prediction models while utilizing the conventional K-theory approach for the local processes. Section 5.2 describes the flux imbalance and K-theory (FLIMK) scheme and introduces the numerical model and simulation setups. Section 5.3 presents the results of the FLIMK scheme in both LES and numerical weather prediction model (NWP). Finally, a summary and conclusion are offered in Section 5.4.

5.2. Methods

5.2.1. Flux Imbalance and K-theory Approach

The sensible heat flux in the atmospheric surface layer (ASL, roughly 10% of PBL height close to the surface) consists of the local and nonlocal parts, as shown in Figure 5.1. The local scale turbulent heat flux is typically described as the covariance of two scalar measurement fluctuations, especially those obtained using the eddy-covariance system (e.g. $\overline{w'\theta'}$). In ESMs, however, the local scale flux is presented using K-theory as $-K_h \frac{\partial \bar{\theta}}{\partial z}$. The nonlocal processes include the total vertical advection flux ($\langle \bar{w} \rangle \langle \bar{\theta} \rangle$), and the dispersive flux $\langle \delta \bar{w} \delta \bar{\theta} \rangle$). In this paper, the definition of the flux imbalance follows Zhou *et al.,* (2019), as the ratio of the nonlocal part to the total reference sensible heat flux at the land surface, given

$$FI = \frac{\langle \delta \bar{w} \delta \bar{\theta} \rangle + \langle \bar{w} \rangle \langle \bar{\theta} \rangle}{\langle \bar{H}_{ref} \rangle} = 1 - \frac{\langle \overline{w'\theta'} \rangle}{\langle \bar{H}_{ref} \rangle}. \tag{5.4}$$

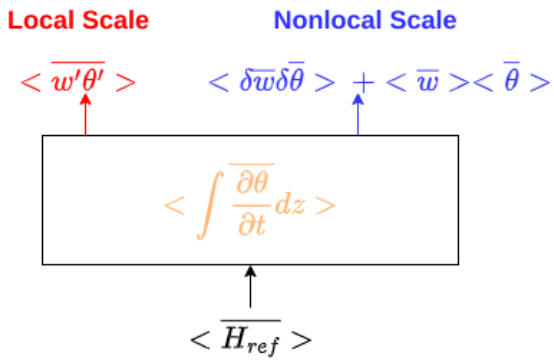

Figure 5.1: Graphical representation of the sensible heat flux. The local scale shows in red, and the nonlocal part shows in blue. Only the heat flux in the vertical direction is considered.

The *FI* has received attention both in field measurements (Wilson *et al.*, 2002; Barr *et al.*, 2006; Franssen *et al.*, 2010; Foken *et al.*, 2011; Stoy *et al.*, 2013; Paleri *et al.*, 2022) and in the large-eddy simulations (Huang, Lee and Patton, 2008; De Roo *et al.*, 2018; Zhou, Li and Li, 2019; Wanner, Calaf and Mauder, 2022; Zhou, Sühring and Li, 2023), leading to several semi-empirical functions being proposed to quantify the *FI*. In this study, the flux imbalance prediction model from De Roo *et al.,* (2018) is selected, hereafter FLIMK_De18, shown in Eq. 5.5, where u_* (ms^{-1}) is the friction velocity, w_* (ms^{-1}) is the vertical velocity scale, z (m) is

the measurement height, and z_i (m) is the boundary layer height. The *FI* may also be calculated based on the definition in Eq. 5.4, which is referred to as FLIMK_LES.

$$FI = \left[0.197 \exp\left(-17.0 \frac{u_*}{w_*}\right) + 0.156\right]\left[0.21 + 10.69 \frac{z}{zi}\right]. \tag{5.5}$$

Based on the *FI* prediction model, a novel approach, the FLIMK scheme, is proposed to account for the nonlocal effect in the surface layer, as shown in Figure 5.2. Specifically, the sensible heat flux at the lowest atmospheric layer will be modified using the *FI* prediction model, as specified in Eq. 5.6. The derivation of Eq. 5.6 is presented in Appendix 4.

$$\overline{H}_{ref} = \frac{-K_h \partial \overline{\theta} / \partial z}{1 - FI}. \tag{5.6}$$

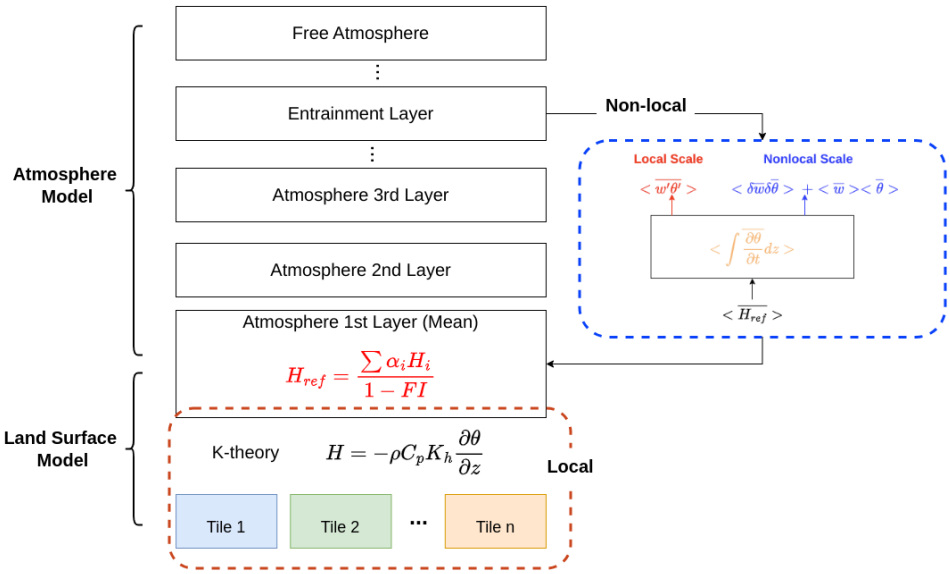

Figure 5.2: Scheme of the FLIMK, the nonlocal effect is described by the *FI* prediction models, where the lowest atmosphere layer is modified based on the *FI*.

5.2.2. Model and Simulation Setup

In this study, the FLIMK scheme is tested in both the idealized LES with prescribed sensible heat flux at the surface, and in a numerical weather prediction (NWP) setup using real test cases from the Atmospheric Radiation Measurement (ARM) campaign (Brown *et al.*, 2002; Ďurán *et al.*, 2021). For that, the Icosahedral Nonhydrostatic Weather and Climate Model (ICON) was selected, as ICON is the new generation of fully compressible atmospheric models, covering

all scales including the climate model, Numerical Weather Prediction (NWP), and Large-Eddy Simulation (LES) (Dipankar *et al.*, 2015b; Zängl *et al.*, 2015; Van Pham *et al.*, 2020).

A 3D sub-grid Smagorinsky scheme with Lilly's stability correction is implemented in ICON to calculate the eddy diffusivity, see Eq 5.7 (Lilly, 1962; Smagorinsky, 1963). With C_s as the Smagorinsky constant of 0.23, $|S| = \sqrt{\frac{1}{2}\left(\frac{\partial u_i}{\partial x_j} + \frac{\partial u_j}{\partial x_i}\right)^2}$ is the strain rate tensor, $\Delta = (\Delta x \Delta y \Delta z)^{1/3}$ is the filter width, and Pr_t as the Prandtl number. Details of the physical parameterization of ICON is referred to the work of (Dipankar *et al.*, 2015b; Zängl *et al.*, 2015) and reference therein.

$$K_h = (C_s \Delta)^2 |S| C_B \frac{1}{Pr_t}, \tag{5.7}$$

In the LES, the land surface heterogeneity was configured with three stripes (Figure 5.3), with the middle stripe representing a sensible heat flux of 0.2 $K\,ms^{-1}$, and the side stripes representing 0.1 $K\,ms^{-1}$. The domain, with double-periodic boundary conditions, covers an area of 19.2 × 19.2 km² and has a spatial resolution of 50 × 50 m². It extends vertically to 4.2 km with a vertical grid size of 10 m, with a sponge layer set at the top 500 m of the model. The simulation lasted for 8 hours, and data from the final hour were used for analysis. It is worth noting that the FLIMK scheme is not run online; instead, it is evaluated by calculating a *priori* based on the LES output.

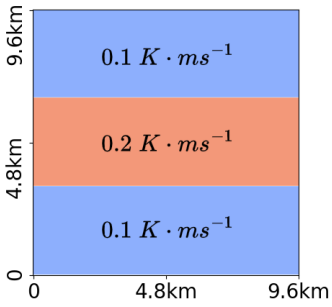

Figure 5.3: Prescribed sensible heat flux in the LES. The middle strip has a larger sensible heat flux of 0.2 $\boldsymbol{K\,ms^{-1}}$ and the side stripes has a smaller value of 0.1 $\boldsymbol{K\,ms^{-1}}$.

In the NWP, forcing data were obtained from measurements conducted over the Atmospheric Radiation Measurement (ARM) program site in Oklahoma on 21 June 1997. Further details of the program can be found in Brown *et al.*, (2002) and Lenderink *et al.*, (2004), with the data available in Ďurán *et al.*, (2021). Additionally, the performance of ICON-SCM has been

evaluated using a well-designed LES model (MicroHH), which yielded satisfactory results. The SCM configuration followed that of Ďurán *et al.*, (2021), with an improved vertical grid size of 10m and the incorporation of the FLIMK scheme in an online simulation approach.

5.3. Results and Discussions

Section 5.3.1 presents the results of the LES, including cross-sections of the potential temperature anomaly, vertical winds, and horizontal winds. These demonstrate the formation of a well-defined secondary circulation structure. This section also highlights the *FI* observed when only local-scale effects (K-theory) are considered and the improvement achieved by the FLIMK scheme. Section 5.3.2 is devoted to the results of the NWP in the single-column mode, with particular emphasis on the enhanced representation of sensible heat flux in the lowest atmospheric layer and the vertical profile of potential temperature. Section 5.3.3 discusses the potential of using other *FI* prediction models and the numerical model convergence.

5.3.1. Large Eddy Simulation

Figure 5.4a shows the horizontal cross-section of the potential temperature anomaly at a height of 45 m. Figure 5.4d displays the vertical cross-sectional of the potential temperature anomaly, averaged along the *y*-direction. In the region with a higher sensible heat flux (see Figure 5.3), a greater potential temperature anomaly is observed in the lower part of the boundary layer, corresponding to a lower potential temperature anomaly at the top of the boundary layer. Figure 5.4e depicts a pattern of the vertical velocity characterized by a narrow region of strong updraft, compensated by a broader area of weak downdraft. Similar patterns have been well presented in previous works (Salesky, Chamecki and Bou-Zeid, 2017; B. Zhou *et al.*, 2018). Figure 5.4 c and Figure 5.4f illustrate that horizontal winds (U) converge (diverge) at the lower (upper) portion of the boundary layer, indicating a well-defined secondary circulation structure. Additionally, the horizontal wind induced by the secondary circulation can reach speeds exceeding 2 ms^{-1}, consistent with findings reported in previous LES studies (Lee, Zhang and Klein, 2019; Zhang, Poll and Kollet, 2023).

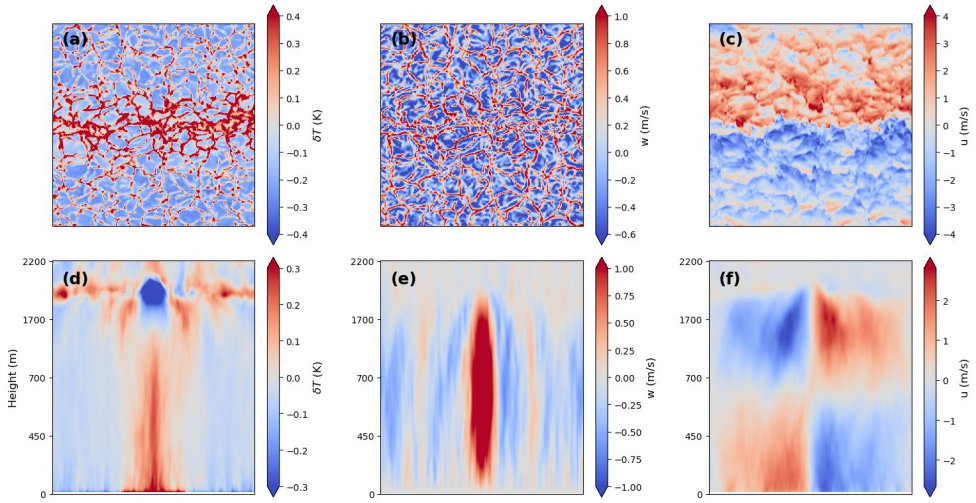

Figure 5.4: Horizontal cross-sections of potential temperature anomaly at 45 m (a), vertical wind speed at 50 m (b), and horizontal wind speed at 45 m (c). Vertical cross-sections of potential temperature anomaly (d), vertical wind speed (e), and horizontal wind speed (f).

A series of sub-regions of varying sizes, ranging from the grid scale (50 m) to larger scales of up to 9.6 km, are selected to investigate the effect of scale on the *FI*. Each sub-region is selected at a random location with 50 samples. The sensible heat flux at a height of 45 m is calculated using both the K-theory and the FLIMK and is then normalized to the prescribed sensible heat flux at the land surface, as shown in the boxplot in Figure 5.5. The underestimation of K-theory is consistent across all scales, with values ranging from approximately 12% to 16% (normalized heat flux of 0.84 to 0.88) for the majority of sub-regions and 15% for the entire area (i.e. 0.85). The mean variance of the normalized heat flux decreases with increasing size.

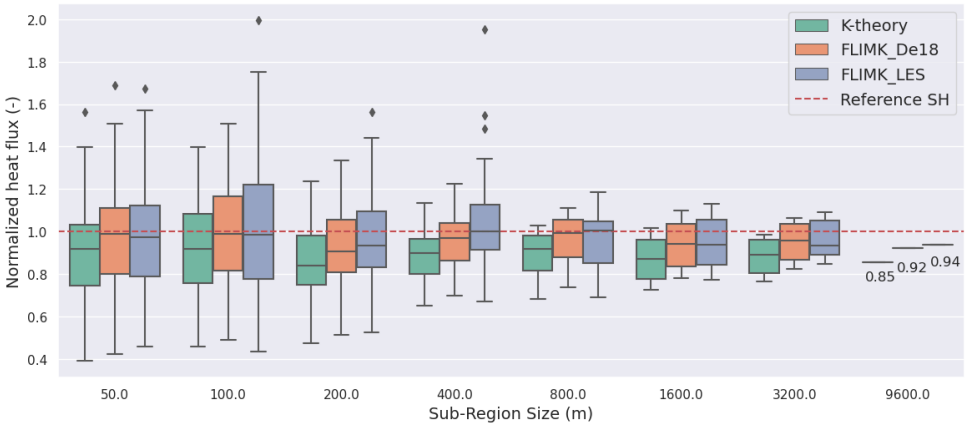

Figure 5.5: Normalized sensible heat flux at 45 m. The value of unit one (red dashed line) indicates no flux imbalance, while any value smaller than unit one represents an underestimation.

The flux imbalance prediction model can be derived based on the definition of Eq 5.4 as FLIMK_LES or based on Eq 5.5 as FLIMK_De18. The underestimation of the sensible heat flux reduced from 15% to 8% (6%) for FLIMK_De18 (FLIMK_LES). It is crucial to highlight that the FLIMK does not lead to perfect closure of the fluxes. Firstly, the turbulent heat flux ($\overline{w'\theta'}$) is influenced by the sampling window size, whereby a larger window size leads to a larger heat flux value. Secondly, the eddy diffusivity (K_h) is a variable that is dependent on height. A different value may be obtained despite the potential temperature gradients being subject to change. In order to circumvent the potential consequences of the SGS parameterization near the land surface, a height of 45 meters has been selected.

5.3.2. Numerical Weather Prediction

The temporal evolution of the sensible heat flux calculated from the K-theory and the FLIMK scheme using the ARM test case is shown in Figure 5.6a. The K-theory and the FLIMK scheme slightly overestimate the sensible heat flux before 4h because the convective boundary layer is not well-formed due to the weak surface sensible heat flux. In contrast, K-theory demonstrated a tendency to underestimate the sensible heat flux after 4 hours, with this underestimation gradually increasing with time to reach a maximum value of 0.018 $K\,ms^{-1}$ (i.e. 16% underestimation) at about 7h. It should be noted that there is no guarantee that the maximum underestimation in absolute value and the maximum *FI* values (i.e. a ratio) will coincide since both are subject to change over time.

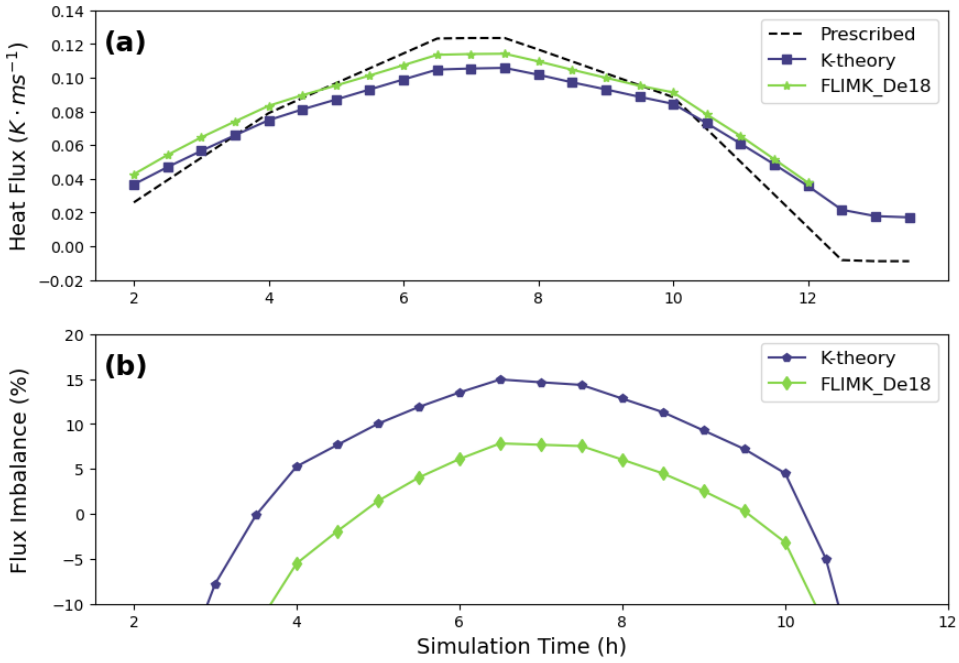

Figure 5.6: Temporal evolution of the sensible heat flux (a) and *FI* (b).

The K-theory and FLIMK_De18 overestimate the heat flux after 10 hours, as shown in Figure 5.6, with a negative value of *FI,* coinciding with a significant decrease in the prescribed sensible heat flux. One potential explanation is that the *FI* prediction model of De18 is proposed based on the convective boundary layer (CBL) conditions. In cases where the heat flux at the land surface is not sufficiently strong, the *FI* prediction model may be rendered inapplicable. Another possible reason is that the convective velocity scale (w_*) used in the De18 is not well defined during the stable or nocturnal periods. It should be noted that there are other *FI* prediction models, which will be discussed in the following section.

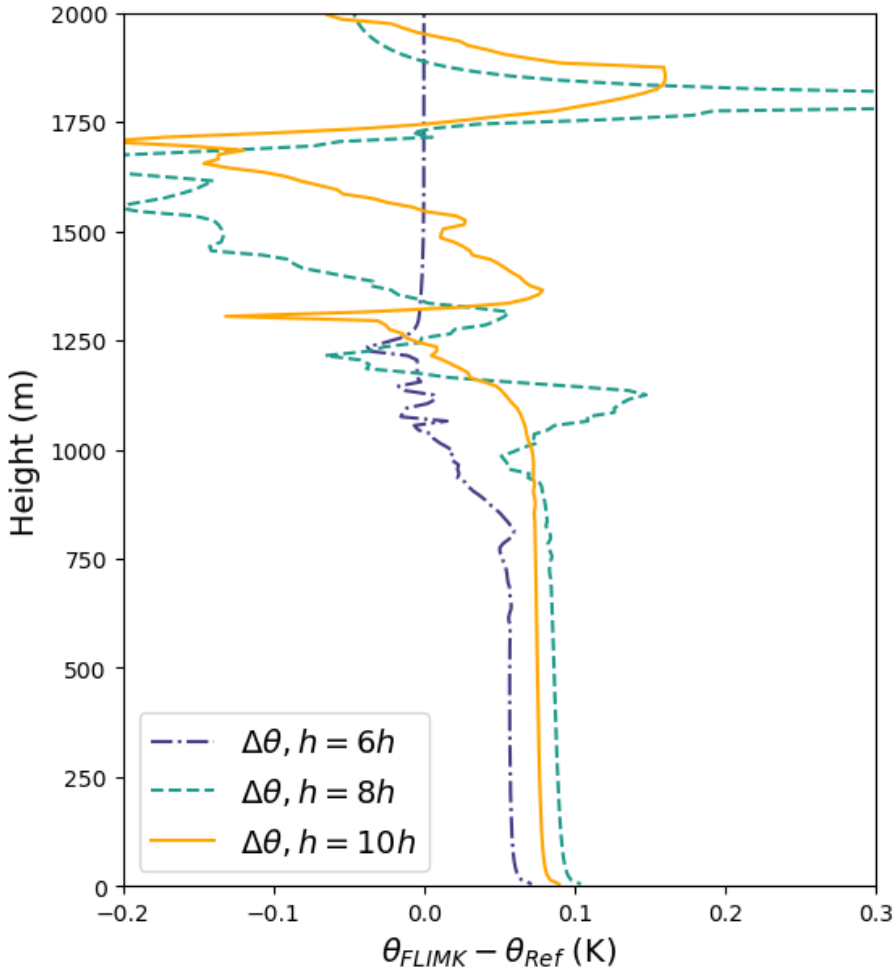

Figure 5.7: Impact of the FLIMK scheme on the potential temperature profile.

The discrepancy between the potential temperature calculated with and without the FLIMK schemes is shown in Figure 5.7. The potential temperature difference increased from 0.07 K to 0.1 K from 6 h to 8 h in the lower part of the PBL, then decreased again from 0.1 K to 0.08 K. This indicates that the model is convergent, as the increase in the sensible heat flux results in an increase in the boundary layer height, leading to a decrease in the *FI* based on De18 (i.e. negative feedback).

At 6h, the impact of the FLIMK scheme on the heat flux at the entrainment zone is insignificant, and the discrepancy in potential temperature ($\theta_{FLIMK} - \theta_{Ref}$ in Figure **5.7**) between the K-

theory and the FLIMK scheme is nearly inconsequential at the top of the PBL. In contrast, at 8 h and 10 h, there is a clear negative $\theta_{FLIMK} - \theta_{Ref}$ at the top of PBL.

5.3.3. Discussions

5.3.3.1. The Flux Imbalance Prediction Model

Numerous effects have been incorporated into PBL schemes to account for nonlocal processes. For instance, more than ten PBL schemes are available in the WRF models for research. However, the current PBL schemes lack an explicit representation of secondary circulations, which is a significant contributing factor to the comparatively weak response of the atmosphere to land surface heterogeneity in PBL schemes compared to LES (Fowler *et al.*, 2024). For example, Waterman *et al.,* (2024) proposed a two-column model that parameterized the subgrid surface heterogeneity-induced circulations with the difference in potential temperature between the two patches and the profiles of the potential temperature and air density. The model can qualitatively reproduce the patterns from LES. Nevertheless, further enhancements are required in the parameter-tuning process (Waterman *et al.*, 2024).

Rather than attempting to reproduce the mesoscale circulations in the sub-grid parameterization, this work aims to incorporate the effects of those circulations on calculating the heat flux. Thus, an alternative approach is proposed to enhance the sensible heat flux at the lowest atmospheric level. This approach is inspired by the observation that *FI* prediction models can qualitatively describe the effects of nonlocal processes on heat flux calculation. It is crucial to acknowledge that this study is concerned with representing sensible heat flux rather than developing a novel PBL scheme. Secondly, it is pertinent to highlight that alternative *FI* prediction models have been proposed in the literature. Table 5.1 lists a few examples for illustrative purposes, and the interested readers are directed to Zhang *et al.,* (2024) for an evaluation work.

Table 5.1: Available Flux Imbalance Prediction Models in the Literature.

Notation	Flux Imbalance Prediction Model	Reference
H08	$\langle I \rangle = \left[\exp\left(4.2 - 16\,\frac{u_*}{w_*}\right) + 2.1\right]\left[1.1 - 8.0\left(\frac{z}{z_i} - 0.38\right)^2\right]^{0.5}$	(Huang et al. 2008)
De18	$\langle I \rangle = \left[0197\exp\left(-17.0\,\frac{u_*}{w_*}\right) + 0.156\right]\left[0.21 + 10.69\,\frac{z}{z_i}\right]$	(De Roo et al. 2018)
Z19	$\langle I \rangle = 1 - \left[-1.46\frac{z}{z_i} + 1.0\right]\left[-0.05\frac{z_i}{L}\frac{l_w}{U\,T} + 0.95\right]$	(Zhou et al. 2019)

W22	$\langle I \rangle = \left[a \exp\left(b \frac{u_*}{w_*}\right) + c\right]\left[20.05 \frac{z}{z_i} + 0.157\right]\left[H_{par}\right]$	(Wanner et al. 2022)

The initial flux imbalance prediction model is that of Huang *et al.,* (2008), which is suitable for calculating *FI* at heights between 0.3 z_i to 0.5 z_i. The work of De Roo *et al.,* (2018) and Zhou *et al.,* (2019) is more appropriate for the lower range, below 0.1 z_i. Furthermore, *FI* prediction models for latent heat flux are documented in the literature, including the one by De Roo *et al.,* (2018). However, this study focuses only on the sensible heat flux.

The subsequent phase of research will focus on the implementation of the FLIMK scheme, which will entail modifications to both sensible and latent heat fluxes. However, the question of whether to maintain the Bowen ratio in a consistent state and the issue of harmonizing *FI* prediction models remain open. A consistent body of evidence has reported discrepancies between heat and humidity (Lamaud and Irvine, 2006; Huang and Margulis, 2009).

5.3.3.2. Numerical Model Convergence

Modifying the sensible heat flux in the surface layer raises the question of whether the energy input to the model might be excessively increased, potentially leading to model instability or failure. The FLIMK scheme is similar to the conventional PBL scheme of Holtslag and Moeng (1991), but it uses the concept of the *FI* to incorporate nonlocal processes. The FLIMK scheme can be expressed as $H = -\rho C_p \left(\frac{\partial \bar{\theta}}{\partial z} + \frac{FI}{1-FI}\frac{\partial \bar{\theta}}{\partial z}\right)$ based on Eq 5.6, that the $\frac{FI}{1-FI}\frac{\partial \bar{\theta}}{\partial z}$ serves as the counter-gradient term. The revised sensible heat flux in the lower atmosphere through the FLIMK scheme gives rise to a modification in the potential temperature that propagates to a higher layer, as illustrated in Figure 5.7. However, an increase in boundary layer height has reduced *FI*, which has led to negative feedback. This is further supported by the fluctuations in the difference between the boundary layer height between the K-theory and the FLIMK scheme, as demonstrated in Figure 5.8.

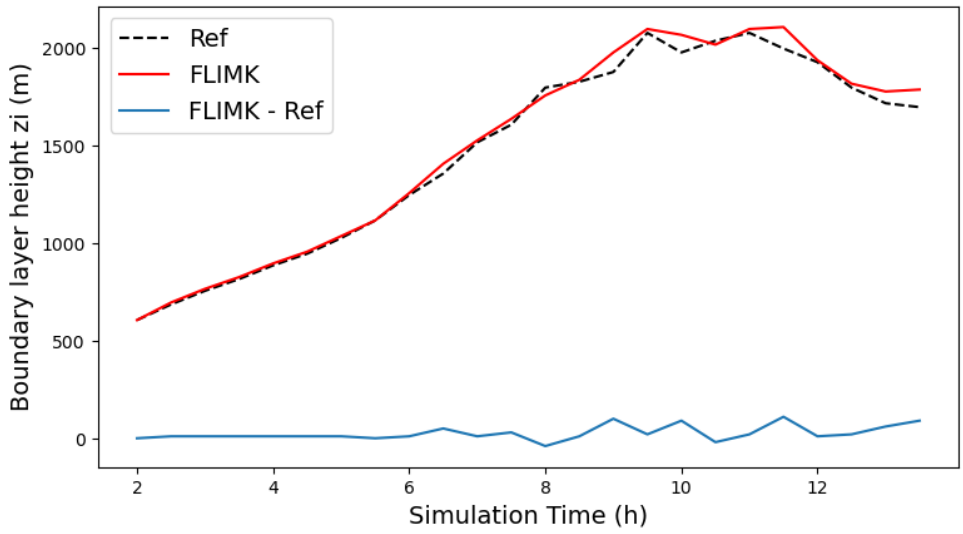

Figure 5.8: Boundary layer height as a function of simulation time.

5.4. Summary and Conclusions

Parameterizing the effects of secondary circulations in Earth System Models (ESMs) is important yet challenging. Building on the demonstrated robustness of the flux imbalance (*FI*) prediction model in quantifying nonlocal processes in heat flux calculations, this study proposes a novel approach that employs the *FI* prediction model to explicitly describe the nonlocal processes induced by secondary circulations. This alternative approach, the Flux Imbalance and K-theory (FLIMK), combines the gradient diffusion approach (K-theory) for local processes and the *FI* prediction models for the nonlocal processes.

Two different models were employed to evaluate FLIMK separately: a large eddy simulation (LES) using prescribed strip sensible heat fluxes, and a numerical weather prediction (NWP) model using field measurements from the Atmospheric Radiation Measurement campaign. The results demonstrate that FLIMK reduces the *FI* from approximately 15% (16%) to 6% (6.7%) for LES (NWP). The FLIMK scheme demonstrates a high level of performance across a range of scales, from 50 m to 9.6 km. Furthermore, the FLIMK scheme is numerically convergent. The boundary layer height rises as the sensible heat flux increases, reducing the *FI* through a negative feedback mechanism.

The proposed FLIMK scheme is not intended to replace existing Planetary Boundary Layer (PBL) schemes but to enhance the representation of surface layer heat fluxes. Due to its simple formulation, which requires only atmospheric stability (u_*/w_*) and relative height (z/z_i), the FLIMK scheme can be easily integrated with existing PBL schemes. This offers a potential pathway for model parameterization improvement. Our next step in future work will involve incorporating latent heat flux into the FLIMK scheme.

5.5. Appendix 4

This section presents the mathematical derivation of the flux imbalance and the K-theory approach (FLIMK). The definition of the flux imbalance (*FI*), as proposed by Zhou et al. (2019), is the ratio of the nonlocal processes (i.e., advection, A, and dispersive flux D) to the reference heat flux at the land surface ($\overline{H}_{ref}$), as illustrated in Eq. A-5.1. In the context of the assumption of a constant flux for the atmospheric surface layer, the reference heat flux can be defined as the sum of the local process ($\overline{w'\theta'}, or\ -K_h\,\partial\bar{\theta}/\partial z$) and the nonlocal processes ($A + D$), see Eq. A-5.2a and A-5.2b. Consequently, the ratio of the local processes to the reference heat flux can be derived in A-5.3, and A-5.4 can be obtained by moving the $\overline{H}_{ref}$ to the left-hand side of the equation.

$$FI = \frac{A+D}{\overline{H}_{ref}}, \tag{A-5.1}$$

$$\overline{H}_{ref} = \underbrace{\overline{w'\theta'}}_{local} + \underbrace{A + D}_{nonlocal}, \tag{A-5.2a}$$

$$\overline{H}_{ref} = \underbrace{-K_h\partial\bar{\theta}/\partial z}_{local} + \underbrace{A + D}_{nonlocal}, \tag{A-5.2b}$$

$$1 - FI = \frac{-K_h\partial\bar{\theta}/\partial z}{\overline{H}_{ref}}, \tag{A-5.3}$$

$$\overline{H}_{ref} = \frac{-K_h\partial\bar{\theta}/\partial z}{1 - FI}. \tag{A-5.4}$$

Chapter 6

6. Conclusions and Outlooks

6.1. Summary

The growing reliance on Earth System Models (ESMs) for understanding and forecasting natural phenomena underscores the critical need for precise and accurate representations of the physical processes within these models. A significant challenge in atmospheric science is quantifying the mesoscale secondary circulations that often form over heterogeneous land surfaces. Secondary circulations have a profound impact on land surface-atmosphere interactions, as well as on the structure and characteristics of the atmosphere. An increasing body of research suggests that secondary circulations play a significant role in underestimating flux measurements, exemplified by the eddy covariance (EC) measurement and large eddy simulations (LES). The formation of secondary circulations has been studied under various conditions, and the impact of secondary circulations on flux estimation led to the development of flux imbalance (*FI*) prediction models. Nevertheless, the formation of the secondary circulation under ambient wind conditions requires further investigation, and the existing *FI* prediction models necessitate a comprehensive evaluation over more complex heterogeneous land surfaces. This PhD work addresses these gaps by investigating the influence of ambient winds on the formation and characteristics of secondary circulations, evaluating *FI* prediction models over two-dimensional heterogeneous land surfaces, and proposing a scheme to incorporate secondary circulation effects into ESMs.

In Chapter 3, a series of LES were conducted over a flat river corridor setup, represented by a continuous heterogeneous soil moisture distribution, with saturation occurring in the middle of the region and progressively drier conditions towards the edges. Constant ambient winds with varying speeds from 0.5 ms^{-1} to 16 ms^{-1} were imposed across the domain, with wind directions ranging from perpendicular (cross-river wind) to parallel (parallel-river wind) and intermediate orientations (mixed wind). The findings indicate that secondary circulation is influenced by ambient wind speed and its relative orientation to the heterogeneity. Secondary circulation is destroyed when the cross-river wind speed exceeds the phase wind speed, which is approximately 2 ms^{-1} in our LES. Conversely, the secondary circulation structure persists even when parallel-river wind speed is as high as 16 ms^{-1}. The peak value of the mesoscale vertical wind (i.e. phase wind) variance profile has been identified as an indicator of secondary

circulation strength through dimensional analysis. In addition, the secondary circulation strength positively correlates with the Bowen ratio, stability parameter, and thermal heterogeneity parameter.

Chapter 4 is devoted to evaluating four *FI* prediction models over a two-dimensional checkerboard soil moisture heterogeneity, encompassing a range of scales from 50 m to 2.4 km. The *FI* is defined as the ratio of the nonlocal processes (i.e. total vertical advection flux and dispersive flux) to the total reference heat flux. A positive value of the *FI* indicates an underestimation of the heat flux. *FI* prediction models are based on semi-empirical similarity functions through proper scaling parameters, including stability parameters ($\frac{u_*}{w_*}$, note $-zi/L = -\kappa\frac{w_*^3}{u_*^3}$), measurement height ($z$), boundary layer height (z_i), horizontal wind speed (U), and time average period (T), among others. The results indicate that the heterogeneity scale affects the structure of secondary circulation. As the heterogeneity scale decreases, secondary circulation transitions from thermally induced secondary circulations to turbulent slow-moving organized structures. Despite these different secondary circulation patterns, the performance of the *FI* prediction models remains nearly unaffected, with *FI* being adequately captured in the atmospheric surface layer. Additionally, the quadrant analysis shows that the enhanced difference between the flux contribution between the ejections ($w' > 0,\ \theta' > 0$) and the sweeps ($w' < 0,\ \theta' < 0$) explains that the *FI* increased with the measurement height, further highlighting the importance of the height in the measurement and the vertical grid size in the ESMs.

Chapter 5 proposes a nonlocal first-order turbulence closure scheme: flux imbalance and K-theory approach (FLIMK). The FLIMK scheme accounts for the nonlocal processes using *FI* prediction models and local processes using K-theory. To test the FLIMK scheme, we used LES output as a *priori*, with the LES-prescribed sensible heat flux at the land surface as a reference. Subregions with different sizes, ranging from 50 m to 9.6 km, are selected to investigate the impact of heterogeneity scales on the performance of the FLIMK scheme. The results suggest that the underestimation (*FI*) of K-theory is consistent across all scales, with values ranging from approximately 12% to 16%. In comparison, the FLIMK scheme decreases the *FI* to approximately 6%. The FLIMK scheme is then implemented in a numerical weather prediction model (NWP) and tested in single-column mode using data from the Atmospheric Radiation Measurement campaign. A similar result is found that the FLIMK scheme decreased the flux imbalance from 16% to 6.7 % compared to the conventional K-theory.

6.2. Limitations

One of the main limitations of this work is the focus on secondary circulation solely within well-developed unstable boundary conditions. The applicability of the *FI* prediction models is limited during nighttime, as they are inapplicable for either eddy covariance measurements or ESMs parameterizations under stable and neutral atmospheric conditions. To illustrate, the convective velocity scale, ($w_* = \left(\frac{g}{\theta_v} z_i \overline{w'\theta'}\right)^{1/3}$), is not well defined in the stable boundary layer when the turbulent heat flux ($\overline{w'\theta'}$) is negative. The atmospheric evolution during transitional periods (after sunrise or sunset) remains unclear because all LES simulation setups in this study are idealized with constant incoming radiation or prescribed heat fluxes. Thus, a precise point at which the *FI* prediction model should be initiated in the subgrid-scale parametrization in ESMs remains to be determined. As previously discussed by Frassen et al. (2010), the imbalance may be even more pronounced at night, though, with a smaller absolute value. The method proposed by Zhou *et al.*, (2019), which is based on the auto-correlation function of the vertical velocity, appears to circumvent the issue of requiring a convective boundary layer. However, the vertical wind velocity at night is much smaller. Thus, this approach is unsuitable for parameterizing the subgrid-scale ESMs in the current form.

A further limitation of this study is that it focuses on the impact of secondary circulation on the atmosphere in the surface layer. The impact of secondary circulation on the entrainment zone has been studied less. The turbulence generated by secondary circulation penetrates the entrainment zone to a greater depth in comparison to that generated by small-scale eddies, resulting in a greater entrainment flux and a slightly higher boundary layer height (z_i). Nevertheless, the impact of secondary circulations on the free atmosphere above remains unclear. It has been documented that a well-developed secondary circulation system has been observed to enhance the liquid water pathways (Han *et al.*,2019) and facilitate the development of deep convection processes, which in turn result in precipitation events. LES conducted for this work is limited to several hours, and thus, the influence of secondary circulation on cloud formation was not studied either.

A further limitation of this PhD work is the absence of a sensitivity analysis of the vertical grid resolution. Previous research indicates that a horizontal grid size of 50 m is sufficient to adequately resolve the energy-containing eddies (Sullivan and Patton, 2011). However,

research focusing on the optimal vertical grid size is limited. Chapter 4 indicates that the sub-grid scale contribution to the heat flux is not negligible for layers adjacent to the land surface. It is often the case that data in this layer is neglected in the process, as has been previously discussed by Zhou *et al.*, (2019), who discarded any data that is lower than Approximately 30 m with zi ~ 1,000 m, which is equivalent to 0.03 zi in their work. In the work of De Roo *et al.*, (2018), a nesting technique is applied to enhance the spatial resolution in the vertical direction while maintaining an acceptable computational burden. It would be interesting to determine which vertical grid size the Monin-Obukhov similarity theory (MOST) would remain valid. As Bou-Zeid (2020) has previously discussed, MOST can only be used to parameterize the land surface and atmosphere interaction when the first grid is higher than the blending height. Furthermore, the land cover will contribute to the blending height by modifying the roughness length. In the present study, however, only bare soil was considered.

6.3. Outlook

This doctoral dissertation examines the formation of the secondary circulation and assesses the feasibility of integrating the influence of secondary circulations on flux estimation through the *FI* prediction models within the ESMs subgrid-scale parameterization. As indicated in the preceding section, a longer simulation period with diurnal dynamics will allow for an investigation of the atmospheric structure's development during transitional periods, such as those occurring after sunrise or sunset, which enables research on the formation and dissolution of secondary circulations. Furthermore, research indicates that the spatial scales of heat fluxes vary throughout the seasons. Based on distributed tower networks and intensive airborne observations over a heterogeneous mid-latitude forested landscape in Northern Wisconsin, USA, Paleri *et al.*, (2022) found significant mesoscale contribution during summer and autumn. Therefore, a year-long LES is recommended to facilitate further research into the diurnal and seasonal dynamics of the secondary circulations. Few studies have focused on long-duration simulations using LES. For example, Schalkwijk *et al.*, (2016) conducted a one-year LES in 2012 over the Cabauw site in the Netherlands, considering a homogeneous land surface. Research extending to heterogeneous surfaces will provide valuable contributions to the field.

A potential avenue for ongoing research is the incorporation of tracers in LES. Similarly, as Huang *et al.*, (2008) did, one may implement both the top-down and bottom-up diffusion (of gases) in LES. The top-down diffusion could be achieved with a non-zero flux at the mixed-layer top and a zero at the surface. This approach will facilitate a comprehensive understanding

of the detailed contribution from the land surface and the entrainment to the *FI*. The focus can also be on examining the effects of the secondary circulation on the free atmosphere above. Moreover, introducing tracers will enable a more nuanced understanding of the distribution of relevant scalars, such as carbon dioxide. Without tracers, misclassifying carbon sinks as carbon sources or vice versa may result from underestimating or overestimating fluxes.

As evidenced by the current LES study, the impact of subgrid-scale parameterization on the lowest level heat flux is notable. Therefore, an additional focus should be on understanding the role that the vertical grid size plays in the ESMs, especially within a height close to the land surface. Two possible recommendations can be made: firstly, using a nesting technology to increase the grid size, as demonstrated by Maronga *et al.*, (2017), or secondly, using the direct numerical simulation (DNS), although this is only effective for relatively low Reynolds numbers of fluid due to the computational cost.

Acknowledgement

The completion of this thesis would not have been possible without the input of the author's love and the assistance of others. I would like to express my sincerest gratitude to my supervisor, Prof. Dr. Stefan Kollet. Stefan Kollet is highly knowledgeable and patient, providing invaluable guidance and support throughout my scientific studies. I am grateful for the numerous opportunities we had to meet and discuss, including model debugging, model results analysis, scientific writing, and many others. Additionally, I am thankful for Stefan's assistance in providing resources and support to conduct my research at the Forschungszentrum Juelich.

I would also like to extend my gratitude to Dr. Stefan Poll. Stefan Poll provides assistance with the implementation of the model and all data analysis. Furthermore, Stefan Poll participates in all weekly (later bi-weekly) meetings in the company of Stefan Kollet, offering indispensable guidance on my research. I am grateful to have the support of the two ‘Stefans‘.

I would also like to thank all the other colleagues at IBG3, Klaus, Bibi, Kaveh, Jan, Rigor, Yueling, Carl, Tobias, Yikui, Roland, Chris, Antonio, and many others that I have not mentioned here.

Last but not least, thanks to my parents for their support.

Bibliography

Albertson, J. D., Kustas, P. and Scanlon, M. (2001) "Large-eddy simulation over heterogeneous terrain with remotely sensed land surface conditions and LES (in the absence of free parameters) yields regionally averaged land surface height in the atmospheric surface atmosphere is shown to be scale-dependent," *Water resources research*, 37(7), pp. 1939–1953.

Ament, F. and Simmer, C. (2006) "Improved representation of land-surface heterogeneity in a non-hydrostatic numerical weather prediction model," *Boundary-Layer Meteorology*, 121(1), pp. 153–174. doi: 10.1007/s10546-006-9066-4.

Aubinet, M. *et al.* (1999) "Estimates of the Annual Net Carbon and Water Exchange of Forests: The EUROFLUX Methodology," in *Advances in Ecological Research*, pp. 113–175. doi: 10.1016/S0065-2504(08)60018-5.

Avissar, R. *et al.* (1989) "A Parameterization of Heterogeneous Land Surfaces for Atmospheric Numerical Models and Its Impact on Regional Meteorology," *Monthly Weather Review*, 117(10), pp. 2113–2136. doi: 10.1175/1520-0493(1989)117<2113:APOHLS>2.0.CO;2.

Avissar, R. and Chen, F. (1993) "Development and Analysis of Prognostic Equations for Mesoscale Kinetic Energy and Mesoscale (Subgrid Scale) Fluxes for Large-Scale Atmospheric Models," *Journal of the Atmospheric Sciences*, 50(22), pp. 3751–3774.

Avissar, R. and Schmidt, T. (1998) "An Evaluation of the Scale at which Ground-Surface Heat Flux Patchiness Affects the Convective Boundary Layer Using Large-Eddy Simulations," *Journal of the Atmospheric Sciences*. American Meteorological Society, 55(16), pp. 2666–2689. doi: 10.1175/1520-0469(1998)055<2666:AEOTSA>2.0.CO;2.

Baldocchi, D. *et al.* (2001) "FLUXNET: A New Tool to Study the Temporal and Spatial Variability of Ecosystem-Scale Carbon Dioxide, Water Vapor, and Energy Flux Densities," *Bulletin of the American Meteorological Society*, 82(11), pp. 2415–2434. doi: 10.1175/1520-0477(2001)082<2415:FANTTS>2.3.CO;2.

Baldocchi, D. D. (2003) "Assessing the eddy covariance technique for evaluating carbon dioxide exchange rates of ecosystems: Past, present and future," *Global change biology*, 9(4), pp. 479–492. doi: 10.1046/j.1365-2486.2003.00629.x.

Baldocchi, D. D. (2020) "How eddy covariance flux measurements have contributed to our understanding of Global Change Biology," *Global change biology*, 26(1), pp. 242–260. doi: 10.1111/gcb.14807.

Barr, A. G. *et al.* (2006) "Surface energy balance closure by the eddy-covariance method above three boreal forest stands and implications for the measurement of the CO2 flux," *Agricultural and Forest Meteorology*, 140(1–4), pp. 322–337. doi: 10.1016/j.agrformet.2006.08.007.

Bauer, P., Thorpe, A. and Brunet, G. (2015) "The quiet revolution of numerical weather prediction," *Nature*, 525(7567), pp. 47–55. doi: 10.1038/nature14956.

Blyth, E. M. *et al.* (2021) "Advances in Land Surface Modelling," *Current Climate Change Reports*. Current Climate Change Reports, 7(2), pp. 45–71. doi: 10.1007/s40641-021-00171-5.

Boekee, J. *et al.* (2024) “Rethinking the Roughness Height: An Improved Description of Temperature Profiles over Short Vegetation,” *Boundary-Layer Meteorology*, 190(7), p. 31. doi: 10.1007/s10546-024-00871-z.

Bou-Zeid, E. *et al.* (2020) “The Persistent Challenge of Surface Heterogeneity in Boundary-Layer Meteorology: A Review,” *Boundary-Layer Meteorology*. Springer Netherlands, 177(2), pp. 227–245. doi: 10.1007/s10546-020-00551-8.

Bou-Zeid, E., Meneveau, C. and Parlange, M. B. (2004) “Large-eddy simulation of neutral atmospheric boundary layer flow over heterogeneous surfaces: Blending height and effective surface roughness,” *Water resources research*, 40(2), pp. 1–18. doi: 10.1029/2003WR002475.

Bou-Zeid, E., Parlange, M. B. and Meneveau, C. (2007) “On the parameterization of surface roughness at regional scales,” *Journal of the Atmospheric Sciences*, 64(1), pp. 216–227. doi: 10.1175/JAS3826.1.

Brown, A. R. *et al.* (2002) “Large-eddy simulation of the diurnal cycle of shallow cumulus convection over land,” *Quarterly Journal of the Royal Meteorological Society*, 128, pp. 1075–1093. doi: 10.1256/003590002320373210.

Businger, J. A. *et al.* (1971) “Flux-profile relationships in the atmospheric surface layer,” *Journal of the Atmospheric Sciences*, 28(2), pp. 181–189.

Chow, F. K. *et al.* (2019) “Crossing Multiple Gray Zones in the Transition from Mesoscale to Microscale Simulation over Complex Terrain,” *Atmosphere*. Multidisciplinary Digital Publishing Institute, 10(5), p. 274. doi: 10.3390/atmos10050274.

Chu, H. *et al.* (2023) “AmeriFlux BASE data pipeline to support network growth and data sharing,” *Scientific Data*, 10(1), pp. 1–13. doi: 10.1038/s41597-023-02531-2.

Cioni, G. and Hohenegger, C. (2017) “Effect of Soil Moisture on Diurnal Convection and Precipitation in Large-Eddy Simulations,” *Journal of Hydrometeorology*. American Meteorological Society, 18(7), pp. 1885–1903. doi: 10.1175/JHM-D-16-0241.1.

Collaud Coen, M. *et al.* (2014) “Determination and climatology of the planetary boundary layer height above the Swiss plateau by in situ and remote sensing measurements as well as by the COSMO-2 model,” *Atmospheric Chemistry and Physics*. Copernicus GmbH, 14(23), pp. 13205–13221. doi: 10.5194/acp-14-13205-2014.

De Roo, F. *et al.* (2018) “A semi-empirical model of the energy balance closure in the surface layer,” *PloS one*, 13(12), pp. 1–23. doi: 10.1371/journal.pone.0209022.

De Roo, F. and Mauder, M. (2018a) “The influence of idealized surface heterogeneity on turbulent flux measurements : a parameter study with large-eddy simulation,” *Atmospheric Chemistry and Physics*, (2015), pp. 1–17.

De Roo, F. and Mauder, M. (2018b) “The influence of idealized surface heterogeneity on virtual turbulent flux measurements,” *Atmospheric Chemistry and Physics*. Copernicus GmbH, 18(7), pp. 5059–5074. doi: 10.5194/acp-18-5059-2018.

Dipankar, A. *et al.* (2015a) “Large eddy simulation using the general circulation model ICON,” *Journal of Advances in Modeling Earth Systems*, 6, pp. 963–986. doi: 10.1002/2015MS000431.

Dipankar, A. *et al.* (2015b) "Large eddy simulation using the general circulation model ICON," *Journal of advances in modeling earth systems*. American Geophysical Union (AGU), 6(3), pp. 963–986. doi: 10.1002/2015MS000431.Received.

Ďurán, I. B. *et al.* (2021) "The icon single-column mode," *Atmosphere*, 12(7), pp. 1–24. doi: 10.3390/atmos12070906.

Eder, F., Schmidt, M., *et al.* (2015) "Mesoscale eddies affect near-surface turbulent exchange: Evidence from lidar and tower measurements," *Journal of Applied Meteorology and Climatology*, 54(1), pp. 189–206. doi: 10.1175/JAMC-D-14-0140.1.

Eder, F., De Roo, F., *et al.* (2015) "Secondary circulations at a solitary forest surrounded by semi-arid shrubland and their impact on eddy-covariance measurements," *Agricultural and Forest Meteorology*. Elsevier B.V., 211–212, pp. 115–127. doi: 10.1016/j.agrformet.2015.06.001.

Eder, F., Serafimovich, A. and Foken, T. (2013) "Coherent Structures at a Forest Edge: Properties, Coupling and Impact of Secondary Circulations," *Boundary-Layer Meteorology*, 148(2), pp. 285–308. doi: 10.1007/s10546-013-9815-0.

Edwards, J. M. *et al.* (2020) "Representation of Boundary-Layer Processes in Numerical Weather Prediction and Climate Models," *Boundary-Layer Meteorology*. Springer Netherlands, 177(2–3), pp. 511–539. doi: 10.1007/s10546-020-00530-z.

Finnigan, J. J. *et al.* (2003) "A Re-evaluation of long-term flux measurement techniques part I: averaging and coordinate rotation," *Boundary-Layer Meteorology*, 107, pp. 1–48.

Finnigan, J. J. and Shaw, R. H. (2008) "Double-averaging methodology and its application to turbulent flow in and above vegetation canopies," *Acta Geophysica*, 56(3), pp. 534–561. doi: 10.2478/s11600-008-0034-x.

Foken, T. (2006) "50 Years of the Monin–Obukhov Similarity Theory," *Boundary-Layer Meteorology*, 119(3), pp. 431–447. doi: 10.1007/s10546-006-9048-6.

Foken, T. (2008) "The energy balance closure problem: An overview," *Ecological applications: a publication of the Ecological Society of America*, 18(6), pp. 1351–1367. doi: 10.1890/06-0922.1.

Foken, T. *et al.* (2010) "Energy balance closure for the LITFASS-2003 experiment," *Theoretical and Applied Climatology*, 101(1), pp. 149–160. doi: 10.1007/s00704-009-0216-8.

Foken, T. *et al.* (2011) "Results of a panel discussion about the energy balance closure correction for trace gases," *Bulletin of the American Meteorological Society*, 92(4), pp. 13–18. doi: 10.1175/2011BAMS3130.1.

Fowler, M. D. *et al.* (2024) "Assessing the Atmospheric Response to Subgrid Surface Heterogeneity in the Single-Column Community Earth System Model, Version 2 (CESM2)," *Journal of Advances in Modeling Earth Systems*, 16(3), pp. 1–18. doi: 10.1029/2022MS003517.

Franssen, H. J. H. *et al.* (2010) "Energy balance closure of eddy-covariance data: A multisite analysis for European FLUXNET stations," *Agricultural and Forest Meteorology*. Elsevier B.V., 150(12), pp. 1553–1567. doi: 10.1016/j.agrformet.2010.08.005.

Gao, Z. *et al.* (2016) "Large eddies modulating flux convergence and divergence in a disturbed unstable atmospheric surface layer," *Journal of Geophysical Research, D: Atmospheres*, 121, pp. 4211–4232. doi: 10.1002/2015JD024529.Received.

Gao, Z., Russell, E. S., *et al.* (2017) "A novel approach to evaluate soil heat flux calculation: An analytical review of nine methods," *Journal of geophysical research*, 122(13), pp. 6934–6949. doi: 10.1002/2017JD027160.

Gao, Z., Liu, H., *et al.* (2017) "Non-closure of the surface energy balance explained by phase difference between vertical velocity and scalars of large atmospheric eddies," *Environmental research letters: ERL [Web site]*, 12. doi: 10.1088/1748-9326/aa625b.

Gao, Z. *et al.* (2020) "Enlarged Nonclosure of Surface Energy Balance With Increasing Atmospheric Instabilities Linked to Changes in Coherent Structures," *Journal of Geophysical Research, D: Atmospheres*, 125(14), pp. 1–13. doi: 10.1029/2020JD032889.

Gerken, T. *et al.* (2019) "Robust observations of land-to-atmosphere feedbacks using the information flows of FLUXNET," *npj Climate and Atmospheric Science*. Nature Publishing Group, 2(1), pp. 1–10. doi: 10.1038/s41612-019-0094-4.

Giorgi, F. and Avissar, R. (1997) "Representation of heterogeneity effects in Earth system modeling: Experience from land surface modeling," *Reviews of geophysics* , 35(4), pp. 413–437. doi: 10.1029/97RG01754.

Gopalakrishnan, S. G. and Avissar, R. (2000) "An LES study of the impacts of land surface heterogeneity on dispersion in the convective boundary layer," *Journal of the Atmospheric Sciences*, 57(2), pp. 352–371. doi: 10.1175/1520-0469(2000)057<0352:ALSOTI>2.0.CO;2.

Grasselt, R. *et al.* (2008) "Validation of TERRA-ML with discharge measurements," *Meteorologische Zeitschrift*. Schweizerbart, 17(6), pp. 763–773. doi: 10.1127/0941-2948/2008/0334.

Gustafson, W. I. *et al.* (2020) "The Large-Eddy Simulation (LES) Atmospheric Radiation Measurement (ARM) Symbiotic Simulation and Observation (LASSO) Activity for Continental Shallow Convection," *Bulletin of the American Meteorological Society*, 101(4), pp. E462–E479. doi: 10.1175/BAMS-D-19-0065.1.

Han, C. *et al.* (2019) "Large-eddy simulation of catchment-scale circulation," *Quarterly Journal of the Royal Meteorological Society*. Wiley, 145(720), pp. 1218 – 1233. doi: 10.1002/qj.3491.

Han, C., Brdar, S. and Kollet, S. (2019) "Response of convective boundary layer and shallow cumulus to soil moisture heterogeneity: A large-eddy simulation study," *Journal of advances in modeling earth systems*. American Geophysical Union (AGU), 11(12), pp. 4305–4322. doi: 10.1029/2019ms001772.

van Heerwaarden, C. C., Mellado, J. P. and De Lozar, A. (2014) "Scaling Laws for the Heterogeneously Heated Free Convective Boundary Layer," *Journal of the Atmospheric Sciences*. American Meteorological Society, 71(11), pp. 3975–4000. doi: 10.1175/JAS-D-13-0383.1.

Heinze, R. *et al.* (2017) "Large-eddy simulations over Germany using ICON: a comprehensive evaluation," *Quarterly Journal of the Royal Meteorological Society*. Wiley, 143(702), pp. 69–100. doi: 10.1002/qj.2947.

Helbig, M. *et al.* (2021) "Integrating continuous atmospheric boundary layer and tower-based flux measurements to advance understanding of land-atmosphere interactions," *Agricultural and Forest Meteorology*, 307(August 2020). doi: 10.1016/j.agrformet.2021.108509.

Hellsten, A. *et al.* (2021) "A nested multi-scale system implemented in the large-eddy simulation model PALM model system 6.0," *Geoscientific model development*. Copernicus GmbH, 14(6), pp. 3185–3214. doi: 10.5194/gmd-14-3185-2021.

Högström, U. (1988) "Non-dimensional wind and temperature profiles in the atmospheric surface layer: A re-evaluation," *Boundary-Layer Meteorology*, 42(1–2), pp. 55–78. doi: 10.1007/BF00119875.

Högström, U. and Bergström, H. (1996) "Organized Turbulence Structures in the Near-Neutral Atmospheric Surface Layer," *Journal of the Atmospheric Sciences*, 53(17), pp. 2452–2464. doi: 10.1175/1520-0469(1996)053<2452:OTSITN>2.0.CO;2.

Hohenegger, C. *et al.* (2009) "The soil moisture-precipitation feedback in simulations with explicit and parameterized convection," *Journal of climate*, 22(19), pp. 5003–5020. doi: 10.1175/2009JCLI2604.1.

Huang, H. Y. and Margulis, S. A. (2009) "On the impact of surface heterogeneity on a realistic convective boundary layer," *Water resources research*. American Geophysical Union (AGU), 45(4), pp. 1–16. doi: 10.1029/2008WR007175.

Huang, H.-Y. and Margulis, S. A. (2013) "Impact of soil moisture heterogeneity length scale and gradients on daytime coupled land-cloudy boundary layer interactions," *Hydrological processes*. Wiley, 27(14), pp. 1988–2003. doi: 10.1002/hyp.9351.

Huang, J., Lee, X. and Patton, E. G. (2008) "A Modelling Study of Flux Imbalance and the Influence of Entrainment in the Convective Boundary Layer," *Boundary-Layer Meteorology*, 127(2), pp. 273–292. doi: 10.1007/s10546-007-9254-x.

Huang, M. *et al.* (2022) "Representing surface heterogeneity in land–atmosphere coupling in E3SMv1 single-column model over ARM SGP during summertime," *Geoscientific Model Development*, 15(16), pp. 6371–6384. doi: 10.5194/gmd-15-6371-2022.

Inagaki, A. *et al.* (2006) "The impact of the surface heterogeneity on the energy imbalance problem using les," *Journal of the Meteorological Society of Japan*, 84(1), pp. 187–198. doi: 10.2208/prohe.49.343.

Joffre, S. M. *et al.* (2001) "Variability of the stable and the unstable atmospheric boundary-layer height and its scales over a boreal forest," *Boundary-Layer Meteorology*, 99(3), pp. 429–450. doi: 10.1023/A:1018956525605.

Kanda, M. *et al.* (2004) "LES Study of the Energy Imbalance Problem with Eddy Covariance Fluxes," *Boundary-Layer Meteorology*, 110(3), pp. 381–404. doi: 10.1023/B:BOUN.0000007225.45548.7a.

Kang, S.-L. and Lenschow, D. H. (2014) “Temporal Evolution of Low-Level Winds Induced by Two-dimensional Mesoscale Surface Heat-Flux Heterogeneity,” *Boundary-Layer Meteorology*. Springer Science and Business Media LLC, 151(3), pp. 501–529. doi: 10.1007/s10546-014-9912-8.

Katul, G. G. *et al.* (2007) “On the spectrum of soil moisture from hourly to interannual scales,” *Water resources research*, 43(5), pp. 1–10. doi: 10.1029/2006WR005356.

Kenny, W. T. *et al.* (2017) “A Numerical Case Study of the Implications of Secondary Circulations to the Interpretation of Eddy-Covariance Measurements Over Small Lakes,” *Boundary-Layer Meteorology*. Springer Netherlands, 165(2), pp. 311–332. doi: 10.1007/s10546-017-0268-8.

Klein, R. (2008) “An unified approach to meteorological modelling based on multiple-scales asymptotics,” in *Topics in modern geophysical fluid dynamics - EGU General Assembly 2007, Vienna, Austria, 15–20 April 2007*. Copernicus GmbH, pp. 23–33. doi: 10.5194/adgeo-15-23-2008.

Kljun, N., Rotach, M. W. and Schmid, H. P. (2002) “A three-dimensional backward Lagrangian footprint model for a wide range of boundary-layer stratifications,” *Boundary-Layer Meteorology*, 103(2), pp. 205–226. doi: 10.1023/A:1014556300021.

Kuell, V. and Bott, A. (2022) “A nonlocal three-dimensional turbulence parameterization (NLT3D) for numerical weather prediction models,” *Quarterly Journal of the Royal Meteorological Society*, 148(742), pp. 117–140. doi: 10.1002/qj.4195.

Lamaud, E. and Irvine, M. (2006) “Temperature-humidity dissimilarity and heat-to-water-vapour transport efficiency above and within a pine forest canopy: The role of the Bowen ratio,” *Boundary-Layer Meteorology*, 120(1), pp. 87–109. doi: 10.1007/s10546-005-9032-6.

Lan, C. *et al.* (2023) “Linkage between surface energy balance non-closure and horizontal asymmetric turbulent transport,” *Quarterly Journal of the Royal Meteorological Society*, (August), pp. 1–18. doi: 10.1002/qj.4562.

Lawrence, D. M. *et al.* (2019) “The Community Land Model Version 5: Description of New Features, Benchmarking, and Impact of Forcing Uncertainty,” *Journal of Advances in Modeling Earth Systems*, 11(12), pp. 4245–4287. doi: 10.1029/2018MS001583.

Lee, J. M., Zhang, Y. and Klein, S. A. (2019) “The Effect of Land Surface Heterogeneity and Background Wind on Shallow Cumulus Clouds and the Transition to Deeper Convection,” *Journal of the Atmospheric Sciences*. American Meteorological Society, 76(2), pp. 401–419. doi: 10.1175/JAS-D-18-0196.1.

Li, D. (2019) “Turbulent Prandtl number in the atmospheric boundary layer - where are we now?,” *Atmospheric Research*. Elsevier, 216(August 2018), pp. 86–105. doi: 10.1016/j.atmosres.2018.09.015.

Li, D. and Bou-Zeid, E. (2011) “Coherent structures and the dissimilarity of turbulent transport of momentum and scalars in the unstable Atmospheric surface layer,” *Boundary-Layer Meteorology*, 140(2), pp. 243–262. doi: 10.1007/s10546-011-9613-5.

Li, D., Katul, G. G. and Liu, H. (2018) “Intrinsic Constraints on Asymmetric Turbulent Transport of Scalars Within the Constant Flux Layer of the Lower Atmosphere,” *Geophysical research letters*, 45(4), pp. 2022–2030. doi: 10.1002/2018GL077021.

Li, Q. *et al.* (2018) “Implications of nonlocal transport and conditionally averaged statistics on Monin-Obukhov similarity theory and Townsend’s attached eddy hypothesis,” *Journal of the Atmospheric Sciences*, 75(10), pp. 3403–3431. doi: 10.1175/JAS-D-17-0301.1.

Lilly, D. K. (1962) “On the numerical simulation of buoyant convection,” *Tell’Us*. Informa UK Limited, 14(2), pp. 148–172. doi: 10.1111/j.2153-3490.1962.tb00128.x.

Lin, H., Li, Y. and Zhao, L. (2022) “Partitioning of Sensible and Latent Heat Fluxes in Different Vegetation Types and Their Spatiotemporal Variations Based on 203 FLUXNET Sites,” *Journal of Geophysical Research, D: Atmospheres*, 127(21). doi: 10.1029/2022jd037142.

Liu, H. *et al.* (2024) “Scalar flux profiles in the unstable atmospheric surface layer under the influence of large eddies: Implications for eddy covariance flux measurements and the non-closure problem," *Geophysical research letters*. American Geophysical Union (AGU), 51(1). doi: 10.1029/2023gl106649.

Liu, H., Gao, Z. and Katul, G. G. (2021) “Non-Closure of Surface Energy Balance Linked to Asymmetric Turbulent Transport of Scalars by Large Eddies,” *Journal of Geophysical Research, D: Atmospheres*, 126(7), pp. 1–12. doi: 10.1029/2020JD034474.

Lothon, M. *et al.* (2014) “The BLLAST field experiment: Boundary-Layer late afternoon and sunset turbulence,” *Atmospheric Chemistry and Physics*, 14(20), pp. 10931–10960. doi: 10.5194/acp-14-10931-2014.

Mahrt, L. (2000) “Surface Heterogeneity and Vertical Structure of the Boundary Layer,” *Boundary-Layer Meteorology*, 96(1), pp. 33–62. doi: 10.1023/A:1002482332477.

Margairaz, F., Pardyjak, E. R. and Calaf, M. (2020a) “Surface Thermal Heterogeneities and the Atmospheric Boundary Layer: The Relevance of Dispersive Fluxes,” *Boundary-Layer Meteorology*. Springer Netherlands, 175(3), pp. 369–395. doi: 10.1007/s10546-020-00509-w.

Margairaz, F., Pardyjak, E. R. and Calaf, M. (2020b) “Surface Thermal Heterogeneities and the Atmospheric Boundary Layer: The Thermal Heterogeneity Parameter,” *Boundary-Layer Meteorology*. Springer Netherlands, 177(1), pp. 49–68. doi: 10.1007/s10546-020-00544-7.

Maronga, B. and Raasch, S. (2013) “Large-Eddy Simulations of Surface Heterogeneity Effects on the Convective Boundary Layer During the LITFASS-2003 Experiment,” *Boundary-Layer Meteorology*, 146(1), pp. 17–44. doi: 10.1007/s10546-012-9748-z.

Mauder, M. *et al.* (2013) “A strategy for quality and uncertainty assessment of long-term eddy-covariance measurements,” *Agricultural and Forest Meteorology*. Elsevier B.V., 169, pp. 122–135. doi: 10.1016/j.agrformet.2012.09.006.

Mauder, M. *et al.* (2018) “Evaluation of energy balance closure adjustment methods by independent evapotranspiration estimates from lysimeters and hydrological simulations,” *Hydrological processes*, 32(1), pp. 39–50. doi: 10.1002/hyp.11397.

Mauder, M. *et al.* (2021) “Options to correct local turbulent flux measurements for large-scale fluxes using an approach based on large-eddy simulation,” *Atmospheric Measurement Techniques*, 14(12), pp. 7835–7850. doi: 10.5194/amt-14-7835-2021.

Mauder, M., Foken, T. and Cuxart, J. (2020) “Surface-Energy-Balance Closure over Land: A Review,” *Boundary-Layer Meteorology*, 177(2), pp. 395–426. doi: 10.1007/s10546-020-00529-6.

Moeng, C.-H. (1984) “A Large-Eddy-Simulation Model for the Study of Planetary Boundary-Layer Turbulence,” *Journal of the Atmospheric Sciences*. American Meteorological Society, 41(13), pp. 2052–2062. doi: 10.1175/1520-0469(1984)041<2052:ALESMF>2.0.CO;2.

Morrison, T. *et al.* (2022) “The Heat-Flux Imbalance: The Role of Advection and Dispersive Fluxes on Heat Transport Over Thermally Heterogeneous Terrain,” *Boundary-Layer Meteorology*. Springer Netherlands, 183(2), pp. 227–247. doi: 10.1007/s10546-021-00687-1.

Morrison, T. J., Calaf, M. and Pardyjak, E. R. (2023) “A full three-dimensional surface energy balance over a desert playa,” *Quarterly Journal of the Royal Meteorological Society*. Wiley, 149(750), pp. 102–114. doi: 10.1002/qj.4397.

Niu, G. Y. *et al.* (2011) “The community Noah land surface model with multiparameterization options (Noah-MP): 1. Model description and evaluation with local-scale measurements,” *Journal of Geophysical Research, D: Atmospheres*, 116(12), pp. 1–19. doi: 10.1029/2010JD015139.

Novick, K. A. *et al.* (2018) “The AmeriFlux network: A coalition of the willing,” *Agricultural and Forest Meteorology*, 249(October 2017), pp. 444–456. doi: 10.1016/j.agrformet.2017.10.009.

Paleri, S. *et al.* (2022) “Space-Scale Resolved Surface Fluxes Across a Heterogeneous, Mid-Latitude Forested Landscape,” *Journal of Geophysical Research, D: Atmospheres*, 127(23). doi: 10.1029/2022JD037138.

Panin, G. N. and Bernhofer, C. (2008) “Parametrization of turbulent fluxes over inhomogeneous landscapes,” *Izvestiya, Atmospheric and Oceanic Physics/Izvestiya Rossiiskoi Akademii Nauk - Fizika Atmosfery i Okeana*, 44(6), pp. 701–716. doi: 10.1134/S0001433808060030.

Pastorello, G. *et al.* (2020) “The FLUXNET2015 dataset and the ONEFlux processing pipeline for eddy covariance data,” *Scientific data*, 7(1), p. 225. doi: 10.1038/s41597-020-0534-3.

Patton, E. G. *et al.* (2016) “Atmospheric stability influences on coupled boundary layer and canopy turbulence,” *Journal of the Atmospheric Sciences*, 73(4), pp. 1621–1647. doi: 10.1175/JAS-D-15-0068.1.

Patton, E. G., Sullivan, P. P. and Moeng, C.-H. (2005) “The Influence of Idealized Heterogeneity on Wet and Dry Planetary Boundary Layers Coupled to the Land Surface,” *Journal of the Atmospheric Sciences*. American Meteorological Society, 62(7), pp. 2078–2097. doi: 10.1175/JAS3465.1.

Pitman, A. J. (2003) “The evolution of, and revolution in, land surface schemes designed for climate models,” *International Journal of Climatology*, 23(5), pp. 479–510. doi: 10.1002/joc.893.

Pleim, J. E. (2007) “A combined local and nonlocal closure model for the atmospheric boundary layer. Part I: Model description and testing,” *Journal of Applied Meteorology and Climatology*, 46(9), pp. 1383–1395. doi: 10.1175/JAM2539.1.

Poll, S., Shrestha, P. and Simmer, C. (2017) “Modelling convectively induced secondary circulations in the terra incognita with TerrSysMP,” *Quarterly Journal of the Royal Meteorological Society*. Wiley, 143(707), pp. 2352–2361. doi: 10.1002/qj.3088.

Poll, S., Shrestha, P. and Simmer, C. (2022) “Grid resolution dependency of land surface heterogeneity effects on boundary - layer structure, " *Quarterly Journal of the Royal Meteorological Society*. Wiley, 148(742), pp. 141–158. doi: 10.1002/qj.4196.

Prabha, T. V., Karipot, A. and Binford, M. W. (2007) “Characteristics of secondary circulations over an inhomogeneous surface simulated with large-eddy simulation,” *Boundary-Layer Meteorology*. Springer Science and Business Media LLC, 123(2), pp. 239–261. doi: 10.1007/s10546-006-9137-6.

Raasch, S. and Harbusch, G. (2001) “An Analysis Of Secondary Circulations And Their Effects Caused By Small-Scale Surface Inhomogeneities Using Large-Eddy Simulation,” *Boundary-Layer Meteorology*, 101(1), pp. 31–59. doi: 10.1023/A:1019297504109.

Rebmann, C. *et al.* (2018) “ICOS eddy covariance flux-station site setup: A review,” *International Agrophysics*, 32(4), pp. 471–494. doi: 10.1515/intag-2017-0044.

Rihani, J. F., Chow, F. K. and Maxwell, R. (2015) “Journal of Advances in Modeling Earth Systems,” *Journal of Advances in Modeling Earth Systems*, 7, pp. 915–937. doi: 10.1002/ 2014MS000371.

Rihani, J. F., Chow, F. K. and Maxwell, R. M. (2015) "Isolating effects of terrain and soil moisture heterogeneity on the atmospheric boundary layer: Idealized simulations to diagnose land-atmosphere feedbacks," *Journal of Advances in Modeling Earth Systems*, 7(2), pp. 915–937. doi: 10.1002/2014MS000371.

Rybka, H. *et al.* (2021) “The behavior of high-CAPE (convective available potential energy) summer convection in large-domain large-eddy simulations with ICON,” *Atmospheric Chemistry and Physics*, 21(6), pp. 4285–4318. doi: 10.5194/acp-21-4285-2021.

Salesky, S. T., Chamecki, M. and Bou-Zeid, E. (2017) “On the Nature of the Transition Between Roll and Cellular Organization in the Convective Boundary Layer,” *Boundary-Layer Meteorology*. Springer Netherlands, 163(1), pp. 41–68. doi: 10.1007/s10546-016-0220-3.

Schalkwijk, J., Jonker, H. J. J. and Siebesma, A. P. (2016) “An Investigation of the Eddy-Covariance Flux Imbalance in a Year-Long Large-Eddy Simulation of the Weather at Cabauw,” *Boundary-Layer Meteorology*. Springer Netherlands, 160(1), pp. 17–39. doi: 10.1007/s10546-016-0138-9.

Schmutz, M. and Vogt, R. (2019) “Flux Similarity and Turbulent Transport of Momentum, Heat and Carbon Dioxide in the Urban Boundary Layer,” *Boundary-Layer Meteorology*, 172(1), pp. 45–65. doi: 10.1007/s10546-019-00431-w.

Schulz, J.-P. and Vogel, G. (2020) “Improving the Processes in the Land Surface Scheme TERRA: Bare Soil Evaporation and Skin Temperature,” *Atmosphere*. Multidisciplinary Digital Publishing Institute, 11(5), p. 513. doi: 10.3390/atmos11050513.

Sedlar, J. *et al.* (2022) “Investigating the Impacts of Daytime Boundary Layer Clouds on Surface Energy Fluxes and Boundary Layer Structure During CHEESEHEAD19,” *Journal of Geophysical Research, D: Atmospheres*, 127(5), pp. 1–24. doi: 10.1029/2021JD036060.

Seibert, P. *et al.* (2000) “Review and intercomparison of operational methods for the determination of the mixing height,” *Atmospheric environment*, 34(7), pp. 1001–1027. doi: 10.1016/S1352-2310(99)00349-0.

Shen, S. and Leclerc, M. Y. (1994) "Large-eddy simulation of small-scale surface effects on the convective boundary-layer structure," *Atmosphere-Ocean*. Taylor & Francis, 32(4), pp. 717–731. doi: 10.1080/07055900.1994.9649519.

Siebesma, A. P., Soares, P. M. M. and Teixeira, J. (2007) “A combined eddy-diffusivity mass-flux approach for the convective boundary layer,” *Journal of the Atmospheric Sciences*, 64(4), pp. 1230–1248. doi: 10.1175/JAS3888.1.

Smagorinsky, J. (1963) “GENERAL CIRCULATION EXPERIMENTS WITH THE PRIMITIVE EQUATIONS,” *Monthly Weather Review*, 91(3), pp. 99–164. doi: 10.1175/1520-0493(1963)091<0099:GCEWTP>2.3.CO;2.

Steinfeld, G. *et al.* (2007) “Spatial representativeness of single tower measurements and the imbalance problem with eddy-covariance fluxes: Results of a large-eddy simulation study,” *Boundary-Layer Meteorology*, 123(1), pp. 77–98. doi: 10.1007/s10546-006-9133-x.

Stevens, B. (2007) “On the growth of layers of nonprecipitating cumulus convection,” *Journal of the Atmospheric Sciences*, 64(8), pp. 2916–2931. doi: 10.1175/JAS3983.1.

Stoy, P. C. *et al.* (2013) “A data-driven analysis of energy balance closure across FLUXNET research sites: The role of landscape scale heterogeneity,” *Agricultural and Forest Meteorology*. Elsevier B.V., 171–172, pp. 137–152. doi: 10.1016/j.agrformet.2012.11.004.

Stull, R. B. (1988) *An Introduction to Boundary Layer Meteorology*. Edited by Roland B. Stull. Springer, Dordrecht. doi: 10.1007/978-94-009-3027-8.

Su, Z. (2002) “The Surface Energy Balance System (SEBS) for estimation of turbulent heat fluxes,” *Hydrology and Earth System Sciences*, 6(1), pp. 85–99. doi: 10.5194/isprs-archives-XLII-1-33-2018.

Sullivan, P. P. *et al.* (1998) “Structure of the entrainment zone capping the convective atmospheric boundary layer,” *Journal of the Atmospheric Sciences*, 55(19), pp. 3042–3064. doi: 10.1175/1520-0469(1998)055<3042:SOTEZC>2.0.CO;2.

Sullivan, P. P. and Patton, E. G. (2011) “The Effect of Mesh Resolution on Convective Boundary Layer Statistics and Structures Generated by Large-Eddy Simulation,” *Journal of*

the Atmospheric Sciences. American Meteorological Society, 68(10), pp. 2395–2415. doi: 10.1175/JAS-D-10-05010.1.

Sun, J. *et al.* (2012) "Turbulence regimes and turbulence intermittency in the stable boundary layer: During CASES-99," *Journal of the Atmospheric Sciences*, 69(1), pp. 338–351. doi: 10.1175/JAS-D-11-082.1.

Sun, J. *et al.* (2021) "Revisiting the Surface Energy Imbalance," *Journal of Geophysical Research, D: Atmospheres*, 126(11), pp. 1–31. doi: 10.1029/2020JD034219.

Suselj, K. *et al.* (2021) "Improving the representation of subtropical boundary layer clouds in the NASA GEOS model with the eddy-diffusivity/mass-flux parameterization," *Monthly Weather Review*, 149(3), pp. 793–809. doi: 10.1175/MWR-D-20-0183.1.

Tan, Z. *et al.* (2018) "An Extended Eddy-Diffusivity Mass-Flux Scheme for Unified Representation of Subgrid-Scale Turbulence and Convection," *Journal of Advances in Modeling Earth Systems*, 10(3), pp. 770–800. doi: 10.1002/2017MS001162.

Tennekes, H. (1973) "A Model for the Dynamics of the Inversion Above a Convective Boundary Layer," *Journal of the Atmospheric Sciences*. American Meteorological Society, 30(4), pp. 558–567. doi: 10.1175/1520-0469(1973)030<0558:AMFTDO>2.0.CO;2.

Twine, T. E. *et al.* (2000) "Correcting eddy-covariance flux underestimates over a grassland," *Agricultural and Forest Meteorology*. Elsevier BV, 103(3), pp. 279–300. doi: 10.1016/s0168-1923(00)00123-4.

Van Pham, T. *et al.* (2020) "ICON in Climate Limited-area Mode (ICON Release Version 2.6.1): a new regional climate model," *Geoscientific Model Development Discussions*. doi: 10.5194/gmd-2020-20.

VanZanten, M. C., Duynkerke, P. G. and Cuijpers, J. W. M. (1999) "Entrainment Parameterization in Convective Boundary Layers," *Journal of the Atmospheric Sciences*, 56(6), pp. 813–828. doi: 10.1175/1520-0469(1999)056<0813:EPICBL>2.0.CO;2.

Verma, P. and Burkhardt, U. (2022) "Contrail formation within cirrus: ICON-LEM simulations of the impact of cirrus cloud properties on contrail formation," *Atmospheric Chemistry and Physics*. Copernicus GmbH, 22(13), pp. 8819–8842. Available at: https://acp.copernicus.org/articles/22/8819/2022/.

Wan, H. *et al.* (2013) "The ICON-1.2 hydrostatic atmospheric dynamical core on triangular grids – Part 1: Formulation and performance of the baseline version," *Geoscientific model development*. Copernicus GmbH, 6(3), pp. 735–763. doi: 10.5194/gmd-6-735-2013.

Wanner, L. *et al.* (2022) "How Does the Choice of the Lower Boundary Conditions in Large-Eddy Simulations Affect the Development of Dispersive Fluxes Near the Surface?," *Boundary-Layer Meteorology*, 182(1), pp. 1–27. doi: 10.1007/s10546-021-00649-7.

Wanner, L. *et al.* (2024) "Towards Energy-Balance Closure with a Model of Dispersive Heat Fluxes," *Boundary-Layer Meteorology*. Springer Netherlands, 190(5), p. 25. doi: 10.1007/s10546-024-00868-8.

Wanner, L., Calaf, M. and Mauder, M. (2022) “Incorporating the effect of heterogeneous surface heating into a semi-empirical model of the surface energy balance closure,” *PloS one*, 17(6), p. e0268097. doi: 10.1371/journal.pone.0268097.

Waterman, T. *et al.* (2024) "A Two-Column Model Parameterization for Subgrid Surface Heterogeneity Driven Circulations," *Journal of Advances in Modeling Earth Systems*, 16(5), pp. 1–22. doi: 10.1029/2023MS003936.

Weinkaemmerer, J. *et al.* (2023) “Boundary-layer plumes over mountainous terrain in idealized large-eddy simulations,” *Quarterly Journal of the Royal Meteorological Society*, 149(757), pp. 3183–3197. doi: 10.1002/qj.4551.

Wilson, K. *et al.* (2002) “Energy balance closure at FLUXNET sites,” *Agricultural and Forest Meteorology*, 113(1–4), pp. 223–243. Available at: http://www.sciencedirect.com/science/article/pii/S0168192302001090.

Wyngaard, J. C. (2004) “Toward Numerical Modeling in the ‘Terra Incognita,’” *Journal of the Atmospheric Sciences*. American Meteorological Society, 61(14), pp. 1816–1826. doi: 10.1175/1520-0469(2004)061<1816:TNMITT>2.0.CO;2.

Wyngaard, J. C. (2010) *Turbulence in the Atmosphere*. Cambridge University Press. Available at: https://play.google.com/store/books/details?id=YLeBN1qYn-0C.

Wyngaard, J. C. and Brost, R. A. (1984) “Top-Down and Bottom-Up Diffusion of a Scalar in the Convective Boundary Layer,” *Journal of the Atmospheric Sciences*. American Meteorological Society, 41(1), pp. 102–112. doi: 10.1175/1520-0469(1984)041<0102:TDABUD>2.0.CO;2.

Yamamoto, S. *et al.* (2005) “Findings through the AsiaFlux network and a view toward the future,” *Journal of geographical sciences*. Springer Science and Business Media LLC, 15(2), pp. 142–148. doi: 10.1007/bf02872679.

Zängl, G. *et al.* (2015) “The ICON (ICOsahedral Non-hydrostatic) modelling framework of DWD and MPI-M: Description of the non-hydrostatic dynamical core,” *Quarterly Journal of the Royal Meteorological Society*. Wiley, 141(687), pp. 563–579. doi: 10.1002/qj.2378.

Zhang, L. *et al.* (2023) “Dissimilarity of Turbulent Transport of Momentum and Heat Under Unstable Conditions Linked to Convective Circulations,” *Journal of Geophysical Research, D: Atmospheres*, 128(8), pp. 1–18. doi: 10.1029/2022JD037997.

Zhang, L., Poll, S. and Kollet, S. (2023) "Large-eddy simulation of soil moisture heterogeneity-induced secondary circulation with ambient winds," *Quarterly Journal of the Royal Meteorological Society*, (vember 2022), pp. 1–17. doi: 10.1002/qj.4413.

Zhou, B. *et al.* (2018) “Reexamining the gradient and countergradient representation of the local and nonlocal heat fluxes in the convective boundary layer,” *Journal of the Atmospheric Sciences*, 75(7), pp. 2317–2336. doi: 10.1175/JAS-D-17-0198.1.

Zhou, B., Zhu, K. and Xue, M. (2017) “A physically based horizontal subgrid-scale turbulent mixing parameterization for the convective boundary layer,” *Journal of the Atmospheric Sciences*, 74(8), pp. 2657–2674. doi: 10.1175/JAS-D-16-0324.1.

Zhou, Y. *et al.* (2018) “Diurnal Variations of the Flux Imbalance Over Homogeneous and Heterogeneous Landscapes,” *Boundary-Layer Meteorology*. Springer Netherlands, 168(3), pp. 417–442. doi: 10.1007/s10546-018-0358-2.

Zhou, Y., Li, D. and Li, X. (2019) “The Effects of Surface Heterogeneity Scale on the Flux Imbalance under Free Convection,” *Journal of Geophysical Research, D: Atmospheres*, 124(15), pp. 8424–8448. doi: 10.1029/2018JD029550.

Zhou, Y. and Li, X. (2019) “Energy balance closures in diverse ecosystems of an endorheic river basin,” *Agricultural and Forest Meteorology*. Elsevier, 274(October 2018), pp. 118–131. doi: 10.1016/j.agrformet.2019.04.019.

Zhou, Y., Sühring, M. and Li, X. (2023) “Evaluation of energy balance closure adjustment and imbalance prediction methods in the convective boundary layer – A large eddy simulation study,” *Agricultural and Forest Meteorology*, 333, p. 109382. doi: 10.1016/j.agrformet.2023.109382.

Band / Volume 639
Insights into Mechanisms of Secondary Organic Aerosol Formation: Approaching Atmospherically Relevant Conditions in an Atmospheric Reaction Chamber
Y. Baker (2024), XVII, 122 pp
ISBN: 978-3-95806-776-9

Band / Volume 640
Advancing the representation of agricultural systems in Land Surface Models: systematic model evaluations and technical model developments
T. S. Boas (2024), xxi, 145 pp
ISBN: 978-3-95806-777-6

Band / Volume 641
Imaging spatial and temporal soil water content variations of the soil-plant continuum using ground penetrating radar
L. Lärm (2024), xii, 303 pp
ISBN: 978-3-95806-778-3

Band / Volume 642
Development of Iridium-based Nanostructures for Oxygen Evolution Reaction in PEM Water Electrolysis
S. Park (2024), 135 pp
ISBN: 978-3-95806-779-0

Band / Volume 643
Multi-dimensional GPR full-waveform inversion for small-scale hydrogeophysical soil characterization
D. Hoven (2024), IX, 163 pp
ISBN: 978-3-95806-781-3

Band / Volume 644
Analyse des Gastransports in komplexen Membransystemen durch Modellierung und multiskalige Simulation
K. Wilkner (2024), VIII, 122 pp
ISBN: 978-3-95806-784-4

Band / Volume 645
Deployment of Fuel Cell Vehicles in Road Transport and the Expansion of the Hydrogen Refueling Station Network: 2024 Update
T. Grube; M. Rex (2024), iii, 26 pp
ISBN: 978-3-95806-786-8

Band / Volume 646
Modellgestützte Analyse treibhausgasneutraler Transformationsstrategien für Deutschland
T. F. Schöb (2024), XII, 228 pp
ISBN: 978-3-95806-789-9

Band / Volume 647
Future Distribution Grids Using Geo-Referenced Synthetic Network Topologies
A. Bandam (2024), ix, 237 pp
ISBN: 978-3-95806-790-5

Band / Volume 648
Multi-scenario, high-resolution Lagrangian transport modeling for the analysis of the Asian tropopause aerosol layer
J. H. Clemens (2024), 143 pp
ISBN: 978-3-95806-792-9

Band / Volume 649
Prospektive Lebenszyklusanalysen von Power-to-Gas-Optionen
J. C. Koj (2024), XVIII, 197 pp
ISBN: 978-3-95806-794-3

Band / Volume 650
Assimilation of groundwater level and cosmic-ray neutron sensor soil moisture measurements into integrated terrestrial system models for better predictions
F. Li (2024), xvii, 172 pp
ISBN: 978-3-95806-796-7

Band / Volume 651
Integration of a rib-channel design to improve air-side contacting in solid oxide cell (SOC) stacks
Y. S. Ayhan (2024), 82 pp
ISBN: 978-3-95806-797-4

Band / Volume 652
Modelling Secondary Circulation in Convective Boundary Layer Using Large Eddy Simulation
L. Zhang (2024), 84 pp
ISBN: 978-3-95806-799-8

Energie & Umwelt / Energy & Environment
Band / Volume 652
ISBN 978-3-95806-799-8

Mitglied der Helmholtz-Gemeinschaft

JÜLICH
Forschungszentrum